Volume 6, Number 2, Spring 2020

ACERP
Advanced Ceramics Progress

ISSN 2423-7477
e-ISSN 2423-7485

Advanced Ceramics Progress

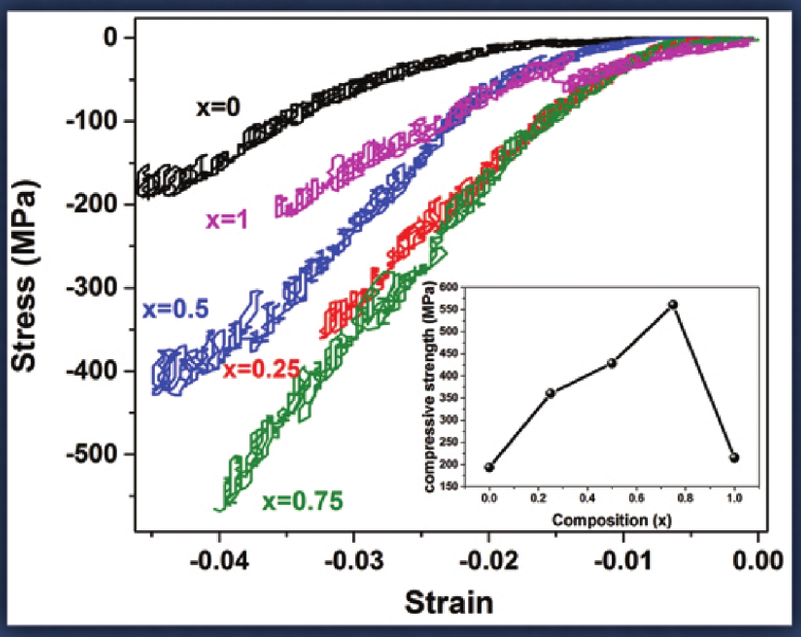

Materials and Energy
Research Center

Iranian Ceramic Society

In The name of God

Advanced Ceramics Progress

DISCLAIMER

The publication of papers in Advanced Ceramics Progress does not imply that the editorial board, editorial advisory board, reviewers or the publisher accept, approve or endorse the data and conclusions of authors.

Advanced **Cer**amics **P**rogress (ISSN 2423-7477) (e-ISSN 2423-7485)
Web Site: www.acerp.ir, E-mail: office@acerp.ir
Tel: +98 (0) 26 36280040-7 ext.: 382, Fax: +98 (0) 26 36201888
Tel:+98 (0)21 88771626-7 ext.: 8931, Fax: +98 (0)21 88773352
Materials and Energy Research Center (MERC); Iranian Ceramic Society (ICERS)

CONTENTS

ACERP: Vol. 6, No.2, (Spring 2020) 1-6

Advanced Ceramics Progress

Research Article

Journal Homepage: www.acerp.ir

Comparison of Semiconducting Behavior and Optical Properties of Oxyfluoride Glasses of SiO_2-Al_2O_3-BaF_2 and SiO_2-Al_2O_3-CaF_2 Systems

L. Farahinia [a], M. Rezvani [a] *, M. Rezazadeh [b]

[a] *Department of Materials Engineering, Faculty of Mechanical Engineering, University of Tabriz, Tabriz, Iran*
[b] *Department of Materials Engineering, Isfahan University of Technology, Isfahan , Iran*

PAPER INFO

Paper history:

Received 31 August 2019
Accepted in revised form 09 February 2020

Keywords:

Bandgap
Semiconductor Glass
Oxyfluoride

ABSTRACT

Amorphous semiconductors are materials with a brilliant prospect for a wide range of optical applications like solar cells, optical sensors, optical devices, and memories. The purpose of the present research was to study the semiconducting optical properties of SiO_2-Al_2O_3-CaF_2 and SiO_2-Al_2O_3-BaF_2 oxyfluoride glassy systems, which has been rarely studied from this point of view. The suitable compositions in the mentioned systems were chosen and melted in covered alumina crucibles at 1450˚C. Afterward, preheated stainless steel molds were used to shape the molten glasses. The absence of any crystallization peak in the XRD results indicated that the samples were amorphous. DTA patterns showed that the crystallization temperature of the fluoride phase is 693˚C for the glass containing BaF_2 (SAB), which is higher than the peak temperature (684˚C) for the glass with CaF_2 (SAC). DTA results were in accordance with density measurements, i. e., the density of the glass SAB (3.85 $g.cm^{-3}$) was higher than the glass SAC (2.70$g.cm^{-3}$). That is to say, BaF_2 presented a more continuous structure with lower amounts of dangling bonds. According to the UV-Vis spectra, sample SAB had higher absorption and smaller bandgap of the glass SAB (with a direct bandgap of 2.90 eV and indirect bandgap of 3.40 eV) indicated that it has better semiconducting behavior than sample SAC (with a direct bandgap of 3.07 eV and indirect bandgap of 3.60 eV). This increment of the semiconducting behavior is attributed to the more continuous structure of the glass SAB. Urbach energy, which is an indicator of disorder degree of structure, was 0.20 and 0.32eV for SAB and SAC, respectively. Therefore, the lower Urbach energy of SAB glass confirmed the higher structure order of it.

1. INTRODUCTION

When fluoride glasses were invented by Poulain et al. (1975) [1], nobody could imagine that these glasses would become the base of photonic glasses such as ZBLAN. The presence of heavy metal fluorides was the reason why they demonstrated unique optical characteristics like the preparation of fibers [2]. In fact, they have a very high position in optics considering the lower phonon energy of fluoride glasses (500 cm^{-1}) compared to oxide glasses [3]. Despite their low phonon energy, fluoride glasses encounter problems like weak thermal, chemical, and mechanical durability [4]. Hence, there were many attempts to solve the mentioned disadvantages, especially during the last decades. It has been shown that introducing oxygen to the network of fluoride glasses or adding fluorides to oxide melts accelerates crystallization. In case of adding high amounts of mentioned components, the outcome will be completely different. That is to say, if the percentage of oxygen gets high, as if it is one of the basic components, it can play the stabilizing role in fluoride glass [5]. A new concept emerged that entitled oxyfluoride glasses considering the entire mentioned above. Some amount of fluorine is substituted by oxygen in oxyfluoride glasses, which this leads to a more continuous glass network as well as higher stability [5].

The importance of oxyfluoride glasses arose from the crystallization possibility of them and resulting in transparent oxyfluoride glass-ceramics. For the first time, Ohwaki and Wang produced oxyfluoride glass-ceramics containing Er^{3+}/Yb^{3+}-doped $(Pb_x,Cd_{1-x})F_2$ nanocrystals [6]. They reported that the red emission of Er^{3+} ions has a higher intensity in the glass-ceramic sample than an amorphous one. This event was due to the effective energy transfer or cross-relaxation between Er^{3+} and Yb^{3+}

* Corresponding Author Email: m_rezvani@tabrizu.ac.ir (M. Rezvani)

https://doi.org/10.30501/acp.2020.105938

in crystallized samples, which was caused by the entrance of rare-earth ions into the low phonon energy-fluoride nanocrystals [6]. In other words, such kinds of glass-ceramics present both advantages of fluoride single crystals and oxide glasses [7]. After this achievement, Pb and Cd eliminated from oxyfluoride glasses and composition of glass-ceramics because of their environmental concerns [8]. Many substituents proposed by researchers like Dejneka who introduced oxyfluoride glass-ceramics containing LaF_3 nanocrystals. Although it was not toxic, the high cost of LaF_3 limited its applications and hindered its getting commercial [9]. Oxyfluoride glass-ceramics containing MF_2 (M=Ca, Ba, Sr) nanocrystals have received great attention during the last two decades as they are not toxic, they are economical, and have high solubility of rare-earth ions [8]. While a wide range of studies is devoted to optical semiconducting properties, luminescence, and up-conversion behavior of the base glass of MF_2 systems, there is not any comparison study between them. Therefore, the purpose of this study is to compare the optical semiconducting properties of two different MF_2 systems, i.e., SiO_2-Al_2O_3-CaF_2 and SiO_2-Al_2O_3-BaF_2. For this purpose, the optical bandgap and Urbach energy calculations were implemented after preparing transparent glasses.

2. EXPERIMENTAL PROCEDURE

High purity of raw materials were weighed and homogenized after choosing a suitable composition in each of the SiO_2-Al_2O_3-BaF_2 and SiO_2-Al_2O_3-CaF_2 systems (Table 1). K_2O was also used in the composition of glasses as a flux agent. Sb_2O_3 and As_2O_3 were added to batches to make bubble-free samples. Afterward, 50g of batches were melted in covered alumina crucibles in the electrical furnace at 1450˚C for 1hr.

TABLE 1. Chemical compositions of glasses in SiO_2-Al_2O_3- BaF_2 and SiO_2- Al_2O_3- BaF_2 systems (molar ratio)

Composition / Sample code	SiO_2	Al_2O_3	BaF_2	CaF_2	K_2O
SAB	50	20	30	-	5
SAC	50	20	-	30	5

Preheated steel molds (at 500 ˚C) were used to shape disc-like samples. Annealing process at 500 ˚C for 1 hour was applied for releasing internal stresses of shaped glasses.

Siemens D-500 system was used to record XRD patterns (Cu-Kα with the wavelength of 1.54Å). The scanning rate was chosen 0.5˚.min^{-1} to identify the crystalline phases or amorphous nature of specimens. Crystallization peak temperatures of glasses were obtained from DTA curves, which are obtained using DTG-60AH Shimadzu equipment with a heating rate of 10˚.min^{-1}. The density of samples was measured by the Archimedes standard method as follows:

$$D = \frac{W_1}{W_1 - W_2} \quad (1)$$

Where W_1 and W_2 are weights of the sample in air and water, respectively. Moreover, the molar volume is calculable using Equation 2:

$$V_m = \sum \frac{M_i}{D} \quad (2)$$

in Equation 2, M_i stands for molar mass, which is equal to:

$$M_i = C_i A_i \quad (3)$$

Where C_i and A_i are the molar concentration and the molecular weight of the ith component, respectively.
Moreover, the microhardness of samples is measured by Vickers micro-hardness equipment (HV-1000Z of PACE Technologies). For this purpose, the indentor was applied by the pressure of 1 N for 15 s.
The optical direct and indirect bandgap energy, Urbach tailing energy, and UV-Vis spectra of glasses were obtained by UV- Vis Shimadzu 1700 spectrophotometer to investigate the transparency. Accordingly, Tauc plots were drawn using their spectra and direct/indirect bandgap energy of samples were calculated. Urbach energy was also obtainable from Ln(α) vs. hυ diagrams and considering their slopes.

3. RESULTS AND DISCUSSION

3.1. Crystallization behavior of SAB and SAC glasses

DTA curves of SAB and SAC oxyfluoride glasses are presented in Figure 1. Similar to the DTA results of typical oxyfluoride glasses, initially, exothermic peaks are related to the crystallization of BaF_2 and CaF_2 nanocrystals in SAB and SAC glasses, respectively [10]. Furthermore, $BaAl_2Si_2O_8$ precipitates in BaF_2 containing glasses and $CaAl_2Si_2O_8$ (anorthite) in CaF_2-based glasses at the second exothermic peak temperatures. Precipitating of these aluminosilicate phases at second peak temperature is known as the crystallization of residual glassy matrixes [11, 12].

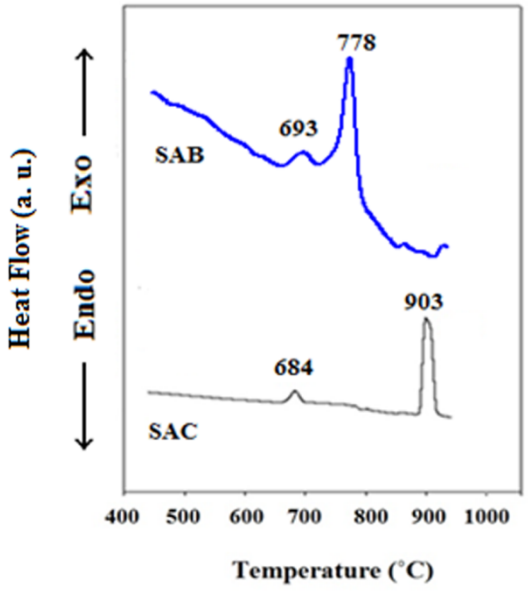

Figure 1. DTA curves of SAB and SAC samples

It is observable from Fig. 1 that the crystallization peak temperature of CaF_2 (684 ˚C) in the SAC sample is lower than BaF_2 (693 ˚C) in SAB glass. Factually, the crystallization of CaF_2 is somehow easier than BaF_2 in oxyfluoride glasses, which is probably due to the bond strengths in glasses, i.e., the crystallization accompanies the active dissociation of atomic bonds. Since energy of Ca-F and Ca-O bonds (523 and 351 KJ.mol^{-1}, respectively) are lower in comparison with Ba-F and Ba-O bonds (581 and 548KJ.mol^{-1}, respectively), lower activation energy are needed for crystallization of SAC glass [13]. Higher hardness of sample SAB is ascribed to the stronger bond energy of Ba-F and Ba-O compared to Ca-F and Ca-O bonds. On the other hand, two exothermic peaks in the DTA curve of the SAB sample are too close to each other, and the crystallization of BaF_2 overlaps with the crystallization of the glass matrix. Hence, the preparation of glass-ceramics containing only BaF_2 nanocrystals from SiO_2- Al_2O_3- BaF_2 glasses is difficult, which sounds to be easier for the SAC sample to be crystallized as glass-ceramics containing only CaF_2 nanocrystals [13].

Figure 2(a) represents the XRD patterns of SAB and SAC glasses. The absence of any crystallization peak and the presence of broad humps indicate the amorphous nature of samples. Furthermore, two humps in XRD patterns of each sample show the possibility of precipitation of two different crystalline phases, which is in accordance with DTA results.

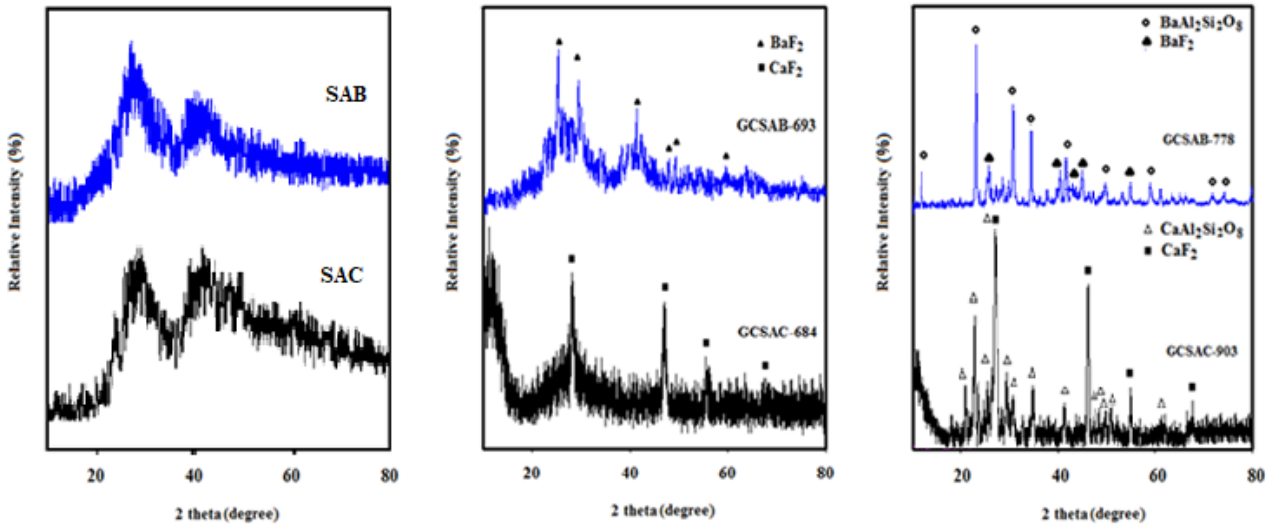

(a) **(b)** **(c)**

Figure 2. XRD patterns of **(a)** glasses and samples heat-treated at their **(b)** first and **(c)** second peak temperatures

Figure 2(b) and (c) exhibit the XRD results of SAB and SAC samples crystallized at their first and second DTA peak temperatures. According to these patterns, the only crystalline phase in glass-ceramics obtained at first peak temperatures (GCSAC-684 and GCSAB-693) are CaF_2 (JCPDS No. 35-0816) and BaF_2 (JCPDS No. 4-452). As claimed above, heat-treating at second peak temperature resulted in the crystallization of aluminosilicate phases in parallel with fluoride crystals (Fig. 2(c)). BaF_2 peaks in the XRD pattern of GCSAB-693 are broader than CaF_2 peaks of GCSAC-684. In other words, the movement of fluoride ions through the barriers around the fluoride crystallites that are Al_2O_3 and SiO_2 – riched layers, gets difficult and no more growth happens for nanocrystals of BaF_2 owing to the diffusion-controlled crystallization mechanism of both CaF_2 and BaF_2 oxyfluoride glasses

and more stronger atomic bonds in BaF_2 containing oxyfluorides [14,15]. As a consequence, the mean crystal size of nanocrystals is 10 and 19nm using the Scherrer equation for samples GCSAB-693 and GCSAC-684, respectively.

3.2. UV-Vis spectra and bandgap study

Figure 3 shows the UV-Vid spectra of specimens. The absorbance of SAB is higher than SAC, and its absorption edge is shifted to longer wavelengths. It should be noticed that the absorbance and absorption edge are affected by the bonds in glass network structure in all glassy materials [16]. In fact, only electrons of outer layers of materials can be excited and the result is absorption in the case of the incidence of a wavelength within the UV-Vis region. As discussed in the previous section, the bonds in SAB glass are much stronger than bonds in SAC glass. Therefore, there are less weak and dangling bonds in SAB, and the mean free path increases for this glass, and subsequently, its bandgap should be smaller [17]. To justify this claim, Tauc plots of both SAC and SAB glasses are presented in Fig. 4. According to Mott and Davis [18], the absorption coefficient (α) of an amorphous solid is related to the energy of the incident photon (hυ) and optical bandgap (E_g^{opt}). They proposed an equation for such behavior (Equation 4).

$$\alpha = \beta^2 \frac{(h\upsilon - E_g^{opt})}{h\upsilon} \quad (4)$$

where β is a constant value representing the residual band constant, which it is dependent on the refractive index of the sample. Moreover, according to indirect allowed, indirect forbidden, direct allowed, and direct forbidden transitions, the amount of n is 2, 3, 1/2, and 1/3, respectively [19]. Hence, based on the Tauc plots presented in Fig. 4, optical bandgap energy can be calculated. For this purpose, the intercept of the obtained linear part divided by its slope [19-21].

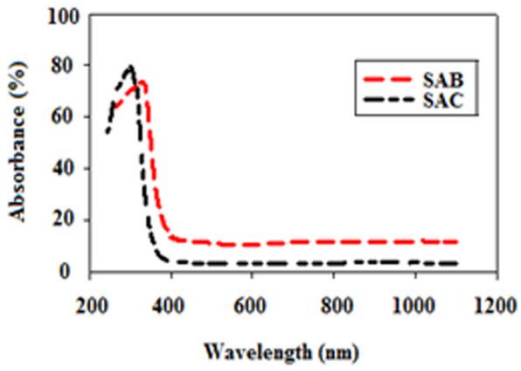

Figure 3. UV-Vis spectra of glasses

The calculated values for direct and indirect bandgaps (tabulated in Table 2) show that the bandgap energy of SAB is lower than the SAC sample, which proves the validity of the above-mentioned claim, i.e., SAB glass has a more continuous network with lower amounts of dangling bonds.

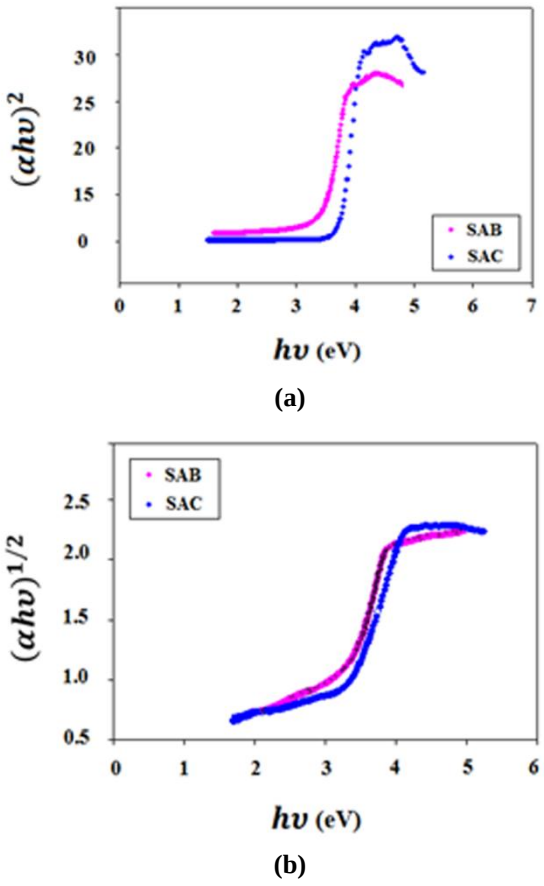

Figure 4. Tauc plots of **(a)** direct and **(b)** indirect bandgaps of SAC and SAB glasses

Additionally, the results of density measurements and molar volume calculations (also presented in Table 2) demonstrate that SAB has higher density and consequently lower V_m than SAC, which proves the more continuous structure.

TABLE 2. Some physical properties of SAC and SAB glasses

Sample Code	E_g Indirect (eV)	E_g Direct (eV)	E_U (eV)	V_m (cm^3/mol)	Hardness (MPa)	D (g/cm^3)
SAC	3.60	3.07	0.32	27.90	677.3	2.70
SAB	3.40	2.90	0.20	26.87	720.2	3.85

Short-range order in amorphous materials is the reason for weaker bonds between atoms and makes localized bond electrons in such atoms. These weak bonds result in tails in the bandgap and reduce the effective bandgap. However, the mobility of these electrons in tails is very hard and they do not play a role in the conduction of material. These tails are known as Urbach tails [22]. That is why the Urbach tail is considered as a degree of disorder in amorphous materials. Urbach energy (E_U) is obtainable using equation 5 and plotting diagrams of Ln(α) vs. hυ and converting the slope of the fitted line to such curves [23].

$$\alpha(\upsilon) = \beta \exp(\frac{h\upsilon}{E_U}) \quad (5)$$

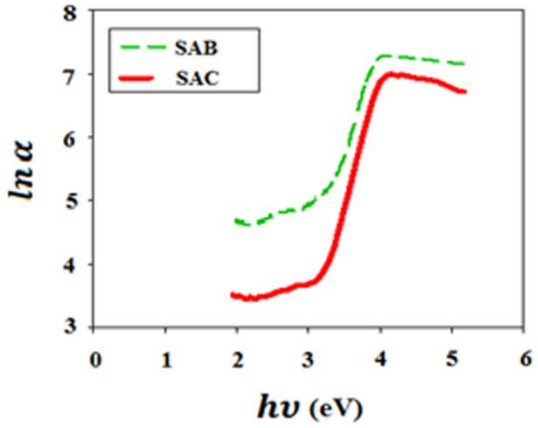

Figure 5. Ln(α) vs. hυ curves for SAC and SAB samples

Figure 5 shows the plots of Ln(α) vs. hυ of samples. Urbach energy of glasses are calculated from these curves and listed in Table. 2. Again lower band tailing energy of SAB implies its higher structural order compared to SAC.

4. CONCLUSIONS

1- According to DTA curves, it sounds like that the crystallization of BaF_2 nanocrystals from SAB glass was more difficult than the crystallization of the CaF_2 nanocrystals from SAC glass.
2- Higher crystallization temperature of BaF_2 in SAB indicated that the network of sample SAB is more continuous than SAC.
3- Lower bandgap energy of direct and indirect bandgaps (2.90 and 3.40 eV, respectively) of SAB glass was evidence of its lower transparency and better semiconducting behavior than SAC glass.
4- Urbach energy calculations also proved the higher degree of order in the SAB network and lower dangling bonds in its structure.
5- From the hardness and semiconducting behavior points of view, the sample SAB was preferred to the glass SAC. Furthermore, it was more favorable than SAC considering the lower mean crystal size of BaF_2 in the crystallized SAB sample. However, the lower transparency of SAB in the UV-Vis region was undeniable.

5. ACKNOWLEDGEMENTS

We would like to show our gratitude to Ali Rahimian and Amin Ahmadi, our colleagues who provided insight and experties that assisted this research.

REFERENCES

1. Poulain, M., Poulain, M., Lucas, J., "Verres fluores au tetrafluorure de zirconium proprietes optiques d'un verre dope au Nd^{3+}", ***Materials Research Bulletin***, Vol. 10, No. 4, (1975), 243-246.
2. Nazabal, V., Poulain, M., Olivier, M., Pirasteh, P., Comy, P., Doualan, J. L., Guy, S., Djouama, T., Boutarfaia, A., Adam, J. L., "Fluoride and oxyfluoride glasses for optical applications", ***Journal of Flourine Chemistry***, Vol. 134, (2012), 18-23.
3. Stevenson, A. J., Serier-Brault, H., Gredin, P., Mortier, M., "Fluoride materials for optical applications: single crystals, ceramics, glasses, and glass-ceramics", ***Journal of Fluorine Chemistry***, Vol. 132, No. 12, (2011), 1165-1173.
4. Babu, P., Jang, K. H., Kim, E. S., Shi, L., Seo, H. J., Lopez, F.E., "Optical properties and white-light emission in Dy^{3+}-doped transparent oxyfluoride glass and glass ceramics containing CaF_2 nanocrystals", ***Journal of the Korean Physical Society***, Vol. 54, No. 4, (2009), 1488-1491.
5. Polishchuk, S.A., Ignat'eva, L.N., Marchenko, Y.V., Bouznik, V.M., "Oxyfluoride glasses (a review)", G***lass Physics and Chemistry***, Vol. 37, No. 1, (2011), 1-20.
6. Wang, Y., Ohwaki, J., "New transparent vitroceramics codoped with Er^{3+} and Yb^{3+} for efficient frequency upconversion", ***Applied physics letters***, Vol. 63, No. 24, (1993), 3268-3270.
7. Kishi, Y., Tanabe, S., "Infrared-to-visible upconversion of rare-earth doped glass ceramics containing CaF_2 crystals", ***Journal of Alloys and Compounds***, Vol. 408–412, (2006), 842–844.
8. Imanieh, M. H., Eftekhari Yekta, B., Marghussian, V., Shakhesi, S., Martín, I. R., "Crystallization of nano calcium fluoride in CaF_2-Al_2O_3-SiO_2 system", ***Solid State Sciences***, Vol. 17, (2013), 76-82.
9. Dejneka, M. J., "The luminescence and structure of novel transparent oxyfluoride glass-ceramics", ***Journal of Non-Crystalline Solids***, Vol. 239, No. 1-3, (1998), 149-155.
10. Antuzevics, A., Kemere, M., Ignatans, R., "Local structure of gadolinium in oxyfluoride glass matrices containing SrF_2 and BaF_2 crystallites", ***Journal of Non-Crystalline Solids***, Vol. 449, (2016), 29–33.

11. Hill, R. G., Goat, C., Wood, D., "Thermal Analysis of a SiO_2-Al_2O_3-CaO-CaF_2 Glass", ***Journal of the American Ceramic Society***, Vol. 75, No. 4, (1992), 778- 785.
12. Fu, J., Parker, J. M., Flower, P. S., Brown, R. M., "Eu^{3+} ions and CaF_2-containing transparent glass-ceramics", ***Materials Research Bulletin***, Vol. 37, No. 11, (2002), 1843-1849.
13. Sung, Y. M., "Crystallization kinetics of fluoride nanocrystals in oxyfluoride glasses", ***Journal of Non-Crystalline Solids***, Vol. 358, No. 1, (2012), 36-39.
14. Rüssel, C., "Nanocrystallization of CaF_2 from $Na_2O/K_2O/CaO/CaF_2/Al_2O_3/SiO_2$ glasses", ***Chemistry of Materials***, Vol. 17, No. 23, (2005), 5843-5847.
15. Rezvani, M., Farahinia, L., "Structure and optical band gap study of transparent oxyfluoride glass-ceramics containing CaF_2 nanocrystals", ***Materials & Design***, Vol. 88, (2015), 252–257.
16. Gautam, C. R., "Synthesis and optical properties of SiO_2–Al_2O_3–MgO–K_2CO_3–CaO–MgF_2–La_2O_3 glasses", ***Bulletin of Materials Science***, Vol. 39, No. 3, (2016), 677-682.
17. Nourbakhsh, Z., Lusk, M., Hashemifar, S. J., Akbarzadeh, H., "Nano structures of amorphous silicon: localization & energy gap", ***Iranian Journal of Physics Research***, Vol. 13, No. 3, (2013), 283 -287.
18. Mott, N. F., Davis, E. A., "Electronic processes in non-crystalline materials", Oxford university press, (2012).
19. Shakeri, M. S., Rezvani, M., "Optical band gap and spectroscopic study of lithium alumino silicate glass containing Y^{3+} ions", ***Spectrochimica Acta Part A: Molecular and Biomolecular Spectroscopy***, Vol. 79, No. 5, (2011), 1920-1925.
20. Lak, F., Rezvani, M., "Optical Characterization of BK7 Borosilicate Glasses Containing Different Amounts of CeO_2", ***Advanced Ceramics Progress***, Vol. 2, No. 3, (2016), 17-24.
21. Rezvani, M., Farahinia, L., "Structure and optical band gap study of transparent oxyfluoride glass-ceramics containing CaF_2 nanocrystals", ***Materials & Design***, Vol. 88, (2015), 252-257.
22. Rosenberg, H. M., "The solid state: an introduction to the physics of crystals for students of physics, materials science, and engineering", 3rd edition, Oxford University press, Oxford, (1988).
23. Abdel-Baki, M., Abdel-Wahab, F. A., Radi, A., El-Diasty, F., "Factors affecting optical dispersion in borate glass systems", ***Journal of Physics and Chemistry of Solids***, Vol. 68, No. 8, (2007), 1457- 1470.

ACERP: Vol. 6, No.2, (Spring 2020) 7-16

Advanced Ceramics Progress

Research Article

Journal Homepage: www.acerp.ir

Investigating the Abrasive Wear Resistance of Thermal-Sprayed WC-Based Coatings

S. M. Nahvi [a] *

[a] *Department of Materials Engineering, Isfahan University of Technology, Isfahan 84156-83111, Iran*

PAPER INFO

Paper history:

Received 1 April 2020
Accepted in revised form 13 April 2020

Keywords:

Abrasive Wear
WC–FeCrAl
WC–NiMoCrFeCo
HVOF

ABSTRACT

The purpose of this research was to investigate the abrasive wear behavior of WC–NiMoCrFeCo (WC-N) and WC–FeCrAl (WC-F) coatings deposited by high-velocity oxygen fuel (HVOF) spraying. The abrasive wear resistance was evaluated by a dry sand rubber wheel (DSRW) test rig using abrasives silica 70 and alumina 60, and the values were then compared to those of conventional WC-Co (WC-C) coatings. The abrasive wear with silica 70 indicated the "soft abrasion" regime, while alumina 60 abrasive caused a "hard abrasion" for all coatings. Moreover, the wear rate of the coatings abraded by alumina 60 was around 1.2-7.8 times greater than that of silica 70. WC-F exhibited the greatest wear resistance compared to other coatings tested by silica 70 due to its lower mean free path and higher hardness compared to other coatings. WC-C coating revealed the cobalt matrix removal followed by WC fracture and pullout using abrasive silica 70, while WC-F and WC-N coatings represented a combination of subsurface cracking, WC pullout, and fracture. Abraded by alumina 60, WC-C, WC-F, and WC-N coatings showed the evidence of grooving, pitting, and cutting. Moreover, WC-C coating had the highest wear resistance due to its high fracture toughness and low porosity, protecting WC-C coating against severe cracking and grooving, respectively. Cross-sectional images of the wear scars revealed a significant sub-surface cracking for WC-F and WC-N coatings while no significant cracking could be detected for WC-C coating.

1. INTRODUCTION

The superior composite structure of WC-Co thermal spray coatings includes a hard ceramic phase (WC) and a ductile metallic binder (Co). This structure provides an exceptional combination of high hardness, fracture toughness, and wear resistance, which makes them useful in a broad range of industrial applications such as seat and gate components in petroleum, pinch rolls, and bridle rolls in steel rolling, and aircraft landing gear in aerospace industries [1-5].

Among the common thermal spray techniques for WC-Co coatings deposition including air plasma spraying (APS), detonation spray coating (DSC), and high-velocity oxygen-fuel (HVOF) spraying, the latter provides higher velocity and lower temperature for in-flight particles and produces more compacted coatings with sustaining a larger fraction of retained WC phase [4]. In addition, HVOF-sprayed WC-Co coatings are considered as a viable alternative to hard chromium plating owing to their superior wear resistance and more environmentally friendly properties [5,6]. Nevertheless, the major concern in HVOF-sprayed WC-Co coatings is to control WC decarburization during the spraying process to avoid the formation of brittle phases, such as W_2C, metallic W, and nano-crystalline Co-W-C [7-9]. Numerous strategies have been implemented to control WC decarburization via the optimization of spray parameters [10-13], tailoring the composition of WC-Co powder [14,15], and utilizing metal-clad WC-Co powders [4,6,16,17]. The optimum wear resistance of WC-Co coatings is achievable in a microstructure including minimum WC decarburized and maximum retained WC particles distributed within the metallic cobalt matrix [18-21].

The abrasive wear resistance is one of the most important factors affecting the tribological performance of WC-based cermet coatings in a variety of practical conditions. For instance, the WC-Co coated cylinder rod

* Corresponding Author Email: mehran.nahvi@cc.iut.ac.ir (S. M. Nahvi)

https://doi.org/10.30501/acp.2020.107466

of landing gear is exposed to impact and adherence of sands and other hard particles imposing crucial damage to the coatings' surface during landing and ground operation of aircraft [5]. Previous works have mostly focused on the effect of WC carbide grain size on the abrasive wear behavior of HVOF-sprayed WC-Co coatings. For example, Stewart et al. [22] and Dent et al. [23] reported inferior abrasive wear resistance for nanostructured WC-Co compared to the conventional coarse-grained coatings due to the extensive dissolution and decarburization of nano-sized WC grains during HVOF spraying. In contrast, Saha et al. [24] and Baik et al. [17] reported an opposite trend for nanostructured WC-Co coatings deposited from Co-coated WC-Co powder. This behavior was attributed to the presence of the protective Co layer around individual nanostructured WC-Co powder particles, which reduces the interactions between HVOF flame and WC particles, and thereby, lowers the extent of decarburization [17,24].

The purpose of the present study was to evaluate the soft and hard abrasive behavior of the WC-based cermet HVOF sprayed coatings with complicated alloyed binders, i.e. WC–NiMoCrFeCo and WC–FeCrAl, using a dry sand rubber wheel testing and compare the outcomes of examinations with conventional WC-Co coatings. The microstructural and mechanical properties of these coatings have been studied in detail, and presented elsewhere [7].

2. EXPERIMENTAL PROCEDURES

2.1. THERMAL SPRAY PROCESS

Three different powders including WC-NiMoCrFeCo (WC-N), WC-FeCrAl (WC-F), and WC-Co (WC-C) were utilized as HVOF feedstock materials. All powders were agglomerated and sintered spheroids with the nominal diameters in the range of 15-45µm. WC grain size and chemical composition of the powders are presented in Table. 1.

TABLE 1. WC grain size and chemical composition of feedstock powders

Powder	Company	WC size (µm)	Composition (wt%)								
			W	Ni	Mo	Cr	Fe	Co	Al	C	O
WC-C (83-17%wt)	Sulzer Metco	1.0	77.98	-	-	-	0.04	16.82	-	5.16	-
WC-F (85-15%wt)	H.C. Starck	0.5	79.05	-	-	3.40	10.79	-	1.02	5.58	0.16
WC-N (85-15%wt)	H.C. Starck	0.7	79.97	8.47	2.24	2.15	0.84	0.62	-	5.65	0.06

Plain-carbon steel (0.12%C, 0.7%Mn) sheets with the hardness of 246$HV_{0.3}$ and dimensions of 59×25×3mm^3 were used as substrate. The substrates were cleaned and grit blasted with ~250µm brown alumina to degrease and roughen the surface. The feedstock powders were sprayed onto the substrates using a Praxair/UTP Top-Gun HVOF spray system with parameters listed in Table 2. Hydrogen and nitrogen were employed as the fuel and carrier gases, respectively. The sprayed samples were cooled with compressed air jets, and collected at the end of the treatment for subsequent characterization.

TABLE 2. Spray parameters employed for coating depositions

Spray Parameter	WC-C	WC-F	WC-N
O_2 flow rate (l min^{-1})	240	240	240
Fuel gas (H_2) flow rate (l min^{-1})	640	640	640
Carrier gas (N_2) flow rate (l min^{-1})	17	17	17
Spray distance (mm)	250	250	250
Number of pass	40	40	51
Length of pass (mm)	77	77	76
Carousel diameter (mm)	280	280	280
Substrate velocity (m s^{-1})	1	1	1
Gun transverse speed (mm s^{-1})	5	5	5
Coating time (s)	674	729	924
Consumption of powder (g)	710	635	555
Coating thickness (µm)	445	436	260
Powder feed rate (g min^{-1})	63	52	36

2.2. Abrasive wear evaluation

The samples were examined using a dry sand rubber wheel test rig modified by Stevenson and Hutchings to evaluate the coatings' behavior under three-body low-stress abrasion conditions [25]. As illustrated in Fig. 1, the coating samples were held in a slot at the top of the rotating wheel to control the feed of abrasive to be passed between the wheel and the sample.

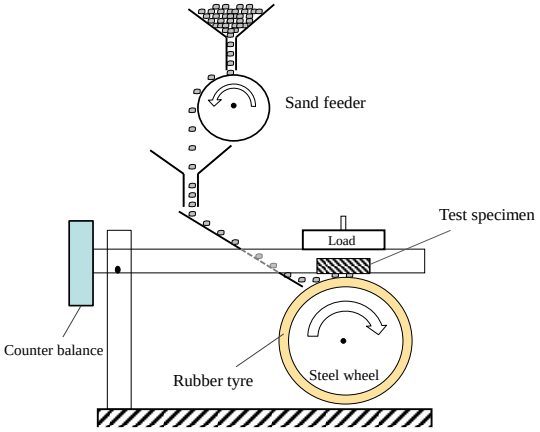

Figure 1. Schematic representation of dry sand rubber wheel abrasion test apparatus

The rubber wheel consisted of a cast polyurethane elastomer (monothane A60; CIL, Preston, UK) around an inner steel wheel with an overall diameter as much as 227mm. The tire had a width as much as 12mm and an international rubber hardness as much as 63±3 degrees as measured by a Wallace Hardness Meter. The rotation speed of the rubber was set at 195rpm, equivalent to a sliding speed of 2.32m.s^{-1}, according to ASTM standard G65 [26].

In this work, two types of abrasives were used:

1. Angular alumina 60 (Abrasive Developments, Henley-in-Arden, UK) with a size range as much as 212-300μm and sand feed rate of 2.64g.s^{-1};
2. Rounded silica 70 (The David Ball Company, Bar Hill, UK) with a size range as much as 180-250μm and sand feed rate of 2.37g.s^{-1} (Fig. 2).

The hardness of the abrasive particles was measured using a LECO M-400 microhardness tester with a 300gf load. The abrasive particles were mounted in a hot hardening resin and polished to preparation of a flat cross-section of the particles to indentation. The reported hardness value is the average value of 5 indents taken from different regions. The Vickers's hardness of silica 70 and alumina 60 abrasives measured on the polished cross-sections with a 300gf indentation load were 1138±47HV$_{0.3}$ and 2144±25HV$_{0.3}$, respectively.

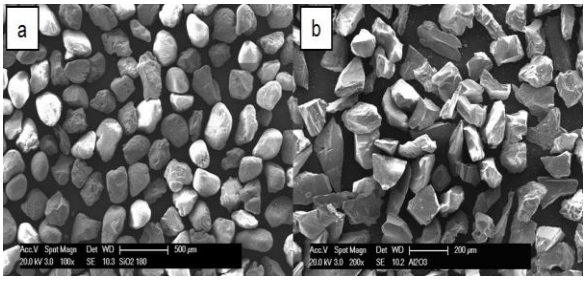

Figure 2. SEM micrograph of (a) silica 70 and (b) alumina 60 abrasive particles

In the wear behavior study, four different loadings of 19.6, 49, 98, and 127.5N were applied. The mass loss of the coatings was measured before and after each test using a GF-200 balance (A&D Instruments Ltd., Tokyo, Japan) with 10g capacity and 0.001g accuracy. Prior to the mass loss measurements, the coated samples were rinsed in methanol and dried. Abrasion distances of 800, 1600, 2400, 3200, and 4000 were considered for the coating samples. The wear rate was acquired from the gradient of the steady-state part of the mass loss versus sliding distance graph.

The worn surface of the coated samples was examined by an optical microscopy, scanning electron microscopy (Philips XL30, FEI Ltd, Cambridge, UK) with an accelerating voltage of 20kV in secondary electron (SE) and back-scattered electron (BSE) imaging modes to explore the wear mechanism of the coatings.

3. RESULTS

3.1. MICROSTRUCTURE AND MECHANICAL PROPERTIES

Detailed microstructural and mechanical properties of WC-C, WC-F, and WC-N coatings have already been reported [7]. Table 3 summarizes the most important microstructural and mechanical features of WC-C, WC-F, and WC-N coatings.

TABLE 3. Microstructural and mechanical properties of WC-C, WC-F, and WC-N coatings [7]

Coating	Carbide (vol%)	(W_2C/WC)	Carbon loss (%)	Porosity (vol %)	Microhardness ($HV_{0.3}$)	K_{IC} ($MPam^{1/2}$)
WC-C	55	9.14	30	1.8	1305 ± 71	5.9 ± 0.13
WC-F	58	12.48	16	5.1	1498 ± 82	3.1 ± 0.23
WC-N	59	40.42	36	2.2	1254 ± 38	2.8 ± 0.27

WC decarburization occurred during HVOF spraying of all materials designations. The minimum carbon loss was obtained for WC–F (16%), while WC–C and WC–N coatings experienced greater extents of decarburization of 30% and 36%, respectively. Cross-sectional SEM images exhibited a typical splat-like microstructure with dark and bright areas, which refers to the regions with lower, and higher mean atomic number, respectively. WC particles with angular morphology were observed in the darker areas of the matrix, indicating insignificant WC dissolution into the matrix. In the brighter regions, however, WC particles were observed with a more rounded morphology, which partially or fully enclosed by an irregular-shaped W_2C phase with brighter contrast [7].

The X-ray diffraction (XRD) analysis revealed that W_2C/WC peak ratio of WC–N (40.42%) is significantly higher than that of WC–F (12.48%) and WC–C (9.14%) coatings, indicating the highest level of W_2C phase formed in WC–N coating [7].

The WC–F coating showed the maximum micro-hardness (1498HV$_{0.3}$) compared to WC–C (1305HV$_{0.3}$) and WC–N (1254HV$_{0.3}$). The WC–N and WC–F coatings with almost identical volume fractions of carbide phases, comprising both the retained WC and newly precipitated W_2C (see Table 3), showed a significant difference in their hardness values. This can be explained by the lower carbon loss and W_2C/WC

ratio of WC–F coating leading to the higher fraction of retained WC phase in comparison to WC–N coating [7]. The cumulative distribution of the fracture toughness of the coatings revealed the higher fracture toughness of WC–C coating with the mean value of 5.9MPam$^{1/2}$ compared to WC–F and WC–N coatings with mean values of 3.1 and 2.8MPam$^{1/2}$, respectively [7].

3.2. ABRASIVE WEAR BEHAVIOR

3.2.1. ABRASIVE WEAR RATE

The abrasive wear rate of WC-C, WC-F, and WC-N coatings was determined using the least square fit method in the linear (steady-state) region. Steady-state wear rates of the coatings abraded by alumina 60 and silica 70 abrasives under the applied loads of 19.6, 49, 98, and 127.5 N are plotted in Fig. 3.

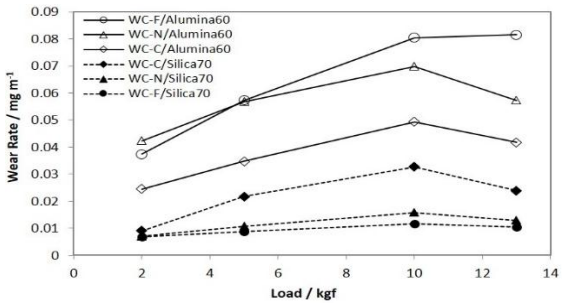

Figure 3. Variation of wear rate as a function of applied load for WC-C, WC-F, and WC-N coatings abraded by silica 70 and alumina 60

In all cases, the wear rate of the coatings abraded by alumina 60 is ~1.2-7.8 times higher than silica 70 abrasive. Hutchings et al. [27] reported that the wear rate is sensitive to the ratio of abrasive hardness (Ha) to the surface hardness (Hs); whereas, Ha/Hs>1.2 causes "hard abrasion" regime, while Ha/Hs<1.2 leads to "soft abrasion" one. Fig. 4 plots the Ha/Hs values for WC-C, WC-F, and WC-N coatings abraded by silica 70 and alumina 60. Obviously, the abrasive wear with alumina 60 is located in the "hard" abrasion region whereas silica 70 causes "soft" abrasion to all coatings. As for the coatings abraded by silica 70, WC-C showed the maximum wear rate of 0.0327mg.m^{-1} under 10kgf applied load, while the minimum wear rate in the range of 0.0069-0.0116mg.m^{-1} was obtained for WC-F coating.

The wear rate increased to the ranges of 0.0245-0.0493 and 0.0374-0.0698mg.m^{-1}, respectively in the case of WC-C and WC-N coatings abraded by alumina 60, with increasing the applied load from 2 to 10kgf. Further increase in the applied load to 13kgf resulted in the wear rate decline to 0.0417 and 0.0573mg.m^{-1} for WC-C and WC-N coatings, respectively. The wear rate of WC-F coating exhibits an upward trend from 0.0374 to 0.0804mg.m^{-1} with increasing the applied load from 2 to 10kg followed by a marginal increase to 0.0815mg.m^{-1} with further load rising to 13kgf.

Accordign to Fig. 3, it is obvious that the type of abrasive significantly affects the abrasive wear resistance of the coatings; e.g., WC-F and WC-C present the highest wear resistance for silica 70 and alumina 60, respectively.

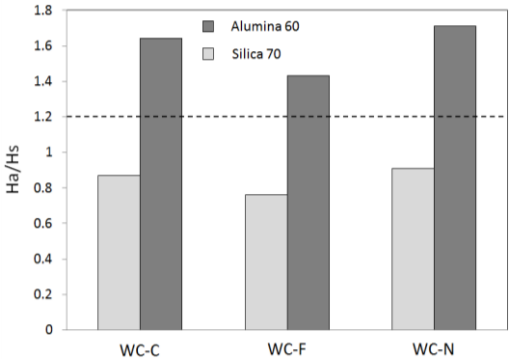

Figure 4. Plot showing transition between "hard" and "soft" abrasive wear mechanisms ($\frac{H_a}{H_s} = 1.2$) for the coatings abraded by silica 70 and alumina 60

3.2.2. WEAR SCAR STUDY

Fig. 5 (a,b) illustrates the optical microscopy images from the central zone of wear scar of WC-F coating abraded by silica 70 at the lowest and highest applied load, namely 19.6N and 127.5N, respectively. The worn surface reveals the evidence of particle rolling with significant indentation of the surface. In contrast, WC-F coating abraded by alumina 60 experiences particle sliding (grooving) along with small particle rolling across the surface (Fig. 5 (c,d)). Optical microscope analysis of other coatings indicated that silica 70 abrasive results in the particles rolling, while alumina 60 abrasive leads to grooving on the worn surface under all applied loads. Fig. 5 also confirms that the size of indentations, and grooves increase with increasing the applied load.

The plan view SEM images of the wear scars of WC-C coating after abrasion with silica 70 at the lowest and the highest applied loads, namely 19.6N and 127.5N, respectively are demonstrated in Fig. 6 (a,b). Wear scar produced under both loads exhibited removal of cobalt matrix at the higher rate and leaving unprotected carbide particles on the worn surface followed by carbide cracking and pullout, which were more significant under the greater applied load (127.5N). As illustrated in the cross-sectional SEM images under the highest load (Fig. 6c), not only the sub-surface cracking was not significant, but also the carbide grains were standing

proud of the matrix indicating preferential wear of the matrix phase. The carbide cracking combined with void formation is also apparent in Fig. 6c.

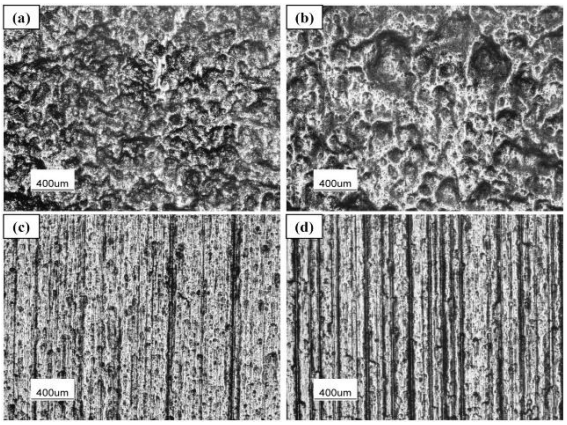

Figure 5. Optical microscopy images of WC-F coating abraded by (a) silica 70 under 19.6N, (b) silica 70 under 127.5N, (c) alumina 60 under 19.6N, and (d) alumina 60 under 127.5N

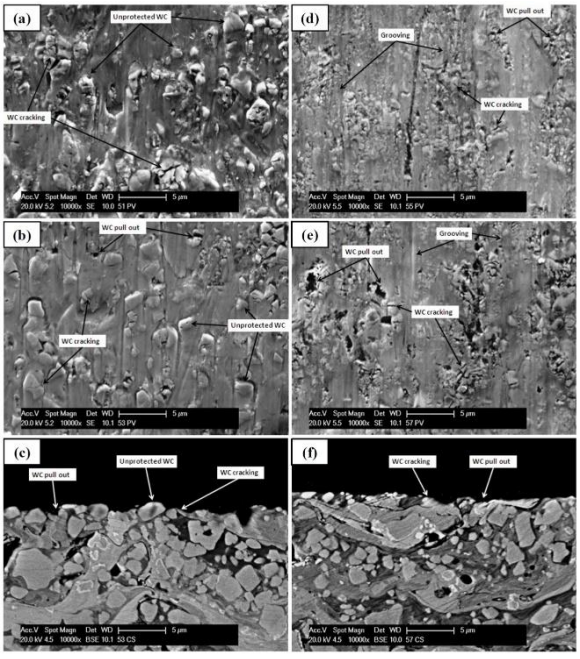

Figure 6. (a,b) Plan view SEM images from wear scar of WC-C coating after abrasion by silica 70 under 19.6 and 127.5N, respectively. (c) Cross-sectional SEM image from wear scar of WC-C coating after abrasion by silica 70 under 127.5N. (d,e) Plan view SEM images from wear scar of WC-C coating after abrasion by alumina 60 under 19.6 and 127.5N, respectively. (f) Cross-sectional SEM image from wear scar of WC-C coating after abrasion by alumina 60 under 127.5N

Fig. 6 (d,e) demonstrates the plan view SEM images of WC-C coating abraded by alumina 60 under 19.6N and 127.5N loads, respectively. Two distinct regions owing low and high density of carbides accompanied by the evidence of grooving, fractured carbide grains, and voids can be detected in Fig. 6 (d,e)due to the carbide pullout. The higher the applied load, the greater the number of voids and cracked carbides appeared on the worn surface. The cross-section of WC-C worn surface abraded by alumina 60 under the highest load (127.5N) (Fig. 6f) exhibits only some small surface pits and no subsurface cracking can be observed.

Fig. 7 (a,b) shows the plan view SEM images from the central zone of the worn surface of WC-F coating abraded by silica 70 at the lowest and the highest loads, namely 19.6N and 127.5N, respectively.

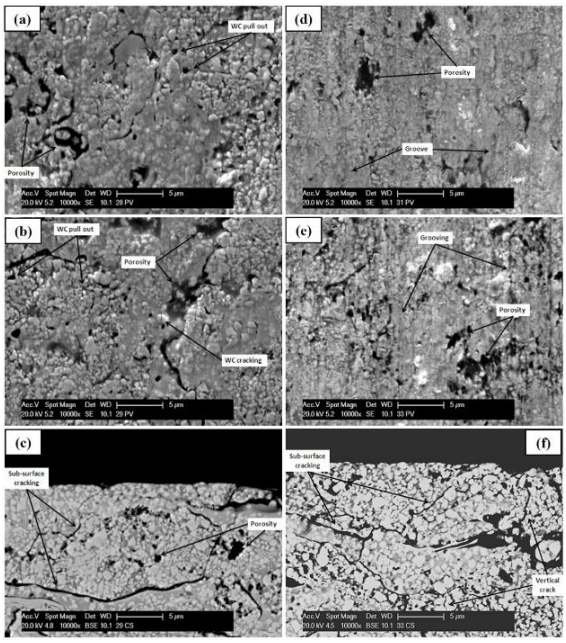

Figure 7. (a,b) Plan view SEM images from wear scar of WC-F coating after abrasion by silica 70 under 19.6 and 127.5N, respectively. (c) Cross-sectional SEM image from wear scar of WC-F coating after abrasion by silica 70 under 127.5N. (d,e) Plan view SEM images from wear scar of WC-F coating after abrasion by alumina 60 under 19.6 and 127.5N, respectively. (f) Cross-sectional SEM image from wear scar of WC-F coating after abrasion by alumina 60 under 127.5N

Many cracks and voids are observed on the wear scar under both applied loads. According to Table 3, the pullout process cannot be easily distinguished because of the high level of porosity in WC-F coating (5.1%). In addition, the metal matrix seems to be exposed to abrasion at a slightly higher rate at which leaves unprotected carbide particles visible in the plan view images (Fig. 7a and b). The cross-sectional SEM image of the worn surface of WC-F coating abraded by silica 70 under the highest applied load (127.5N) is shown in Fig. 7c. The sub-surface crack propagating through the

coating's sub-layers with inherent porosity of the coating is visible in the cross-sectional view of WC-F coating. However, qualitatively good adhesion is apparent between carbide grains and the matrix.

The plan view SEM images of WC-F coating abraded by alumina 60 under 19.6N and 127.5N loads (Fig. 7 (d,e)) display the evidence of grooves and large voids on the worn surface related to either materials loss or presence of open porosities on the coating's surface. Grooving and void formation is more obvious for WC-F coating tested under higher load (127.5N). Besides, the cross-sectional image of the WC-F worn surface (Fig. 7f) reveals a continuous network of cracking along with a wide area of porosity at the sub-surface layer.

Fig 8 (a,b) shows the plan view SEM images from wear scar of WC-N coating abraded by silica 70 under the lowest and highest applied loads, namely 19.6N and 127.5N.

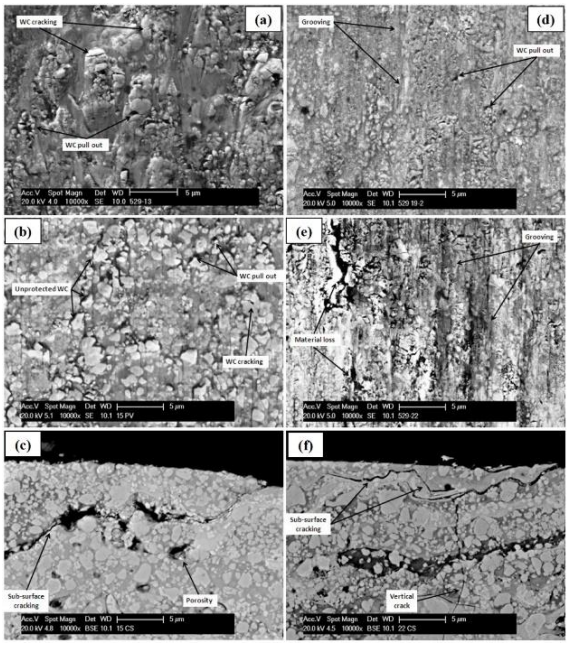

Figure 8. (a,b) Plan view SEM images from wear scar of WCN coating after abrasion by silica 70 under 19.6 and 127.5N, respectively. (c) Cross-sectional SEM image from wear scar of WC-N coating after abrasion by silica 70 under 127.5N. (d,e) Plan view SEM images from wear scar of WC-N coating after abrasion by alumina 60 under 19.6 and 127.5N, respectively. (f) Cross-sectional SEM image from wear scar of WC-N coating after abrasion by alumina 60 under 127.5N

The carbide cracking and pullout are the main abrasive wear mechanisms for the WC-N coating. This mechanism takes place following the faster removal of the metal matrix; hence, the carbide particles are no longer supported by the matrix leading to their pullout and cracking during abrasive wear [16]. The cross-sectional SEM image (Fig. 8c) indicates the good adhesion of carbide particles to the matrix at the subsurface layers of WC-N coating. Besides, sub-surface cracking and porosity are evident in the cross-sectional image of WC-N wear scar.

SEM images of worn surface of WC-N coating abraded by alumina 60 are presented in Fig. 8(d-f). The plan view images under the applied loads of 19.6N (Fig. 8d) and 127.5N (Fig. 8e) show cutting and grooving of both the binder and carbide, with the larger and deeper grooves at the higher load leading to a significant material removal from the worn surface of WC-N coating. The cross-sectional SEM image of the worn surface (Fig. 8f) reveals the evidence of vertical and sub-surface crack propagation through the binder phase.

4. DISCUSSION

4.1. GENERAL OBSERVATIONS

As plotted in Fig. 3, the abrasive wear rate of WC-C, WC-F, and WC-N coatings exhibits an increasing trend with the applied load for both silica 70 and alumina 60 abrasives. However, there is an exception in this trend at 127.5N for several coatings in which the wear rate is unexpectedly reduced. The temperature of both sample and wheel increase during dry sand rubber wheel test depending on various parameters including the abrasive type, sample material, and testing load [28]. The rubber temperature rising as a function of the applied load will result in decreasing its hardness followed by the reduction in wear rate at 127.5N [25].

The abrasive hardness to coating hardness ratio indicated the "hard abrasive wear" by alumina 60 and the "soft abrasive wear" by silica 70 (Fig. 4) indicating significantly lower wear rates with the silica 70 abrasives compared to alumina 60 for all coatings and all examined test conditions (Fig. 3). In addition, low magnification optical microscopy images of the coatings (Fig. 5 (a,c)) indicate particle rolling with significant indentation of the surface caused by silica 70 abrasives, while the alumina 60 resulted in grooves along the direction of abrasive flow. The size of indentations, and grooves increase by increasing the applied load (Fig. 5 (b,d)). The greater hardness and the angular morphology of the alumina 60 compared to the more rounded silica 70 particles (see Fig. 2) can be considered as the main reasons for the significant difference in the wear behavior of the coatings.

Fig. 9 (a,b) displays the wear rate of WC-C, WC-F, and WC-N coatings abraded by silica 70 and alumina 60 as a function of the hardness of the coatings.

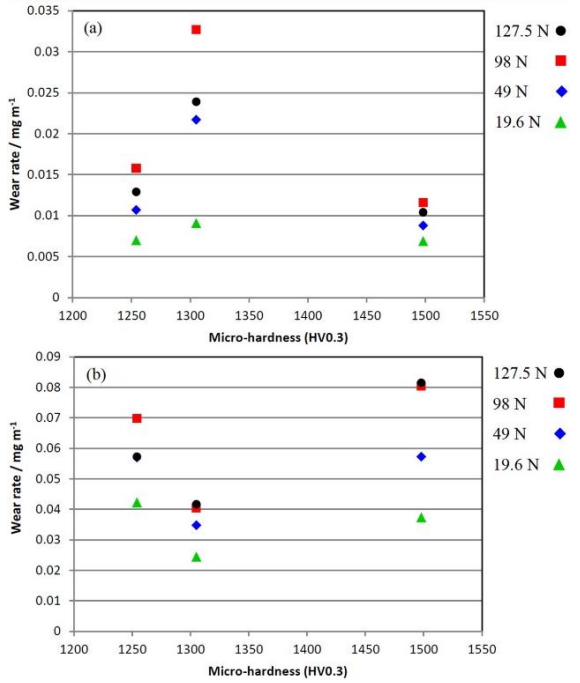

Figure 9. Variation of wear rate as a function of microhardness for WC-C (1305$HV_{0.3}$), WC-F (1498$HV_{0.3}$), and WC-N (1254$HV_{0.3}$) coatings braded by (a) silica 70 and (b) alumina 60

According to plots presented in Fig. 9, the wear rate of the coatings is not necessarily deceased with increasing the hardness of the coatings. For instance, the wear rate of WC-C coating abraded by silica 70 is generally greater than that of WC-N coating despite the higher hardness of the WC-C coating compared to WC-N one (Fig. 9a). Notably, this trend will be reversed by exposing the coatings under abrasion by alumina 60; i.e. WC-N coating with lower hardness suffers from more damage and materials removal as compared to WC-C coating. This can be referred to the complicated mechanism of abrasive wear in thermally sprayed cermet coatings, which make the type of abrasive as a key factor determining the abrasion wear resistance of the coatings.

The WC-C, WC-F, and WC-N coatings can be classified into two groups with distinct characteristics:

Co-group (WC-C) and non-Co-group (WC-F and WC-N). Each group exhibits similar characteristics in the feedstock powder and the resultant coating.

Co-group mostly contains 83wt% WC, while this amount is 85wt% for non-Co-group [7]. Moreover, the carbide shape in the non-Co-group seems to be rounded as compared to the angular carbide grains in the Co-group [7]. Finally, the binder material in the starting powder is a pure metal (Cobalt) for Co-group, whereas there are two complicated alloys (Hastelloy type C for WC-N and Kanthal for WC-F) for non-Co-group as the binder materials [7].

Similar properties of the coatings in each group include:

i) High fracture toughness for Co-group (WC-C: 5.9±0.13MPa.$m^{1/2}$) and low fracture toughness for non-Co-group (WC-F: 3.1±0.23 and WC-N: 2.8±0.27MPa.$m^{1/2}$);

ii) Low porosity for Co-group (WC-C: 1.8%) and high porosity for non-Co-group (WC-F: 5.1% and WC-N: 2.2%);

iii) Higher W_2C and lower amorphous phases in non-Co-group as compared to Co-group [7];

iv) High mean free path for Co-group (WC-C: 0.68µm) and low mean free path for non-Co-group (WC-F: 0.31µm and WC-N: 0.4µm);

v) The high volume fraction of carbide phase for non-Co-group (WC-F: 58% and WC-N: 59%) and lower carbide volume fraction for Co-group (WC-C: 55%).

Based on the abovementioned differences between feedstock powder and coatings of Co-group and non-Co group, the abrasive wear mechanisms of the coatings abraded by silica 70 and alumina 60 can be explained according to the next part of this research.

4.2. ABRASIVE WEAR WITH SILICA 70

The silica 70 abrasives with the lowest hardness compared to other coatings examined (1138±47$HV_{0.3}$) exhibits a rounded morphology with a narrow size distribution. The abrasive hardness (H_a) to the hardness of thr coatings (H_s) ratio is less than 1.2 indicating "soft wear" regime and, as such, particle blunting is most probable during abrasion process resulting in a lower rate of wear under three-body (rolling) abrasion mechanism as compared to the harder abrasive particles. The selective binder phase removal from the near-surface layer is considered as a substantial stage in the wear process of composite materials abraded by soft abrasives [29]. Cyclic indenting contact of abrasive particles during the three-body abrasion process imposes compressive stresses at the surface of the coatings. As a result, the support of the binder is no longer possible for WC particles as parts of the binder are initially extruded out of the surface followed by damage to WC grains located in heavily loaded regions, where the binder phase is abraded. This leads to WC fracture into smaller particles and their gradual pullout from the surface. The situation will be more complicated and the damage will be more severe for WC grains located at the edge of defects such as cracks or areas of surface damage where a greater load is imposed by abrasive particles resulting in the growth of the defects. Consequently, micro-cracks preferentially propagate around the pits and through the W-rich binder phase or along splat boundaries. Elastic-plastic indentation of the abrasive may also form sub-surface cracks into the coating, the propagation of which leads to detachment of fragments of the surface of coatings [30]. The crack initiation caused at the end of an empty space by binder phase removal or carbide grains pullout is observed in

the cross-sectional SEM images of the coatings (e.g., Fig. 7c) indicating crack propagation mostly through the W-rich binder phase or splat boundaries.

The plan view and cross-sectional SEM images are shown in Fig. 6 (a-c). The cobalt matrix removal followed by WC fracture and pullout is the prevalent abrasive wear mechanisms for Co-group (WC-C coating) abraded by silica 70, while limited evidence of micro-grooving and sub-surface cracking were observed indicating the high fracture toughness of Co-group ($5.9\pm0.13 MPa.m^{1/2}$) and high resistance to crack initiation and propagation.

A combination of subsurface cracking, WC pullout, and the fracture was observed for non-Co-group during abrasive wear by silica 70 (see Fig. 7 (a-c) and Fig. 8 (a-c)). The higher density of subsurface cracking could be attributed to the higher porosity and W_2C/WC ratio in non-Co-coatings compared to Co-group leading to lower fracture toughness (WC-F: $3.1\pm0.23 MPa.m^{1/2}$ and WC-N: $2.8\pm0.27 MPa.m^{1/2}$) [7].

Non-Co-group abraded by silica 70 particles showed superior wear resistance compared to Co-group.

It has been reported that there is a relationship between abrasion resistance and the mean free path of the binder phase between the carbide grains for the cemented materials. This means that a short mean free path caused by a high volume fraction of fine carbide grains, leads to the highest abrasion resistance [31]. A similar result has been reported for HVOF thermally sprayed WC-based coating abraded by a dry sand rubber wheel test indicating the best abrasion resistance for the coating with the lowest the mean free path [32]. The comparison between mean free path of Co-group (WC-C: 0.68µm) and non-Co-group coatings (WC-F: 0.31µm and WC-N: 0.4µm) reveals significantly lower values for the latter group resulting in their superior abrasion wear resistance.

The abrasive wear behavior of both WC-F and WC-N Coatings (non-Co-group) abraded by silica 70 follows the soft wear regime with low wear rates. It should be noted that the wear rate of WC-N coating is faster than the WC-F one. The greater wear resistance of WC-F could be justified by its lower mean free path and higher hardness as compared to WC-N coating (Table 3).

4.3. ABRASIVE WEAR WITH ALUMINA 60

Alumina 60 abrasive with the highest hardness among the examined coatings (2144±25HV0.3) exhibits an angular morphology with a narrow size range (Fig. 2). The abrasive hardness H_a to the hardness of the coating H_s ratio is more than 1.2 indicating the "hard wear" regime. Abrasive particles cause the plastic deformation mostly by plastic ploughing and cutting accompanied by some local fracture in the more brittle composites under hard abrasive conditions [27].

The worn surface of WC-C, WC-F, and WC-N coatings produced by alumina abrasive (Figs. 6-8 (d-f)) shows the evidence of grooving, pitting, and cutting. The cross-sectional images of the wear scars also indicate a significant sub-surface cracking for WC-F and WC-N coatings while no significant cracking can be detected for WC-C coating, which indicates the high fracture toughness of WC-C coating compared to non-Co coatings. According to the results, two main wear mechanisms can be considered in materials including plastic deformation and fracture. The passage of the hard and sharp abrasives causes the plastic deformation of the surface at the first stage of the abrasion process resulting in the formation of grooves with materials pile up at the groove edges.

A plastic groove forms during embedding and sliding of sharp particles into the surface at the first stage of wear. The penetration extent of the abrasive particles into the surface is different for each coating.

The residual stresses caused by deformation drive the lateral cracks to grow upwards through the coating.

Cross-sectional SEM images of the wear scars of WC-F and WC-N coatings reveal that the subsurface cracks propagate parallel to the top surface of the coatings (Fig. 7f, Fig. 8f). Two types of cracks can be formed due to the low fracture toughness of WC-F and WC-N coatings: Horizontal cracks along the surface and vertical cracks perpendicular to the surface. According to the argument of Stewart et al. [22], formation of vertical cracks caused by the indentation of the abrasive into the coating is the initial stage of the material loss procedure. The vertical cracks run down through the coating and end upon reaching either a region of the W-rich binder phase or a splat boundary. The next step is the crack propagate parallel to the coating surface to reach the surface. In general, this process results in high materials removal in the coatings with low fracture toughness (non-Co-group).

At the second stage, the fatigue of the surface layers and fracture can occur through mechanical deformation leading to the spalling type of failure. A comparison between Co-group and non-Co-group reveals that the fracture mechanism plays more significant role in the wear of the latter owing to its lower fracture toughness that leads to the higher wear rate of WC-F and WC-N coatings compared to WC-C one, as plotted in Fig. 3. In addition, the higher porosity of non-Co-group coatings than Co-group ones can be considered as an important factor in creating more grooves followed by greater material removal.

In summary, WC-C coating exhibited the optimum wear resistance among the coatings abraded by alumina 60 abrasive due to the high fracture toughness and low porosity and protection of WC-C coating against severe cracking and grooving, respectively.

However, the lowest abrasive wear resistance was obtained as for WC-F coating. WC-F is a coating with

high hardness. Nevertheless, the presence of plenty of porosities makes it a coating with low fracture toughness resulting in a large number of grooves at the first stage of the abrasion process and severe cracking at the second stage. Therefore, the wear resistance of WC-F coating is less than other coatings examined, namely WC-C and WC-N.

5. CONCLUSIONS

In this study, the abrasive wear behavior of two advanced WC-based coatings, WC–NiMoCrFeCo (WC-N) and WC–FeCrAl (WC-F), deposited by a Top Gun HVOF system was examined under a soft and hard abrasion regime. The outcomes of investigations were compared to conventional WC-Co (WC-C) coating, as well. The main conclusions can be drawn as follows:

(1) The abrasive wear with silica 70 was located in the "soft abrasion" regime for all coatings, while alumina 60 abrasive imposed a "hard abrasion" regime. Moreover, the wear rate of the coatings abraded by alumina 60 was ~1.2-7.8 times higher than silica 70 abrasive.
(2) Among the coatings tested by silica 70, WC-F exhibited the superior wear resistance owing to its lower mean free path and higher hardness as compared to other coatings.
(3) In the case of Co-group (WC-C) coating abraded by silica 70, the cobalt matrix removal followed by WC fracture and pullout were the prevalent abrasive wear mechanisms. As for non-Co-group coatings (WC-F and WC-N), a combination of subsurface cracking, WC pull-out, and the fracture was operating during abrasive wear by silica 70.
(4) WC-C coating revealed the highest wear resistance relative to other coatings when abraded by alumina 60. This was caused by its high fracture toughness and low porosity, which protect WC-C coating against severe cracking and grooving, respectively.
(5) Examination of the worn surface of WC-C, WC-F, and WC-N coatings after abrasion by alumina 60 showed the evidence of grooving, pitting, and cutting. The cross-sectional images of the wear scars also revealed a significant sub-surface cracking for WC-F and WC-N coatings while no significant cracking was detected for WC-C coating.

6. ACKNOWLEDGEMENTS

The author sincerely appreciate Professors Philip Shipway and Graham McCartney from Department of Mechanical, Materials, and Manufacturing Engineering, The University of Nottingham, UK, for their supervision, advice and encouragement throughout this research.

REFERENCES

1. Yuan, J., Ma, C., Yang, S., Yu, Z., Li, H., "Improving the wear resistance of HVOF sprayed WC-Co coatings by adding submicron-sized WC particles at the splats' interfaces", ***Surface and Coatings Technology***, Vol. 285, (2016), 17-23.
2. Trpčevská, J., Ganev, N., Żórawski, W., Jakubeczyova, D., Briančin, J., "Effect of powder particle size on the structure of HVOF WC-Co sprayed coatings", ***Powder Metallurgy Progress***, Vol. 9, No. 1, (2009), 42-48.
3. Stewart, D. A., Shipway, P. H., McCartney, D. G., "Microstructural evolution in thermally sprayed WC-Co coatings: comparison between nanocomposite and conventional starting powders", ***Acta Materialia***, Vol. 48, No. 7, (2000), 1593-1604.
4. Mateen, A., Saha, G. C., Khan, T. I., Khalid, F. A., "Tribological behaviour of HVOF sprayed near-nanostructured and microstructured WC-17wt.% Co coatings", ***Surface and Coatings Technology***, Vol. 206, No. 6, (2011), 1077-1084.
5. Gong, T., Yao, P., Zuo, X., Zhang, Z., Xiao, Y., Zhao, L., Zhou, H., Deng, M., Wang, Q., Zhong, A., "Influence of WC carbide particle size on the microstructure and abrasive wear behavior of WC–10Co–4Cr coatings for aircraft landing gear", ***Wear***, Vol. 362-363, (2016), 135-145.
6. Jafari, M., Enayati, M. H., Salehi, M., Nahvi, S. M., Park, C. G., "Microstructural and mechanical characterizations of a novel HVOF-sprayed WC-Co coating deposited from electroless Ni–P coated WC-12Co powders", ***Materials Science and Engineering: A***, Vol. 578, (2013), 46–53.
7. Nahvi, S. M., Jafari, M., "Microstructural and mechanical properties of advanced HVOF-sprayed WC-based cermet coatings", ***Surface and Coatings Technology,*** Vol. 286, (2016), 95-102.
8. Berger, L. M., "Applications of hardmetals as thermal spray coatings", ***International Journal of Refractory Metals and Hard Materials***, Vol. 49, (2015), 350-364.
9. Park, S. Y., Kim, M. C., Park, C. G., "Mechanical properties and microstructure evolution of the nano WC–Co coatings fabricated by detonation gun spraying with post heat treatment", ***Materials Science and Engineering: A***, Vol. 449-451, (2007), 894-897.
10. Myalska, H., Moskal, G., Szymański, K., "Microstructure and properties of WC-Co coatings, modified by sub-microcrystalline carbides, obtained by different methods of high velocity spray processes", ***Surface and Coatings Technology***, Vol. 260, (2014), 303-309.
11. Qiao, Y., Fischer, T. E., Dent, A., "The effects of fuel chemistry and feedstock powder structure on the mechanical and tribological properties of HVOF thermal-sprayed WC-Co coatings with very fine structures", ***Surface and Coatings Technology***, Vol. 172, No. 1, (2003), 24-41.
12. Picas, J. A., Punset, M., Baile, M. T., Martín, E., Forn, A., "Effect of oxygen/fuel ratio on the in-flight particle parameters and properties of HVOF WC-CoCr coatings", ***Surface and Coatings Technology***, Vol. 205, (2011), S364-S368.
13. Sobolev, V. V., Guilemany, J. M., Nutting, J., "High velocity oxy-fuel spraying: Theory, structure-property relationships and applications", London: Maney Publishing, (2004).
14. De Villiers Lovelock, H. L., "Powder/processing/structure relationships in WC-Co thermal spray coatings: A review of the

published literature", ***Journal of Thermal Spray Technology***, Vol. 7, No. 3, (1998), 357-373.

15. Yuan, J., Zhu, Y., Zheng, X., Ruan, Q., Ji, H., "Improvement in tribological properties of atmospheric plasma-sprayed WC-Co coating followed by Cu electrochemical impregnation", ***Applied Surface Science***, Vol. 255, No. 18, (2009), 7959-7965.
16. Jafari, M., Enayati, M. H., Salehi, M., Nahvi, S. M., Hosseini, S. N., Park, C. G., "Influence of nickel-coated nanostructured WC-Co powders on microstructural and tribological properties of HVOF coatings", ***Journal of Thermal Spray Technology***, Vol. 23, No. 8, (2014), 1456-1469.
17. Baik, K. H., Kim, J. H., Seong, B. G., "Improvements in hardness and wear resistance of thermally sprayed WC-Co nanocomposite coatings", ***Materials Science and Engineering: A***, Vol. 449-451, (2007), 846-849.
18. Saha, G. C., Khan, T. I., "The corrosion and wear performance of microcrystalline WC-10Co-4Cr and near-nanocrystalline WC-17Co high velocity oxy-fuel sprayed coatings on steel substrate", ***Metallurgical and Materials Transactions A***, Vol. 41, No. 11, (2010), 3000–3009.
19. Aristizabal, M., Rodriguez, N., Ibarreta, F., Martinez, R., Sanchez, J. M., "Liquid phase sintering and oxidation resistance of WC–Ni–Co–Cr cemented carbides", ***International Journal of Refractory Metals and Hard Materials***, Vol. 28, No. 4, (2010), 516–522.
20. Birks, N., Meier, G. H., Pettit, F. S., "Introduction to the High-Temperature Oxidation of Metals", 2nd ed., Cambridge University Press: UK, (2006).
21. Nerz, J., Kushner, B., Rotolico, A., "Microstructural Evaluation of Tungsten Carbide-Cobalt Coatings", ***Journal of Thermal Spray Technology***, Vol. 1, No. 2, (1992), 147-152.
22. Stewart, D. A., Shipway, P. H., Mccartney, D. G., "Abrasive wear behaviour of conventional and nanocomposite HVOF-sprayed WC–Co coatings", ***Wear***, Vol. 225–229, (1999), 789–798.
23. Dent, A. H., Depalo, S., Sampath, S., "Examination of the wear properties of HVOF sprayed nanostructured and conventional WC–Co cermets with different binder phase contents", ***Journal of Thermal Spray Technology***, Vol. 11, No. 4, (2002), 551–558.
24. Khan, T. I., Saha, G., Glenesk, L. B., "Nanostructured composite coatings for oil sands applications", ***Surface Engineering***, Vol. 26, No7, (2010), 540-545.
25. Stevenson, A. N. J., Hutchings, I. M., "Development of the dry sand rubber wheel abrasion test", ***Wear***, Vol. 195, No. 1-2, (1996), 232-240.
26. ASTM G 65-00, "Standard Test Method for Measuring Abrasion Using the Dry Sand/Rubber Wheel Apparatus", ASTM International West Conshohocken, PA., (2000), 256-267.
27. Hutchings, I. M., Shipway, P. H., "Tribology: friction and wear engineering materials", Oxford: Butterworth-Heinemann, (2017), 273.
28. Nahvi, S. M., Shipway, P. H., McCartney, D. G., "Particle motion and modes of wear in the dry sand-rubber wheel abrasion test", ***Wear***, Vol. 267, No. 11, (2009), 2083-2091.
29. Blombery, R. I., Perrot, C. M., Robinson, P. M., "Abrasive wear of tungsten carbide-cobalt composites. I. Wear mechanisms", ***Materials Science and Engineering,*** Vol. 13, No. 2, (1974), 93-100.
30. Chen, H., Xu, C., Zhou, Q., Hutchings, I. M., Shipway, P. H., Liu, J., "Micro-scale abrasive wear behaviour of HVOF sprayed and laser-remelted conventional and nanostructured WC-Co coatings", ***Wear***, Vol. 258, No. 1-4, (2005), 333-338.
31. Larsen-Basse, J., "Effect of composition, microstructure, and service conditions on the wear of cemented carbides", ***The Journal of the Minerals, Metals & Materials Society (JOM)***, Vol. 35, No. 11, (1983), 35-42.
32. Kumari, K., Anand, K., Bellacci, M., Giannozzi, M., "Effect of microstructure on abrasive wear behaviour of thermally sprayed WC-10Co-4Cr coatings", ***Wear***, Vol. 268, No. 11-12, (2010), 1309-1319.

ACERP: Vol. 6, No.2, (Spring 2020) 17-23

Advanced Ceramics Progress

Research Article

Journal Homepage: www.acerp.ir

Studying the Optical Density, Topography, and Structural Properties of CZO and CAZO Thin Films at Different Annealing Temperatures

N. Rahimi [a], V. Dalouji [a *], A. Souri [b]

[a] *Department of Physics, Faculty of Science, Malayer University, Malayer, Iran*
[b] *Department of Materials Engineering, Faculty of Engineering, Malayer University, Malayer, Iran*

PAPER INFO

Paper history:

Received 23 February 2020
Accepted in revised form 23 April 2020

Keywords:

The CAZO Thin Films
Fractal Dimensions
Topography
Optical Density
Bearing Area

ABSTRACT

In this paper, CAZO and CZO thin films were deposited on quartz substrates by radio frequency magnetic sputtering and annealed at different temperatures of 400, 500, and 600°C. One of the most structural studies of thin-film materials is the analysis of the results that are obtained from AFM images. The most variations in optical density of CZO and CAZO thin films were at energy points to about 3eV and 4eV, respectively. Fractal dimensions and structural properties of films, as well as the optical density of CZO and CAZO thin films, were investigated. The AFM images were used to estimate the lateral size of the nanoparticles on the surface of the films. Annealed films at 500°Chad the maximum values for the lateral size of the nanoparticles. These values for the as-deposited films and annealed films at different temperatures of 400, 500, and 600°C were about 7.9,8.1, 6.5, and 7.75nm for CZO thin films, respectively. In addition, the lateral size of CAZO thin films was about 6.8, 6.27, 6.04, and 6.71, respectively. Films that annealed at 500°Chad the minimum value of fractal dimensions. The power spectral density of all films reflects the inverse power low variations, especially in the high spatial frequency region, indicating the presence of fractal components in prominent topographies. The maximum variations in the bearing area were as much as 0.015μm and 0.01μm for CZO thin films and CAZO thin films, respectively.

1. INTRODUCTION

Nowadays, nanomaterials play an important role in different branches of science, such as materials, industry, and chemistry [1-9]. The zinc oxide thin films were applied extensively in optoelectronics, Transparent Conductive Oxide (TCO) films transistors, and biosensors [10,11]. One of the most structural studies of thin-films materials were obtained from AFM images [12]. Extensive efforts have been made to develop the next-generation of optoelectronic devices based on transparent conductive materials that are gaining more attention due to their electrical and optical properties [13]. They are used as appropriate materials for various applications, including light-emitting diodes, solar cells, and gas sensors [14-17]. ZnO is an n-type semiconductor that has been attempted to utilize various elements such as Cr, Co, Ni, M, or Fe in ZnO to improve its electrical properties. CuO [18] and Cu_2O_4 [19, 20] have a thin band of 1.2 and 2.2V, respectively. The ionic atoms (Cu^{+1} and Cu^{+2}) are replaced to Zn^{+2} in CZO thin films, which facilitates the alternatives at the Zn site. The different methods such as sol-gel and Radio Frequency (RF)-magnetron sputtering have been used to obtain Cu-doped ZnO thin films [21,22]. Aluminum doped zinc oxide films were prepared by a variety of techniques such as evaporation [23, 24] metal-organic chemical vapor deposition (MOCVD) [25], RF sputtering [19], Sol-gel [26, 27], heat dissipation [28-30], pulsed laser deposition (PLD) [31], and magnetron sputtering [32-36]. Cu-Al-doped ZnO thin films, which are weak magnetic semiconductors, are good candidates as a source of polar rotations and ferromagnetism generation at room temperature [37]. In the previous report by the researchers of this paper [38], the relation between the fractal dimensions of carbon-nickel films regarding their electrical properties were studied in details.

In this work, the effect of doping content and nanoparticle distribution in CZO and CAZO thin films

* Corresponding Author E-mail: Dalouji@yahoo.com (V. Dalouji)
https://doi.org/10.30501/acp.2020.107466

were studied on optical density, surface topography, and the fractal dimensions of films.

2. EXPERIMENTAL PROCEDURE

In this study, the CZO and CAZO films were deposited on quartz substrates by radio frequency magnetron sputtering at room temperature, and then, they were annealed at 400, 500, and 600ºC in Ar atmosphere. The sputtering gas was Ar and O_2 with the (O_2/O_2 + Ar) ratio of 30%, which remained constant during the operation by employing two rotary and turbo pumps. The base pressure of the sputtering chamber was less than 2×10^{-5}mbar. The working pressure was fixed at 6×10^{-3}mbar. The sputtering power is kept at 125W during the growth of the films. In addition, substrates were cleaned with distilled water to remove any possible impurity, which were placed in ethanol and acetone in the ultrasonic cleaner for 10min. The thickness of CZO and CAZO thin films was about 230±5nm. The values obtained from EDAX analyses (an analytical technique used for the elemental analysis or chemical characterization of a sample) for the ratio of these three metals were 90 to 5% by the weight of zinc to copper and aluminum, respectively. Films were annealed in a furnace by argon flux at three temperatures of 400, 500, and 600°C for 1 hour to consider the effects of annealing on the different properties of thin films. AFM system in the contact mode was used for the study of film surfaces. AFM analysis 2-D surface texture provided a deeper insight into their characteristics and implementation in graphical models and computer simulation. Studying surface roughness of samples at the nanometer scale revealed a fractal structure, which confirmed the relationship between the value of the fractal dimensions and surface roughness parameters. The profile meter was employed to measure the thicknesses of films after deposition processes. The optical spectroscopy properties of films were measured by spectrophotometer in the wavelength range of 200–2500nm. The EDAX system was used to study the content of films.

3. RESULTS AND DISCUSSION

The optical density (D_{opt}) of CZO and CAZO thin films can be obtained from the following equation [39, 40]:

$$D_{opt} = \alpha t \quad (1)$$

Where t is the thickness of the thin films.
The absorption coefficient α of films were obtained from Lambert's relation

$$\alpha = 2.303\ A / t \quad (2)$$

where A is the absorbance of the films.
Fig. 1 (a) and (b) show the electrical density of as-deposited films and films that are annealed at different temperatures 400, 500, and 600ºCfor CZO and CAZO films. The optical density for the CZO thin films is constant between 1 and 3eV, which increase with a steep gradient after 3eV. The optical density for the CZO thin films is constant between 1 and 4eV, which increase with a steep gradient after 4eV. The over 3eV, the optical density of CZO thin films annealed at 500°C have a maximum value. However, the over 4eV, the optical density of as-deposited CAZO thin films have a maximum value. In this work, the thickness is fixed. The size of nanoparticle smoothly increases with increasing annealing temperature up to 400°C. However, the size of nanoparticle has significant changes in the photon energy from 400 to 600°C, and miss an index of optical absorption characterization process, which is theoretically 2 and ½ for the allowed indirect and direct transitions, respectively [10].

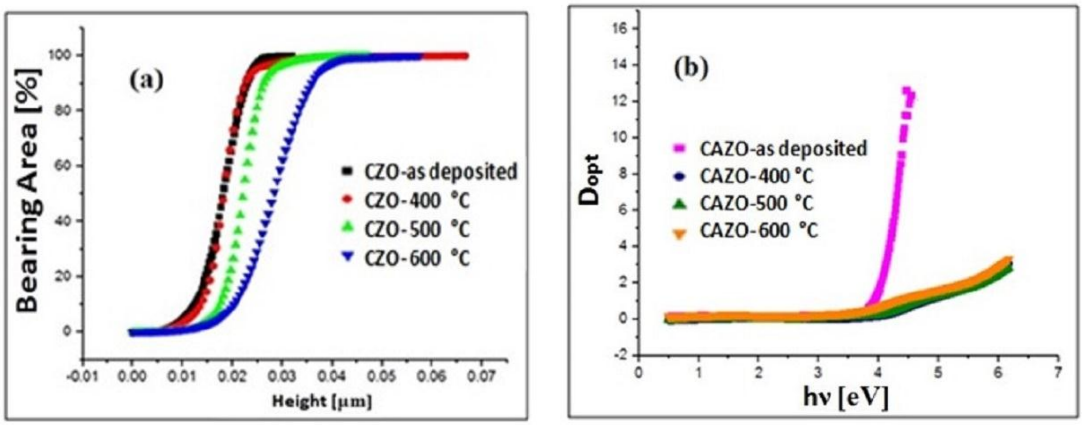

Figure 1. Optical density of as-deposited films and films annealed at 400, 500, and 600°C, (a) CZO and (b) CAZO films

Fig. 2 (a)-(h) show AFM (atomic force microscopy) images of the thin films on the surface of the as-deposited films and films that are annealed at different temperatures 400, 500, and 600°C for CZO and CAZO thin films. Atomic force microscopes (AFM) are a group of scanning probe microscopes that can take biological and non-inductive films in addition to being able to be imaged in a non-vacuum environment. The lateral size of the thin films can be estimated using AFM images. These values for the as-deposited films and films that are annealed at different temperatures400, 500, and 600°C were about 7.9, 8.1, 6.5, and 7.75nm for CZO thin films, respectively. Moreover, the lateral size for CAZO thin films was about 6.8, 6.27, 6.04, and 6.71, respectively. The CZO thin films annealed at 400°C have maximum the amount of nanoparticles lateral size, however the as-deposited CAZO thin films have maximum the amount of nanoparticles lateral size. The AFM images of the CZO films show that nanoparticles are almost spherical and become more amorphous with increasing temperature. However, the CAZO nanoparticles are initially amorphous, spherical, and smaller than the CZO nanoparticles.

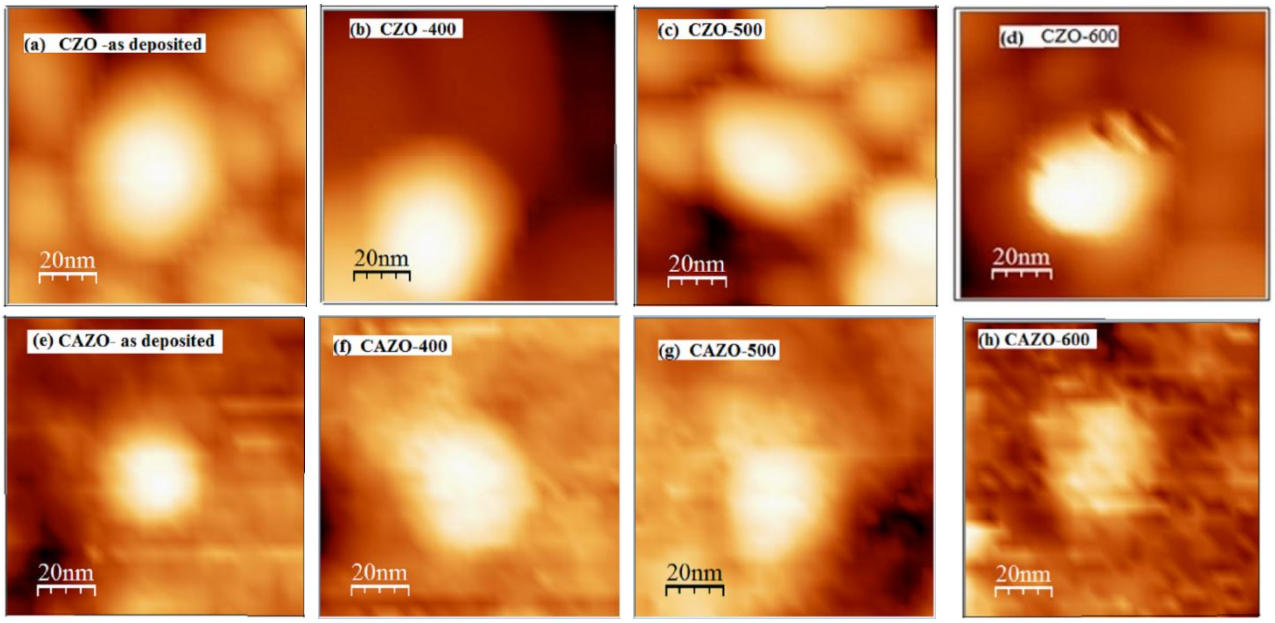

Figure 2. AFM images of nanoparticles on the surface of the CZO and CZAO films for (a,e) the as-deposited films and films that are annealed at different temperatures of (b, f) 400°C, (c, g) 500°C, and (d, h) 600°C

The variation of lateral sizes of film surfaces versus annealing temperature was shown in Fig. 3. It was found that the size of nanoparticles CAZO decreases with the increase in annealing temperature to 500°C, and then, decreases from as-deposited to 500°C. In this way, the CAZO films annealed at 500°C and the CZO at 500°C films have a maximum value of nanoparticles. It can also be seen that the variation of the lateral size of the CZO and CAZO nanoparticles have a slight slope changes. The nanoparticles size changes as Gaussian plots, which can almost be due to little changes in the size of the nanoparticles with the change in temperature. Fig. 4 (a)-(h) show the variation in the height of the thin films on the surface versus the x and z axes for the deposited films and films that are annealed at different temperatures of 400, 500, and 600°C, respectively. The scanning size on the surface of the films was as much as1×1μm by the AFM, the maximum scale value on the x-axis was as much as1μm. The height changes on the

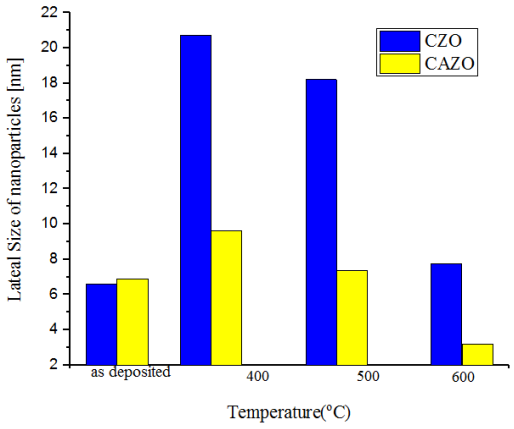

Figure 3. The variations of lateral size of nanoparticles on the surface of the CZO and CZAO thin films for the as-deposited films and films that are annealed at different temperatures of 400, 500, and 600°C

surface of the scanned films show that the films have a topological phase change at 500 and 600°C for CZO thin films and at 600 and 400°C for CAZO thin films. In the deposited films, the *z* values were about 30 and 50nm for the CZO thin films and 9 and 20 nm for CAZO thin films. These results show that the films are smooth in this state, which can have a second phase change. The CAZO nanoparticles have lower fluctuations at room temperature, and the peaks have a slower slope than other temperatures, which have a steep leap above 20nm at 500°C. Also, the CZO nanoparticles at 600°C has lower fluctuations than other temperatures. The *z* ratio of *x* is closely related to both materials, which has many peaks.

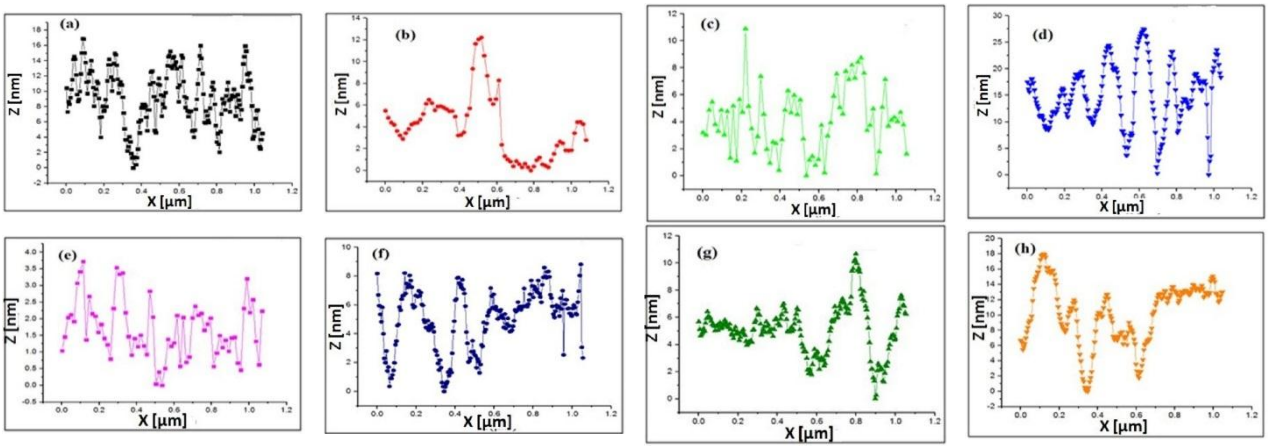

Figure 4. Z-height variations of nanoparticles on the surface of films versus x-axis of the CZO and CZAO thin films for (a,e) the as-deposited films and films that are annealed at different temperatures of (b,f) 400, (c,g) 500, (d,h) 600°C

The PSD spectra were extracted from the scanned area and 1μ×1μ obtained from AFM images of the films as shown in Fig. 2. It can be seen that all the PSD points include a high spatial frequency region. According to the Dynamic Scaling Theory (DST), the power spectral densities (PSDs) analyses closely show how the roughness varies with length scale. The AFM images can be divided into pixels as a small square area where the vectors $h(x_i)$ and $h(y_j)$ are the height at (x_i, y_j) positions. Then, the one-dimensional average of the power spectral densities (PSDs) is given as follows:

$$P(n) = \frac{2L}{N}\left[< \sum_{i=1}^{\frac{N}{2}} (FFT\ (h\ (x_i))^2 >_y + < \sum_{j=1}^{\frac{N}{2}} \left(FFT\ (h\ (y_j)\right)^2 >_x\right] \quad (3)$$

where FFT is the Fast Fourier Transform between the real and reciprocal spaces.

According to the dynamical scaling theory, the relation *P (k)* and frequency *k* are given below for a system with lateral size L [41]

$$\text{P (k)} \propto k^{-\beta} \quad (4)$$

Where β is calculated from the slope of the log-log in PSD spectra of high spatial frequency. The fractal dimensions D_f of films are obtained by solving the β slope of the log-log graph [41]

$$D_f = 4 + {}^{\beta}/_{2} \quad (5)$$

Fig. 5 (a) and 5(b) show the graphs of the spectral density change of the spatial frequency for as-deposited films and films that are annealed at different temperatures of 400, 500, and 600°C. The spectral compaction power of all films reflects the inverse current power variations, especially in the high spatial frequency region, indicating the attendance of fractal components in outstanding topographies. These values determine the relative amounts of surface disorder at different distance scales.

As the annealing temperature increases, the performance of the spectral compaction power increases, which can be due to the decrease in the size of the nanoparticles and have a maximum value at 600°C for CZO films and at 500°C for the CAZO thin films. The values of the fractal dimensions of the films annealed at different annealing temperatures are shown in Fig. 6 that clearly indicates the values of the fractal dimensions depend on the annealing temperature.

The values of the fractal dimensions of the as-deposited CZO thin films and the CZO thin films annealed at 400, 500, and 600°Cwere estimated as much as2.05, 2.07, 2.31, and 2.04, respectively. The values of the fractal dimensions of as-deposited and the CAZO thin films annealed at 400, 500, and 600°C also were estimated as much as2.64, 2.8, 2.9, and 2.7, respectively. Therefore, the fractal dimensions of films increase with the increase of the annealing temperature up to 500°C, and then, decrease over 500°C.

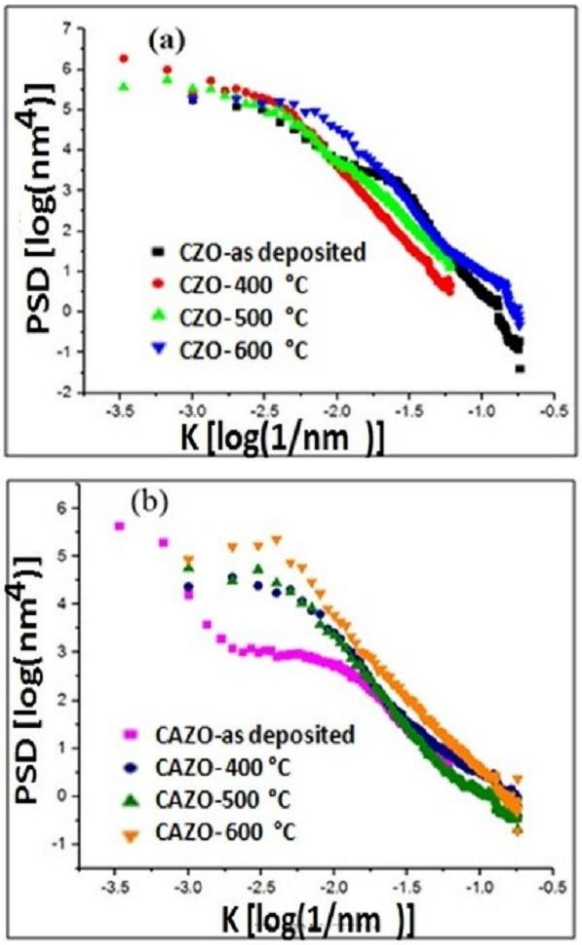

Figure 5. The variations of power spectral density of the films versus frequency k of as-deposited films and annealed films at different temperatures of 400, 500, and 600°C for (a) the CZO thin films and (b) the CAZO thin films

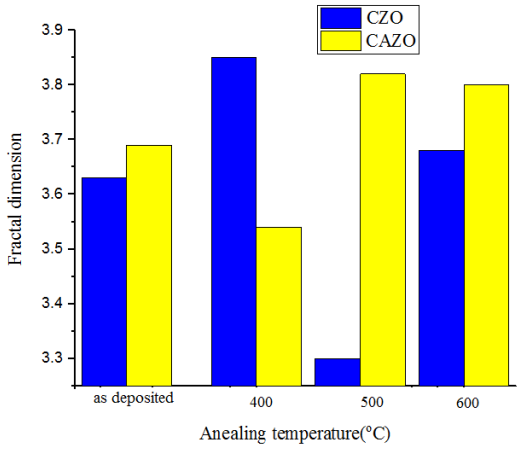

Figure 6. The variationsof fractal dimensions of the CZO thin films and the CAZO thin films annealed at different temperatures of 400, 500, and 600°C

Fig. 7 (a) and (b) show the variations of bearing area of as-deposited CZO and CAZO thin films and CZO and CAZO thin films annealed at400, 500, and 600°C. The CZO thin films in all temperatures have a cavity coverage of less than 10% and layer content of about 95% and 85%, respectively, which are monolayer height. In the vacuum case, the coating is zero, and the content of the films is about 95%, 90% of which is isolated. Furthermore, the cavity coverage is less than 5% for the CAZO thin films as-deposited at room temperature, and the layer content is around 100%, 90% of which is from the height of monolayer. In addition, the monolayer content is over 100% for other temperatures. In the vacuum case, the coating is zero, and the film content is about 100%, 99% of which is isolated.

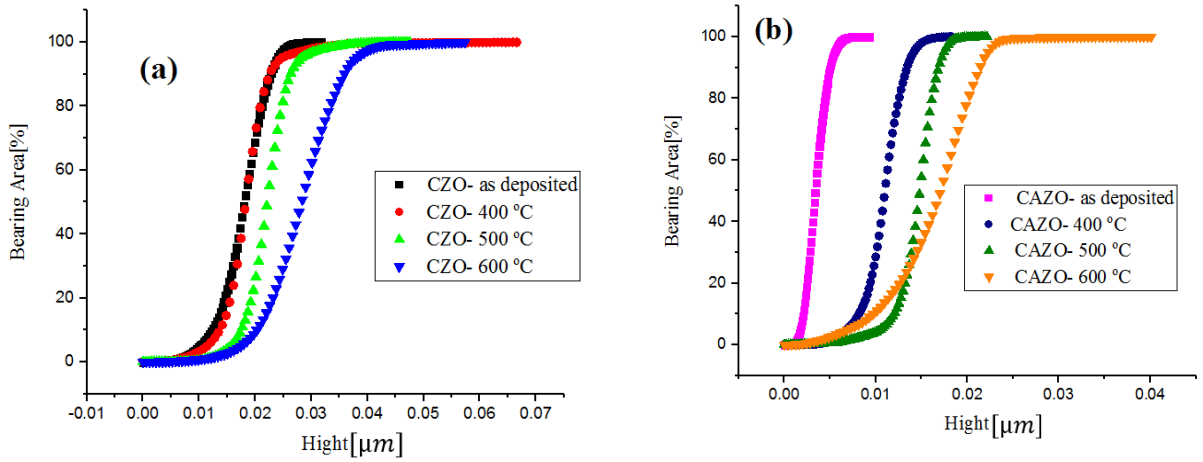

Figure 7. The bearing area of as-deposited films and films that are annealed at different temperatures of 400, 500, and 600°C for (a) CZO films, and (b) CAZO films

4. CONCLUSION

The results suggested that CZO films annealed at 400°C had a maximum lateral size 8.1 nm, and CAZO films annealed at as-deposited had a maximum lateral size as much as 6.8 nm. The CZO and CAZO nanoparticles were almost spherical and became more amorphous with increasing temperature. CZO films showed that nanoparticles were almost spherical and became more amorphous with increasing temperature. However, the CAZO nanoparticles were initially amorphous, spherical, and smaller than the CZO nanoparticles. The CZO and CAZO films had a cavity coverage of less than 10% and 5%, respectively. The optical density had a maximum value both in CZO annealed at 500°C and as-deposited CAZO films. The values of the fractal dimensions of the as-deposited CZO thin films and the CZO thin films annealed at 400, 500, and 600°C were estimated as much as 2.05, 2.07, 2.31, and 2.04, respectively. The values of the fractal dimensions of the as-deposited CAZO thin films annealed at 400, 500, and 600°C also were estimated as much as 2.64, 2.8, 2.9, and 2.7, respectively. It can be seen that the bearing areas of the CZO and CAZO films 600°C had maximum vales and each of them had an increasing function with height.

5. ACKNOWLEDGMENTS

The authors would like to acknowledge the financial support of Malayer University for this research.

REFERENCES

1. Ţălu, Ş., "Micro and nanoscale characterization of three dimensional surfaces: Basics and applications", Napoca Star Publishing House, Cluj-Napoca, Romania, (2015), 350.
2. Dejam, L., Solaymani, S., Achour, A., Stach, S., Ţălu, Ş., Nezafat, N. B., Dalouji, V., Shokri, A. A., Ghaderi, A., "Correlation between surface topography, optical band gaps and crystalline properties of engineered AZO and CAZO thin films", ***Chemical Physics Letters***, Vol. 719, (2019), 78-90.
3. Sobola, D., Ţălu, Ş., Solaymani, S., Grmela, L., "Influence of scanning rate on quality of AFM image: Study of surface statistical metrics", ***Microscopy Research and Technique***, Vol. 80, No. 12, (2017), 1328-1336.
4. Ţălu, Ş., Bramowicz, M., Kulesza, S., Dalouji, V., Solaymani, S., Valedbagi, S., "Fractal features of carbon–nickel composite thin films", ***Microscopy Research & Technique***, Vol. 79, No. 12, (2016), 1208-1213.
5. Stach, S., Sapota, W., Ţălu, Ş., Ahmadpourian, A., Luna, C., Ghobadi, N., Arman, A., Ganji, M., "3-D Surface stereometry studies of sputtered TiN thin films obtained at different substrate temperatures", ***Journal of Materials Science: Materials in Electronics***, Vol. 28, No. 2, (2017), 2113-2122.
6. Zare, M., Solaymani, S., Shafiekhani, A., Kulesza, S., Ţălu, Ş., Bramowicz, M., "Evolution of rough-surface geometry and crystalline structures of aligned TiO_2 nanotubes for photoelectrochemical water splitting", ***Scientific Reports***, Vol. 8, No. 1, (2018), 1-11.
7. Hoseinzadeh, T., Solaymani, S., Kulesza, S., Achour, A., Ghorannevis, Z., Ţălu, Ş., Bramowicz, M., Ghoranneviss, M., Rezaee, S., Boochani, A., Maozaffari, N., "Microstructure, fractal geometry and dye-sensitized solar cells performance of CdS/TiO_2 nanostructures", ***Journal of Electroanalytical Chemistry***, Vol. 830-831, (2018), 80-87.
8. Solaymani, S., Kulesza, S., Ţălu, Ş., Bramowicz, M., Nezafat, N. B., Dalouji, V., Rezaee, S., Karami, H., Malekzadeh, M., Dorbidi, E. S., "The effect of different laser irradiation on rugometric and microtopographic features in zirconia ceramics: Study of surface statistical metrics", ***Journal of Alloys and Compounds***, Vol. 765, (2018), 180-185.
9. Naseri, N., Ţălu, Ş., Kulesza, S., Qarechalloo, S., Achour, A., Bramowicz, M., Ghaderi, A., Solaymani, S., "How morphological surface parameters are correlated with electrocatalytic performance of cobalt-based nanostructures", ***Journal of Industrial and Engineering Chemistry***, Vol. 57, (2018), 97-103.
10. Dejam, L., Solaymani, S., Achour, A., Stach, A., Ţălu, Ş., Nezafat, N. B., Dalouji, V., Shokri, A. A., Ghaderi, A., "Correlation between surface topography, optical band gaps and crystalline properties of engineered AZO and CAZO thin films", ***Chemical Physics Letters***, Vol. 719, (2019), 78-90.
11. Wang, Y., Liu, F., Ji, Y., Yang, M., Liu, W., Wang, W., Sun, Q., Zhang, Z., Zhao, X., Liu, X., "Controllable synthesis of various kinds of copper sulfides (CuS, Cu_7S_4, Cu_9S_5) for high-performance super capacitors", ***Dalton Transactions***, Vol. 44, No. 22, (2015), 10431-10437.
12. Sobola, D., Ţălu, Ş., Solaymani, S., Grmela, L., "Influence of scanning rate on quality of AFM image: Study of surface statistical metrics", ***Microscopy Research and Technique***, Vol. 80, No. 12, (2017), 1328-1336.
13. Dalouji, V., Solaymani, S., Rezaee, S., Mehrparvar**,** D., "Nonmetal—Metal transition in carbon films embedded by Ni nanoparticles: The temperature coefficient of resistivity (TCR), Raman spectra and surface morphology", ***Optik*** ,Vol. 156, (2018), 338-345.
14. Matsumura, M., Camata, R. P., "Pulsed Laser Deposition and Photoluminescence Measurements of ZnO Thin Films on Flexible Polyimide Substrates", ***Thin Solid Films***, Vol. 476, No. 2, (2005), 317-321.
15. Chaabouni, F., Costa, L. C., Abaab, M., Monteiro, J., "Characterization of n-Type: ZnO: Al Films Grown by Magnetron Sputtering", In ***Materials Science Forum*** (Vol. 514-516, 1358-1362), Trans Tech Publications Ltd, Zurich-Uetikon, Switzerland, (2006).
16. Minami, T., Nishi, Y., Miyata, T., "Effect of the thin Ga_2O_3 layer in n^+-ZnO/n-Ga_2O_3/p-Cu_2O heterojunction solar cells"**,** ***Thin Solid Films***, Vol. 549, (2013), 65–69.
17. Casadei, A., Pecora, E. F., Trevino, J., Forestiere, C., Ruffer, D., Russo-Averchi, E., Matteini, F., Tutuncuoglu, G., Heiss, M., Fontcuberta i Morral, A., Dal Negro, L., "Photonic-plasmonic coupling of GaAs single nanowires to optical nano antennas", ***Nano Letters***, Vol. 14, No. 5, (2014), 2271–2278.
18. Kim, T. W., Ha, H. W, Paek, M. J., Hyun, S. H., Choy, J. H., Hwang, S. J., "Unique phase transformation behavior and visible light photocatalytic activity of titanium oxide hybridized with copper oxide", ***Journal of Materials Chemistry***, Vol. 20, No.16, (2010), 3238–3245.
19. Olsen, L. C., Bohara, R. C., Urie, M. W., "Explanation for low-efficiency Cu_2O Schottky-barrier solar cells", ***Applied Physics Letters***, Vol. 34, No. 1, (1979), 47–49.
20. Nakanishi, Y., Miyake, A., Kominami, H., Aoki, T., Hatanaka, Y., Shimaoka, G., "Preparation of ZnO thin films for high-resolution field emission display by electron beam evaporation", ***Applied Surface Science***, Vol. 142, No. 1-4, (1999), 233-236.
21. Ganesh, V., Salem, G. F., Yahia, I. S., Yakuphanoglu, F., "Synthesis, Optical and Photoluminescence Properties of Cu-

Doped Zno Nano-Fibers Thin Films: Nonlinear Optics", ***Journal of Electronic Materials***, Vol. 47, No. 3, (2018), 1798-1805.

22. Zheng, J. H., Song, J. L., Li, X. J., Jiang, Q., Lian, J. S., "Experimental and first-principle investigation of Cu-doped ZnO ferromagnetic powders", ***Crystal Research and Technology***, Vol. 46, No. 11, (2011), 1143-1148.
23. Jin, M., Feng, J., De-Heng, Z., Hong-lei, M., Shu-Ying, L., "Optical and electronic properties of transparent conducting ZnO and ZnO: Al films prepared by evaporating method", ***Thin Solid Films***, Vol. 357, No. 2, (1999), 98-101.
24. Lee, J. H., Chou, C. Y., Bi, Z., Tsai, C. F., Wang, H., "Growth-controlled surface roughness in Al-doped ZnO as transparent conducting oxide", ***Nanotechnology***, Vol. 20, No. 39, (2009), 395704.
25. Zang, Z., Wen, M., Chen, W., Zeng, Y., Zu, Z., Zeng, X., Tang, X., "Strong yellow emission of ZnO hollow nano spheres fabricated using polystyrene spheres as templates", ***Materials & Design***, Vol. 84, (2015), 418–421.
26. Jimenez-Gonzalez, A. E., Urueta J. A. S., Suarez-Parra, R., "Optical and electrical characteristics of aluminum-doped ZnO thin films prepared by sol gel technique", ***Journal of Crystal Growth***, Vol. 192, No. 3-4, (1998), 430-438.
27. Tang, W. Cameron, D. C., "Aluminum-doped zinc oxide transparent conductors deposited by the sol-gel process", ***Thin Solid Films***, Vol. 238, No. 1, (1994), 83-87.
28. Vigil, O., Cruz, F., Santana, G., Vaillant, L., Morales-Acevedo, A., Contreras-Puente, G., "Influence of post-thermal annealing on the properties of sprayed cadmium–zinc oxide thin films", ***Applied Surface Science***, Vol.161, No. 1-2, (2000), 27-34.
29. Nunes, P., Malik, A., Fernandes, B., Fortunato, E., Vilarinho, P., Martins, R., "Influence of the doping and annealing atmosphere on zinc oxide thin films deposited by spray pyrolysis", ***Vacuum***, Vol. 52, No. 1-2, (1999), 45-49.
30. Nunes, P., Fortunato, E., Martins, R., "Influence of the post-treatment on the properties of ZnO thin films", ***Thin Solid Films***, Vol. 383, No. 1-2, (2001), 277-280.
31. Jin, B. J., Woo, H. S., Im, S., Bae, S. H., Lee, S. Y., "Relationship between photoluminescence and electrical properties of ZnO thin films grown by pulsed laser deposition", ***Applied Surface Science***, Vol.169–170, (2001), 521-524.
32. Meng, X. Q., Zhen, W., Guo, J. P., Fan, X. J., "Structural, optical and electrical properties of ZnO and ZnO-Al2O3 films prepared by dc magnetron sputtering", ***Applied Physics A***, Vol. 70, No. 4, (2000), 421–424.
33. Minemoto, T., Negami, T., Nishiwaki, S., Takakura, H., Hamakawa, Y., "Preparation of $Zn_{1-x}Mg_xO$ films by radio frequency magnetron sputtering", ***Thin Solid Films***, Vol. 372, No. 1-2, (2000), 173-176.
34. Minami, T., Sonohara, H., Kakumu, T., Takata, S., "Highly Transparent and Conductive $Zn_2In_2O_5$ Thin Films Prepared by RF Magnetron Sputtering", ***Japanese Journal of Applied Physics***, Vol. 34, No. 8A, (1995), L971.
35. Minami, T., Yamamoto, T., Miyata, T., "Highly transparent and conductive rare earth-doped ZnO thin films prepared by magnetron sputtering", ***Thin Solid Films***, Vol. 366, No. 1-2, (2000), 63-68.
36. Tominaga, K., Kataoka, M., Manabe, H., Ueda, T., Mori, I., "Transparent ZnO: Al films prepared by co-sputtering of ZnO: Al with either a Zn or an Al target", ***Thin Solid Films***, Vol. 290–291, (1996), 84-87.
37. Serin, T., Atilgan, A., Kara, I., Yildiz, A., "Electron transport in Al-Cu co-doped ZnO thin films", ***Journal of Applied Physics***, Vol. 121, No. 9, (2017), 095303.
38. Dalouji, V., "Power spectral densities and polaron hopping conduction parameters in carbon films embedded by nickel nanoparticles", ***Optik***, Vol. 148, (2017), 1-7.
39. Hassanien, A. S., Akl, A. A., "Effect of Se addition on optical and electrical properties of chalcogenide CdSSe thin films", ***Superlattices and Microstructures***, Vol. 89, (2016), 153-169.
40. Van Zeghbroeck, B., "Principles of Electronic Devices", Boulder, University of Colorado, (1997).
41. Raoufi, D., "Fractal analyses of ITO thin films: A study based on power spectral density", ***Physica B: Condensed Matter***, Vol. 405, No. 1, (2010), 451-455.

ACERP: Vol. 6, No.2, (Spring 2020) 24-29

Advanced Ceramics Progress

Research Article

Journal Homepage: www.acerp.ir

Dielectric and Mechanical Properties of BZT-xBCT Piezoceramics Modified by Nano SiO_2 Additive

R. Hayati [a]*, M. A. Razavian [a]

[a] *Department of Materials Engineering, Yasouj University, Yasouj, 75918-74934, Iran*

PAPER INFO

Paper history:

Received 27 May 2020
Accepted in revised form 14 June 2020

Keywords:

Piezoceramic
$(Ba_{0.85}Ca_{0.15})(Ti_{0.9}Zr_{0.1})O_3$
NanoSiO_2; Dielectric
Mechanical Property

ABSTRACT

Lead-free $(Ba_{0.85}Ca_{0.15})(Ti_{0.9}Zr_{0.1})O_3$ piezoceramics with nano SiO_2 additive were prepared by conventional solid oxide sintering method. The samples were fabricated by means of cold isostatic pressing and sintering was performed at 1350 °C for 4 h in the air. The phase structure and microstructure were studied via X-ray diffraction technique and field emission scanning electron microscopy. The room-temperature dielectric properties and the variations in the temperature ranging from 23 to 160 °C were measured using a high-precision LCR meter. The mechanical properties such as Vickers hardness and compressive strength were investigated. The obtained results showed that nano SiO_2 addition produced dense and uniform microstructures with larger grains than pure BCZT. The Curie temperature of undoped BCZT increased to about 25 °C through the incorporation of 0.75 mol% SiO_2 and then, the mechanical properties considerably improved. Accordingly, BCZT piezoceramic with nano SiO_2 additive enjoys viable properties, which makes it widely applicable.

1. INTRODUCTION

Due to the ability of piezoelectric materials to exchange electrical energy for mechanical energy, they are widely used in a variety of applications such as sensors, actuators, and energy harvesters [1]. Although PZT and other Pb-based piezoceramics are the most widely used materials, human health and environmental concerns have compelled the piezoelectric society to look for safe and lead-free materials such as $K_{0.5}Na_{0.5}NbO_3$ (KNN), $(Na_{1/2}Bi_{1/2})TiO_3$ (NBT), and $(Ba_{1-x}Ca_x)(Ti_{1-x}Zr_x)O_3$ (BCZT) [2, 3].

The pseudo-binary solid solution of $Ba(Zr_{0.2}Ti_{0.8})O_3$-x $(Ba_{0.7}Ca_{0.3})TiO_3$, referred to as BZT-xBCT, was introduced by Liu and Ren [4]. Our studies have shown that BCZT is a competitive alternative to PZT and because of its superior piezoelectric coefficients (d_{33}≈620 pC/N for x=0.5) [4] large blocking force values [5] and high cycling stability [6] this material is regarded as a good candidate for actuator applications [7]. However, some limitations such as high processing temperatures [8] and low Curie temperature limits its applications [9]. Despite its outstanding piezoelectric properties, BCZT is constrained by some limitations including high processing temperatures [8] and low T_C, which puts limits on its working temperature [9]. Therefore, in recent years, attempts have been made to reduce the processing temperature and increase the Curie point of BCZT by doping or using different additives.

The critical parameter that affects the functionality of piezoelectric devices is the mechanical behavior of the material. The feasibility of crack propagation near porosities, grain boundaries, and domain walls marks the importance of hardness, strength, and toughness of materials for piezoelectric applications [10]. For instance, during the actuating process, the periodic domain switching in ferroelectric materials and their corresponding non-elastic strain results in growth of crack and mechanical malfunctioning of the device [11]. Various studies have investigated the mechanical properties of PZT and non-Pb piezoelectric ceramics; however, only few of them have reported the mechanical properties of lead-free BCZT piezoceramics.

The Vickers hardness of pure and doped PZT ceramics ranges from 2.5 to 4 GPa [12-14]. For KNN-based piezoceramics, the corresponding values attributed to hardness and compressive strength are 2.2-5 GPa and 36-126 MPa, respectively [15]. Regarding the BCZT

* Corresponding Author Email: r.hayati@yu.ac.ir (R. Hayati)

https://doi.org/10.30501/acp.2020.109545

piezoceramics, Srivinas et al. (2015) investigated the mechanical behavior of $Ba(Zr_{0.2}Ti_{0.8})O_3$-0.5 $(Ba_{0.7}Ca_{0.3})O_3$ ceramics in terms of Vickers hardness, modulus, and fracture toughness and reported higher values than those of PZT [16]. In another study, Coondoo et al., compared Young's modulus and hardness of sol-gel synthesized BZT-50BCT (SG-BCZT) with the corresponding parameters of conventionally-sintered BCZT ceramics (CS-BCZT). They concluded that the sol-gel method produced BZT-50BCT ceramics with smaller grains and higher mechanical properties, as decreasing the grain size form 27 µm in CS-BCZT to 1.5 µm in SG-BCZT resulted in the increment of Young's modulus from 117.9 to 158.3 GPa [17]. As a result there should be a clear relation between the processing technique, the microstructure and the functional properties of pizoceramics, as is declared in the literature [18-20].

In order to improve the mechanical behavior of piezoceramics, some additives such as AlN [21], Si_3N_4 [22], Al_2O_3 [23], and SiO_2 [24] were applied. Adhikari et al. [25] studied the effects of nano Al_2O_3 addition on mechanical properties of BZT-50BCT piezoceramics and concluded that adding 1 Vol.% alumina increased the flexural strength and hardness to 92 and 741.5 MPa, respectively.

Given the constructive effect of nano particles on electrical and mechanical properties of piezoceramics [25, 26], the present study examines the effects of nano SiO_2 addition on dielectric and mechanical properties of BZT-50BCT ceramics. Based on the authors' knowledge, the effect of nano SiO_2 additive on dielectric and mechanical properties of BZT-50BCT is not reported in the literature. We expect that nano SiO_2 additive facilitates the sintering process and improves the mechanical properties of BCZT piezoceramics at a low sintering temperature, without the deterioration of the dielectric properties.

2. EXPERIMENTAL

Lead-free $(Ba_{1-x}Ca_x)(Ti_{1-x}Zr_x)O_3$ (BCZT) piezoceramics were fabricated via conventional solid oxide sintering route. The raw materials of $BaCO_3$ (99.5%), $CaCO_3$ (99.5%), TiO_2 (99.5%), and ZrO_2 (99.5%) (all purchased from Merck Co., Darmstadt, Germany) were mixed according to the stoichiometric formula and ground for 5 h at 200 rpm in ethanol using a planetary mill with zirconia balls. The calcination process was carried out at 1300 °C for 4 hours at a heating rate of 3°C/min. Different amounts of nano SiO_2 were mixed with the BCZT powder at the second milling step at a milling time interval of 2 h at 250 rpm and the compositions were called BCZT-xSi: x values of 0, 0.25, 0.5, 0.75, and 1 mol%. The slurries were then oven-dried at 90 °C for 24 h. The powders were shaped by hand into disks with diameters of 10 mm and thickness of 1.5-2 mm and, subsequently, pressed via cold isostatic pressing (CIP, K303, Iran) at 250 MPa. The sintering was performed in zirconia crucibles at 1350 °C (heating rate of 5 °C/min) for 4 h.

The density of samples was measured using Archimedes method. The phase structure was studied by means of X-ray diffraction technique (XRD: Philips Co., Model PW1730, Netherlands) with Cu kα radiation and the microstructure of the polished and thermal-etched samples was investigated using a field-emission scanning electron microscope (FE-SEM; Model MIRA3 XMU, TESCAN, Czech Republic). Based on the FE-SEM images, the average grain size of at least 200 grains was determined by the mean intercept length method via Lince software.

The dielectric properties were measured by a high-precision LCR meter at a frequency of 1 KHz (GW Instek Co., model LCR-6020), and the Curie temperature was measured in the temperature range of RT-160 °C by the same LCR meter equipped with a heating system.

As mentioned in a previous study [9], the stress-strain curves of cylindrical samples were employed to measure the compressive strength using a DMG Universal testing machine (Model 7166, United Kingdom) at a speed of 0.5 mm/min. Disk shaped samples were used for the Vickers hardness test (MHV1000Z) and the test was performed with a load of 200 g at a dwell time of 20 seconds.

3. RESULTS AND DISCUSSION

Fig. 1 shows the XRD patterns of BCZT-xSi ceramics with different SiO_2 content. As observed, all the samples possess a single perovskite phase with no impurity or second phases. This demonstrates that the amount of probable silica-based phases is less than the detection limit of the XRD technique (2-4 wt%).

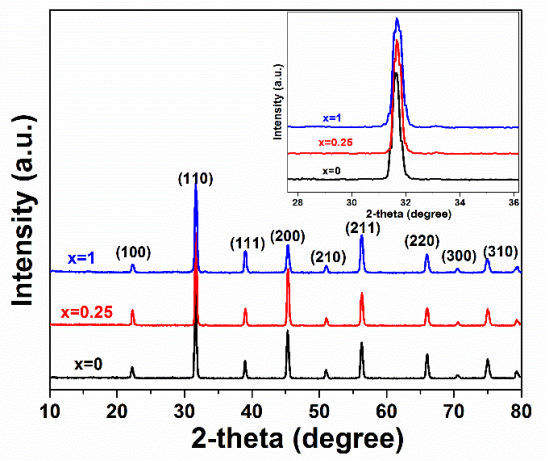

Figure 1. The XRD patterns of BCZT-xSi ceramics sintered at 1350 °C for 4h, the inset shows the expanded peaks at 2θ=32°

The extended peaks at 2θ≈32° are shown in the inset of Fig. 1. As observed, the peaks are slightly shifted to higher 2θ angles, indicating that incorporation of SiO_2 to BCZT lattice contracted the structure due to the smaller ionic radius of Si^{4+} (0.4 Å) than those of Zr^{4+} (0.7 Å) and Ti^{4+} (0.605 Å) in the B-site of the BCZT perovskite lattice. The splitting of peaks at 2θ=45° and the overlapping of the corresponding peaks at these angles confirm the formation of non-cubic phases and the ferroelectric nature of these compositions.

The FE-SEM micrographs of BCZT-xSi samples sintered at 1350 °C are shown in Fig. 2. At this temperature, sintering of BCZT leads to a porous microstructure as evident in Fig 2a.

However, upon addition of nano SiO_2 we can see in Fig. 2b-d that the porosity is reduced with a higher SiO_2 content leading to increased grain size and density (Fig. 3). At 0.75mol%, the average grain size and density are 14 µm and 5.57 g/cm^3 (97.5% relative density, based on the theoretical density of 5.71 for BCZT and 2.65 for SiO_2) respectively. This density value is comparable with previous studies [7,25]. However, higher SiO_2 addition had a negative effect on densification. It must be noted that the sintering temperature of pure, single phase BCZT is about 1450-1550 [4, 27, 28], whereas in this study sintering was performed at 1350 °C. Therefore, it is plausible that the incorporation of a nanoscale powder accelerates the densification process and thus plays the role of a sintering aid [29].

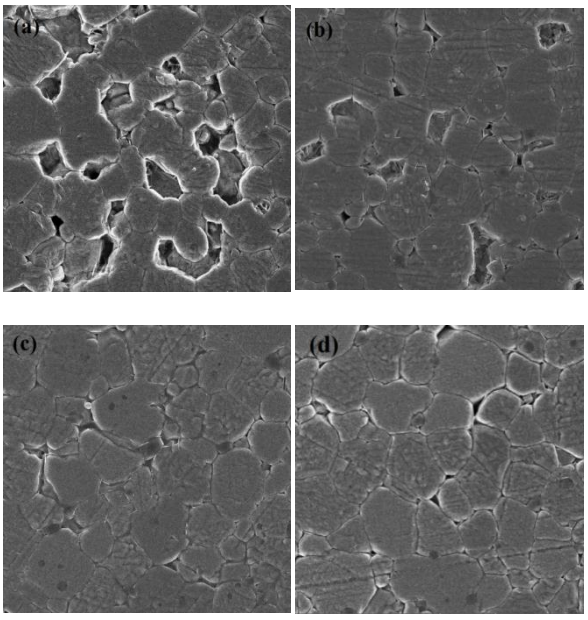

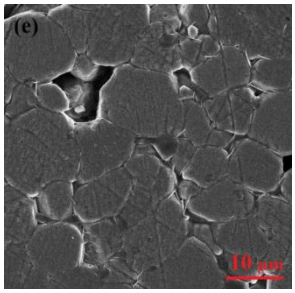

Figure 2. The FE-SEM photographs taken from the polished and thermally-etched surfaces of BCZT-xSi samples sintered at 1350 °C for 4 h (a) x=0, (b) x=0.25, (c) x=0.5, (d) x=0.75, and (e) x=1

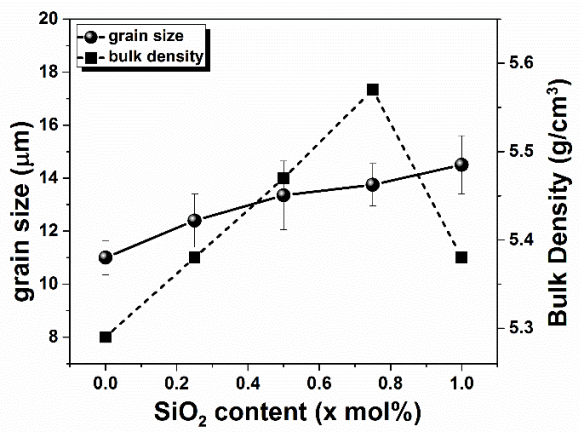

Figure 3. The variations in grain size and bulk density with SiO_2 content for BCZT-xSi samples sintered at 1350 °C for 4 h

The plots of variation of dielectric properties with temperature are presented in Fig. 4. Measurements were carried out at temperatures ranging from 23 to 160 °C and a frequency of 1 kHz. The maximum dielectric constant at T_C is reduced with SiO_2 addition; therefore, the highest value is related to undoped BCZT (ε_{max}=7776). Some fluctuations in the maxima of the curves have been detected, and the highest value of ε_{max} is 7714 for BCZT-0.75Si sample. The Curie temperature shifts to higher temperatures and the maximum T_C of 105 °C belongs to BCZT-1Si sample. Any increase in T_C can be attributed to the lattice distortion after incorporation of Si ions to BCZT lattice. The upward trend of Curie temperature with SiO_2 addition is in agreement with the results obtained by Lee et al. [30] for $Ba_{0.96}Ca_{0.04}Zr_{0.15}Ti_{0.85}O_3$-$xSiO_2$ ceramics; however, the Curie temperatures of the present study are much higher than the corresponding values reported with different BCZT compositions.

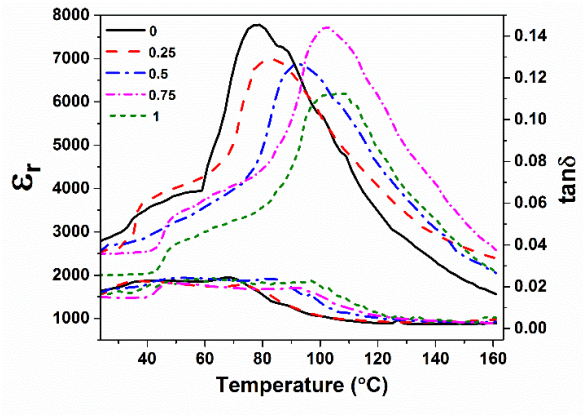

Figure 4. The variations in dielectric properties versus temperature for BCZT-xSi samples measured at a frequency of 1 KHz

The data of room-temperature dielectric constant (ε_r) and dielectric loss (tanδ) are reported in Table 1. Addition of SiO_2 does not improve the dielectric constant; however, due to the higher density, dielectric loss is slightly lower than that of pure BCZT. SiO_2 can form some glassy phases with inferior dielectric constant than that of BCZT; this is the reason why lower ε_r values are obtained by increasing SiO_2 content [30].

TABLE 1. Summary of dielectric properties of BCZT-xSi samples sintered at 1350 °C for 4 h

X	ε_r (1kHz, RT)	tanδ (1kHz, RT)	T_C (°C)
0	2759	0.018	79
0.25	2125	0.016	83
0.5	2515	0.017	93
0.75	2502	0.015	103
1	2003	0.017	105

Fig. 5 shows the compressive stress-strain curves of BCZT-xSi samples and the corresponding compressive strength values are presented in the figure inset. Accordingly, nano SiO_2 addition considerably improves the compressive strength of BCZT, and BCZT-0.75Si experiences the maximum value of 550 MPa at a sintering temperature of 1350 °C. Since the trend of variations in compressive strength is similar to bulk density, it can be concluded that the uniform grains and dense microstructure of this sample are the notable criteria that maximize the strength of this composition. Chen et al. [31] argued that the lower the porosity values were, the higher the compressive strength of the ceramics would be, as can be seen in the following equation:

$$\sigma = \sigma_0 \exp(-k\alpha) \quad (1)$$

where σ_0 is the strength of a perfect lattice, σ the corresponding value in the presence of defects, α the factor presenting the amount of porosities, and k an experimental coefficient. Hayati et al. [9] investigated the mechanical properties of BZT-xBCT piezoceramics and suggested that the highest compressive strength of 950 MPa was obtained for BZT-0.5 BCT. In another study, Yusong et al. [32] reported the maximum compressive strength of 210 MPa for BNT-0.06BT ceramics sintered at 1150 °C for 2 h. According to Tan et al. [15], the compressive strength of $(K_{0.48}Na_{0.52})_{1-x}(Li_{0.15}Na_{0.85})xNb_{0.98}Sb_{0.02}O_3$-$0.03Bi_{0.5}Na_{0.5}ZrO_3$-$0.02CaTiO_3$ piezoceramics ranged from 300 to 790 MPa. Compared with the compressive strength of natural bone [33] and apatite scaffolds [34], the values of these parameters obtained in the present study are much higher.

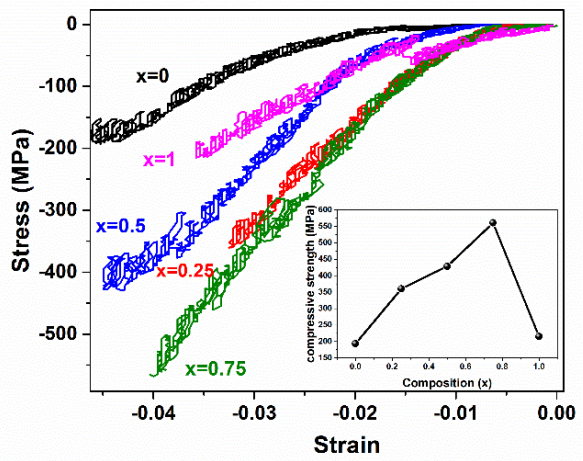

Figure 5. The stress-strain curves of BCZT-xSi samples sintered at 1350 °C for 4 h (the inset shows the plot of the compressive strength versus composition)

The Vickers hardness of BCZT-xSi ceramics with different SiO_2 content is shown in Fig. 6. As observed, nano SiO_2 has tripled the hardness of pure BCZT, experiencing an increase from 2.7 GPa for undoped BCZT to 6.8 GPa for BCZT-0.75 Si. Although this sample is characterized by the highest density, the higher hardness of BCZT-Si ceramics is not necessarily related to the bulk density of this sample, as demonstrated by Arianpour et al. [35] in their study on the mechanical properties of Ultra-High Temperature Tantalum/Hafnium Carbides Composite. Moshtaghioun et al. [36] suggested that the hardness of ceramics followed the Hall-Petch equation, and smaller grains would lead to higher hardness values. However, the higher hardness of BCZT-Si piezoceramics with larger grains than undoped BCZT cannot be justified according to the hall-petch equation. The Vickers hardness of silica ranges from 4.5 to 9.5 GPa, which can be regarded as a hard material. Therefore, incorporation of nano SiO_2 to BCZT ceramics considerably increases the hardness at a low sintering temperature and BCZT-0.75Si with a dense and uniform microstructure is the hardest sample.

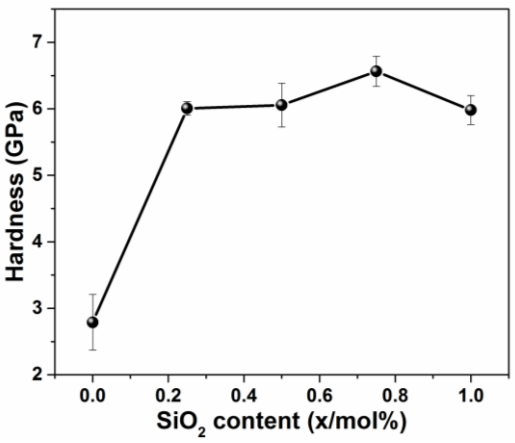

Figure 6. The variations in hardness versus composition of BCZT-xSi samples sintered at 1350 °C for 4 h

4. CONCLUDING REMARKS

In the present study, $(Ba_{0.85}Ca_{0.15})(Ti_{0.9}Zr_{0.1})O_3$ piezoceramics were prepared by solid state synthesis route and, after adding nano SiO_2, the samples were fabricated through normal sintering in the air at 1350 °C. Phase and microstructure analyses were carried out using x-ray diffractometry and scanning electron microscopy. The addition of up to 1 mol% SiO_2 resulted in a single perovskite phase with no secondary phases, and the microstructure studies demonstrated dense and uniform microstructures with relatively larger grains than undoped BCZT. The unchanged room-temperature dielectric constant was accompanied by lower dielectric loss and higher Curie temperature. In addition, the mechanical properties increased severely as the compressive strength and Vickers hardness of the BCZT sample with 0.75 mol% nano SiO_2 reached the values of 550 MPa and 6.8 GPa, respectively. Accordingly, BCZT ceramic with nano SiO_2 additive is a good candidate for piezoelectric devices.

5. ACKNOWLEDGMENTS

The authors would like to acknowledge the financial support of Yasouj University of Iran for this research.

REFERENCES

1. Koruza, J., Bell, A.J., Frömling, T., Webber, K.G., Wang, K., Rödel, J., "Requirements for the transfer of lead-free piezoceramics into application", ***Journal of Materiomics***, Vol. 4, No. 1, (2018), 13-26. DOI:10.1016/j.jmat.2018.02.001
2. Panda, P.K., Sahoo, B., "PZT to lead free piezo ceramics: a review", ***Ferroelectrics***, Vol. 474, No. 1, (2015), 128-143. DOI:10.1080/00150193.2015.997146
3. Wei, H., Wang, H., Xia, Y., Cui, D., Shi, Y., Dong, M., Liu, C., Ding, T., Zhang, J., Ma, Y., Wang, N., "An overview of lead-free piezoelectric materials and devices", ***Journal of Materials Chemistry C***, Vol. 6, No. 46, (2018), 12446-12467. DOI:10.1039/c8tc04515a
4. Liu, W., Ren, X., "Large piezoelectric effect in Pb-free ceramics", ***Physical review letters***, Vol. 103, No. 25, (2009), 257602. DOI:10.1103/physrevlett.103.257602
5. Brandt, D.R., Acosta, M., Koruza, J., Webber, K.G., "Mechanical constitutive behavior and exceptional blocking force of lead-free BZT-x BCT piezoceramics", ***Journal of Applied Physics***, Vol. 115, No. 20, (2014), 204107. DOI:10.1063/1.4879395
6. Zhang, Y., Glaum, J., Ehmke, M.C., Blendell, J.E., Bowman, K.J., Hoffman, M.J., "High bipolar fatigue resistance of BCTZ lead- free piezoelectric ceramics", ***Journal of the American Ceramic Society***, Vol. 99, No. 1, (2016), 174-182. DOI:10.1111/jace.13927
7. Hayati, R., Bahrevar, M.A., Ebadzadeh, T., Rojas, V., Novak, N., Koruza, J., "Effects of Bi2O3 additive on sintering process and dielectric, ferroelectric, and piezoelectric properties of (Ba0. 85Ca0. 15)(Zr0. 1Ti0. 9) O3 lead-free piezoceramics", ***Journal of the European Ceramic Society***, Vol. 36, No. 14, (2016), 3391-3400. DOI:10.1016/j.jeurceramsoc.2016.05.033
8. Hayati, R., Bahrevar, M.A., Ganjkhanlou, Y., Rojas, V., Koruza, J., "Electromechanical properties of Ce-doped (Ba 0.85 Ca 0.15)(Zr 0.1 Ti 0.9) O 3 lead-free piezoceramics", ***Journal of Advanced Ceramics***, Vol. 8, No. 2, (2019), 186-195. DOI:10.1007/s40145-018-0304-2
9. Hayati, R., Fayazi, M., Diargar, H., Kaveh, M., Tayebi, L., "Electrical and mechanical properties of BZT− x BCT lead- free piezoceramics", ***International Journal of Applied Ceramic Technology***, Vol. 17, No. 4, (2020), 1891-1898. DOI:10.1111/ijac.13494
10. Takahashi, H., Nagata, H., Takenaka, T., "Mechanical bending strength of (Bi0. 5Na0. 5) TiO3-based lead-Free piezoelectric ceramics", ***Journal of Asian Ceramic Societies***, Vol. 5, No. 3, (2017), 242-246. DOI:10.1016/j.jascer.2017.03.002
11. Promsawat, M., Watcharapasorn, A., Jiansirisomboon, S., "Effects of ZnO nanoparticulate addition on the properties of PMNT ceramics", ***Nanoscale research letters***, Vol. 7, No. 1, (2012), 1-7. DOI:10.1186/1556-276x-7-65
12. Promsawat, M., Watcharapasorn, A., Sreesattabud, T., Jiansirisomboon, S., "Effect of ZnO nano-particulates on structure and properties of PZT/ZnO ceramics", ***Ferroelectrics***, Vol. 382, No. 1, (2009), 166-172. DOI:10.1080/00150190902870226
13. Nam, H.D., Lee, H.Y., "Electrical and mechanical properties of PZT ceramics", ***Ferroelectrics***, Vol. 186, No. 1, (1996), 309-312. DOI:10.1080/00150199608218090
14. Miyoshi, T., Funakubo, H., "Effect of grain size on mechanical properties of full-dense Pb (Zr, Ti) O3 ceramics", ***Japanese Journal of Applied Physics***, Vol. 49, No. 9S, (2010), 09MD13. DOI:10.1143/jjap.49.09md13
15. Tan, Z., Xie, S., Jiang, L., Xing, J., Chen, Y., Zhu, J., Xiao, D., Wang, Q., "Oxygen octahedron tilting, electrical properties and mechanical behaviors in alkali niobate-based lead-free piezoelectric ceramics", ***Journal of Materiomics***, Vol. 5, No. 3, (2019), 372-384. DOI:10.1016/j.jmat.2019.02.001
16. Srinivas, A., Krishnaiah, R.V., Niranjani, V.L., Kamat, S.V., Karthik, T., Asthana, S., "Ferroelectric, piezoelectric and mechanical properties in lead free (0.5) Ba (Zr0. 2Ti0. 8) O3–(0.5)(Ba0. 7Ca0. 3) TiO3 electroceramics", ***Ceramics International***, Vol. 41, No. 2, (2015), 1980-1985. DOI:10.1016/j.ceramint.2014.08.127
17. Coondoo, I., Panwar, N., Alikin, D., Bdikin, I., Islam, S.S., Turygin, A., Shur, V.Y., Kholkin, A.L., "A comparative study of

structural and electrical properties in lead-free BCZT ceramics: influence of the synthesis method", ***Acta Materialia***, Vol. 155, (2018), 331-342. DOI:10.1016/j.actamat.2018.05.029

18. Hao, J., Bai, W., Li, W., Zhai, J., "Correlation between the microstructure and electrical properties in high- performance (Ba 0.85 Ca 0.15)(Zr 0.1 Ti 0.9) O 3 lead- free piezoelectric ceramics", ***Journal of the American Ceramic Society***, Vol. 95, No. 6, (2012), 1998-2006. DOI:10.1111/j.1551-2916.2012.05146.x
19. Bai, Y., Matousek, A., Tofel, P., Bijalwan, V., Nan, B., Hughes, H., Button, T.W., "(Ba, Ca)(Zr, Ti) O3 lead-free piezoelectric ceramics—the critical role of processing on properties", ***Journal of the European Ceramic Society***, Vol. 35, No. 13, (2015), 3445-3456. DOI:10.1016/j.jeurceramsoc.2015.05.010
20. Mittal, S., Chandramani Singh, K., "Size Effect of Nanoscale Powders on the Polarization of the BCZT Piezoceramic: A Pyroelectric and Fatigue Perspective", ***Integrated Ferroelectrics***, Vol. 205, No. 1, (2020), 122-130. DOI:10.1080/10584587.2019.1675008
21. Xu, D., Wang, L., Li, W., Wang, W., Hou, Y., Cao, W., Feng, Y., Fei, W., "Enhanced piezoelectric and mechanical properties of AlN-modified BaTiO 3 composite ceramics", ***Physical Chemistry Chemical Physics***, Vol. 16, No. 26, (2014), 13078-13085. DOI:10.1039/c4cp00796d
22. Iyer, S., McIntosh, J., Bandyopadhyay, A., Langrana, N., Safari, A., Danforth, S.C., Clancy, R.B., Gasdaska, C., Whalen, P.J., "Microstructural characterization and mechanical properties of Si3N4 formed by fused deposition of ceramics", ***International Journal of Applied Ceramic Technology***, Vol. 5, No. 2, (2008), 127-137. DOI:10.1111/j.1744-7402.2008.02193.x
23. Puchmark, C., Rujijanagul, G., Jiansirisomboon, S., Tunkasiri, T., Vittayakorn, N., Comyn, T., Milne, S.J., "Mechanical property evaluation of PZT/Al2O3 composites prepared by a simple solid-state mixed oxide method", ***Current Applied Physics***, Vol. 6, No. 3, (2006), 323-326. DOI:10.1016/j.cap.2005.11.010
24. Zhu, Z.G., Li, B.S., Li, G.R., Yin, Q.R., "Effects of SiO2 substitution on piezoelectric and mechanical properties of PMS-PZT ternary piezoelectric ceramics", ***In Key Engineering Materials***, Vol. 280, (2005), 215-218. Trans Tech Publications Ltd. DOI:10.4028/www.scientific.net/kem.280-283.215
25. Adhikari, P., Mazumder, R., Sahoo, G.K., "Electrical and mechanical properties of 0.5 Ba (Zr0. 2Ti0. 8) O3–0.5 (Ba0. 7Ca0. 3) TiO3 (BZT–BCT) Lead free ferroelectric ceramics reinforced with nano-sized Al2O3", ***Ferroelectrics***, Vol. 490, No. 1, (2016), 60-69. DOI:10.1080/00150193.2015.1072013
26. Hayati, R., Barzegar, A., "Microstructure and electrical properties of lead free potassium sodium niobate piezoceramics with nano ZnO additive", ***Materials Science and Engineering: B***, Vol. 172, No. 2, (2010), 121-126. DOI:10.1016/j.mseb.2010.04.033
27. Rojas, V., Koruza, J., Patterson, E.A., Acosta, M., Jiang, X., Liu, N., Dietz, C., Rödel, J., "Influence of composition on the unipolar electric fatigue of Ba (Zr0. 2Ti0. 8) O3- (Ba0. 7Ca0. 3) TiO3 lead- free piezoceramics", ***Journal of the American Ceramic Society***, Vol. 100, No. 10, (2017), 4699-4709. DOI:10.1111/jace.15013
28. Buatip, N., Dhanunjaya, M., Amonpattaratkit, P., Pomyai, P., Sonklin, T., Reichmann, K., Janphaung, P., Pojprapai, S., "Comparison of conventional and reactive sintering techniques for Lead–Free BCZT ferroelectric ceramics", ***Radiation Physics and Chemistry***, Vol. 172, (2020), 108770. DOI:10.1016/j.radphyschem.2020.108770
29. Castro, R., Van Benthem, K. eds., "Sintering: mechanisms of convention nanodensification and field assisted processes", ***Springer Science & Business Media***, Vol. 35, (2012). DOI:10.1007/978-3-642-31009-6
30. Lee, Y.C., Lin, C.W., Lu, W.H., Chen, W.J., Lee, W.H., "Influence of SiO2 addition on the dielectric properties and microstructure of (Ba0. 96Ca0. 04)(Ti0. 85Zr0. 15) O3 ceramics", ***International Journal of Applied Ceramic Technology***, Vol. 6, No. 6, (2009), 692-701. DOI:10.1111/j.1744-7402.2009.02379.x
31. Chen, Y., Xie, S., Wang, Q., Fu, L., Nie, R., Zhu, J., "Correlation between microstructural evolutions and electrical/mechanical behaviors in Nb/Ce co-doped Pb (Zr0. 52Ti0. 48) O3 ceramics at different sintering temperatures", ***Materials Research Bulletin***, Vol. 94, (2017), 174-182. DOI:10.1016/j.materresbull.2017.05.045
32. Yusong, P., Qianqian, S., Yan, C., "Fabrication and mechanical properties of Na0. 5Bi0. 5TiO3–BaTiO3 lead-free piezoelectric ceramics", ***Ceramics–Silikáty,*** Vol. 58, No. 1, (2014), 50-55.
33. Havaldar, R., Pilli, S.C., Putti, B.B., "Insights into the effects of tensile and compressive loadings on human femur bone", ***Advanced biomedical research***, Vol. 3, (2014). DOI:10.4103/2277-9175.129375
34. Abdollahi, E., Bakhsheshi-Rad, H., "Evaluation of mechanical properties and apatite formation of synthesized fluorapatite-hardystonite nanocomposite scaffolds", ***Advanced Ceramics Progress***, Vol. 4, (2018), 8-15. DOI:10.30501/acp.2018.92930
35. Arianpour, F., Golestani Fard, F., Rezaie, H., "Spark Plasma Sintering of Ultra-High Temperature Tantalum/Hafnium Carbides Composite", ***Advanced Ceramics Progress***, Vol. 2, No. 1, (2016), 13-18. DOI:10.30501/acp.2016.70013
36. Moshtaghioun, B.M., Gomez-Garcia, D., Dominguez-Rodriguez, A., Todd, R.I., "Grain size dependence of hardness and fracture toughness in pure near fully-dense boron carbide ceramics", ***Journal of the European Ceramic Society***, Vol. 36, No. 7, (2016), 1829-1834. DOI:10.1016/j.jeurceramsoc.2016.01.017

ACERP: Vol. 6, No.2, (Spring 2020) 30-34

Advanced Ceramics Progress

Research Article

Journal Homepage: www.acerp.ir

Preparation and Characterization of $Y_3A_5O_{12}$: Cr^{3+} Nanophosphor by Electrochemical Technique

M. Hosseinifard [a *], H. Goldooz [b], A. Badiei [b], A. Kazemzadeh [a]

[a] *Department of Semiconductors, Materials and Energy Research Center (MERC), Meshkin Dasht, Alborz, Iran*

[b] *School of Chemistry, College of Science, University of Tehran, Tehran, Iran*

PAPER INFO

Paper history:

Received 28 May 2020
Accepted in revised form 20 June 2020

Keywords:

YAG: Cr
Hydroxide Precursors
Electrodeposition
Emission

ABSTRACT

$Y_3A_5O_{12}$:Cr^{3+} nanophosphor was synthesized by cathodic electrodeposition method. During the preparation procedure, hydroxide precursors were deposited on the surface of cathode via electrochemical reaction and then the final product was achieved by heat treatment of obtained powder at 1100 °C for 4 h. The structure and properties of the obtained product were investigated by various analysis methods such as X-Ray Diffraction (XRD), Fourier Transform InfraRed (FTIR) Spectroscopy, Photoluminescence Spectroscopy (PL), Scanning Electron Microscopy (SEM) and N_2 adsorption-desorption analysis. The XRD patterns of the synthesized YAG: Cr product, were in good match with the pure $Y_3Al_5O_{12}$ phase and the absence of any other impurities indicates the transformation of Cr^{3+} ions into the host matrix (YAG). In the emission spectrum of prepared material, a broad emission containing four pronounced bands at 685, 695, 710 and 725 nm was observed that indicates the presence of Cr^{3+} ions in the final product and further confirmed the formation of desired oxide product (YAG: Cr). The results of our studies showed that cathodic electrodeposition is a practical and highly efficient method for preparation of $Y_3A_5O_{12}$:Cr^{3+} nanophosphor compound.

1. INTRODUCTION

A phosphor material can absorb the electromagnetic radiation from Light Emitting Diodes (LED) and transform it into visible light. The emitted light can be tuned to form a broad (for lighting) or narrow (for solid state lasers) emission spectrum by engineering the phosphor layer structure, morphology and composition. Rare-earth or metal ions activated Yttrium Aluminum Garnets (YAG phosphors) are important crystal materials due to their good chemical, physical, creep resistance and optical properties, used in solid state lasers, Light-Emitting Diodes (LEDs) and so on [1-6]. For example, the optical properties of YAG pure phase doped with transition metal ions (Cr^{4+}, V^{3+}, Cr^{3+} and Co^{2+}) and lanthanide ions (Ce^{3+}, Eu^{3+}, $Sm^{3+}$and Tb^{3+}) for application as phosphor materials have been studied in many papers [7-13]. Typically, solid state reactions of oxide materials at high temperature (above 1500 ^oC) are carried out for synthesis of YAG phosphors and to obtain nanoscale powder of compounds, mechanical milling is often used.

In recent years, several methods have been employed to prepare pure YAG and YAG phosphor such as sol-gel, co-precipitation, solvothermal, combustion and electrochemical method [13-17,21]. Among these methods, electrochemical methods (e.g. cathodic electrodeposition) are in general, simple, low cost, and suitable technique that can be used as an effective method for the synthesis of YAG nanophosphor due to its powerful control on the structure of the hydroxide deposit which can be easily tuned by controlling the base electrogeneration [18-20]. In this method, the hydroxide ions, electrogenerated on the surface of cathode by reduction of water molecules, are reacted with the cations in the bath solution, containing appropriate chloride salts in required stoichiometric amount, to form the final YAG product and as a consequence a hydroxide gel is deposited on the surface of steel substrate (cathode).

* Corresponding Author Email: m.hosseini@merc.ac.ir (M. Hosseinifard)

https://doi.org/10.30501/acp.2020.109547

Heat-treatment of electrodeposited material results in obtaining desired YAG phosphor product.

In this paper, we report the preparation of YAG: Cr ($Y_3Al_5O_{12}:Cr^{3+}$) nanophosphors by cathodic electrodeposition from a bath solution containing suitable chloride salts, at 25 ºC and using a current density of 1 $mAcm^{-2}$, followed by heat-treatment of obtained electrodeposited material. There are a few reports for preparation of YAG compounds through cathodic electrodeposition method [18-20] and we have previously employed this method to prepare some YAG samples [22] but as far as we know there is no report in the literature for synthesis of YAG: Cr^{3+} nanophosphor by means of cathodic electrodeposition.

2. EXPERIMENTAL PROCEDURES

2.1. Chemicals

Aluminum chloride anhydrous ($AlCl_3$) Chromium (III) nitrate nonahydrate ($Cr(NO_3)_3\ _9H_2O$) as well as Yttrium(III) chloride hexahydrate ($YCl_3\ .6H_2O$) (Aldrich), and ethanol 96 % (Merck).

2.2. Synthesis procedure

An electrochemical cell, containing a cathodic steel substrate placed between two parallel graphite anodes, was used to perform cathodic electrodeposition. The required amount of metal salts for preparation of YAG: Cr were dissolved in a 1:3 water-ethanol mixture and served as electrolyte solution in the cell's bath. The steel substrate was electropolished prior to each deposition. [18-20].

A constant current density of 1 $mAcm^{-2}$ at 25 ºC for 2 h was used to perform deposition experiments. Then, the formed gel-like material on the cathodic steel electrode was scraped and air dried at room temperature for 5 h. At the end, the dried powder of component was heat treated at 1100 °C in air for 4 h in order to conversion of hydroxide precursor into the final oxide product.

2.3. Characterization

A Phillips PW-1800 diffractometer (equipped with a Cu Kα radiation source) was employed to evaluate the crystal structure with ranging from 10 to 70 (scanning rate: 5 degrees per minutes). The FT-IR spectra of the YAG and YAG: Cr materials were analyzed on a RAYLEIGH WQF- 510A apparatus. Fluorescence spectra were recorded on Agilent G980A instrument. The surface morphology of the prepared YAG powder was studied using a scanning electron microscope (TESCAN VEGA3 Model). The specific surface area and pore size distribution of the sample was measured via N_2 adsorption–desorption analysis at 77 K performed by a BELSORP Mini II.

3. RESULTS AND DISSCUSSION

3.1. XRD and FT-IR analysis

The XRD patterns of the YAG and Cr^{3+} doped YAG synthesized via the cathodic electrodeposition method at 1100 ºC are depicted in Fig.1a-b [18]. All diffraction peaks correspond to the pure $Y_3Al_5O_{12}$ phase (JCPDS No.082-0575) and no other impurities were observed for YAG: Cr^{3+} (Fig. 1b), indicating that Cr^{3+} ions have been transformed into YAG host framework and the original structure of YAG has remained intact [7-8, 18-20]. The lattice parameter of YAG: Cr is a bit larger than the standard value of cubic YAG, because of a small lattice distortion resulted from the slightly larger radius of Cr^{3+} ions in comparison with Al^{3+} ions [19]. The average sizes of YAG and YAG: Cr particles were determined by means of Scherrer equation [20]. It was found that average grain size of YAG and YAG: Cr nanopowders were around 48 nm and 57 nm respectively.

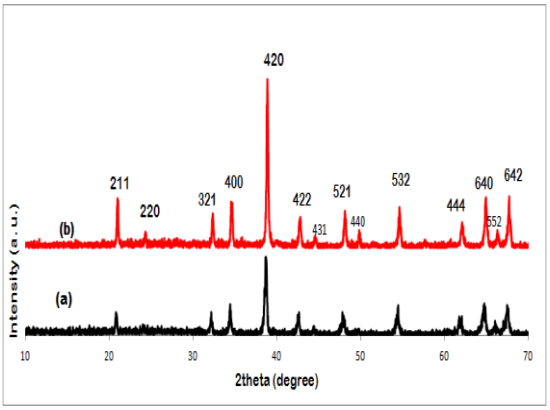

Figure 1. XRD patterns of (a) YAG and (b) YAG:Cr samples

The FTIR spectra of the YAG and YAG: Cr powders are shown in Fig. 2. The characteristic peaks at 722 and 790 cm^{-1} correspond to the stretching modes of the AlO_6 octahedral in the YAG cubic structure. characteristic peaks at 521, 688 and 570 cm^{-1} are attributed to the stretching modes of AlO_4 tetrahedral. The bands located below 900 cm^{-1} are ascribed to M-O vibrations [18-20].

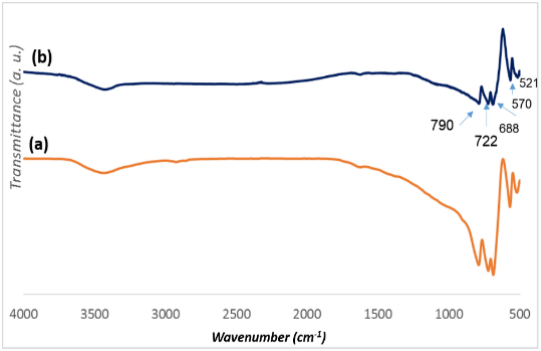

Figure 2. FTIR spectra of (a) YAG and (b) YAG: Cr samples

3.2. Photoluminescence analysis

The emission spectrum of YAG: Cr^{3+} nanophosphor prepared by cathodic electrodeposition method is shown in Fig.3. The spectrum was produced via spin allowed $^4A_2 \rightarrow {}^4T_1$ and $^4A_2 \rightarrow {}^4T_2$ transition of Cr^{3+} ions with the excitation wavelength at 617nm. Four pronounced bands at 685, 695, 710 and 725 nm were observed in the emission spectrum. The observed bands in the emission spectrum are in good correspondence with the reported results in the literature for YAG: Cr^{3+} nanophosphors that are synthesized via other methods [8]. The line at 695 is result of the Cr^{3+} zero phonon $^2E \rightarrow {}^4A_2$ transition, while its associated stokes phonon side bands are near 710 and 725 nm and anti-stokes phonon side band was observed at 685 nm [7-8].

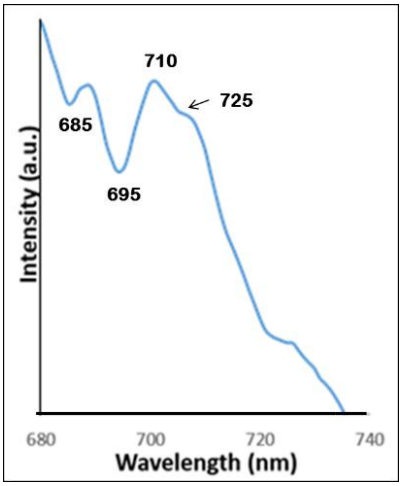

Figure 3. Photoluminescence emission spectrum of YAG: Cr nanophosphor sample

3.3. Surface morphology and EDX analysis

The morphology of the synthesized YAG: Cr nanophosphor was characterized by SEM (Fig. 4a). According to the SEM image, the spherically shaped nanoparticles can be observed in the porous background. While some particles are agglomerated as clusters but individual particles of about 100 nm are clearly visible. The representative EDX pattern of YAG: Cr nanophosphor is depicted in Fig. 4b. The existence of Al, Y, O and Cr peaks confirms formation of the synthesized YAG: Cr^{3+} component.

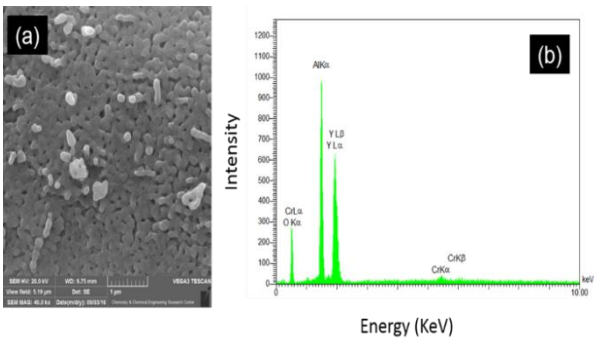

Figure 4. (a) SEM image and (b) EDX spectrum of the synthesized YAG: Cr nanophosphor component

3.4. N_2 adsorption-desorption analysis

The Brunauere, Emmete and Teller (BET) method was used to calculate the SSA of YAG: Cr nanophosphor. The PSD and N_2 isotherm are shown in Fig. 5. The attained isotherm could be classified as the type-III isotherm and the H_2 hysteresis loop based on the IUPAC classification which is characteristic for mesopore structure.

The pore diameter (BJH method) and the surface area of YAG: Cr nanophosphor was determined as 44 nm and 47 $m^2\ g^{-1}$, respectively [24-25] that are in good agreement with the reported amounts for YAG nanophosphors synthesized via other methods [25].

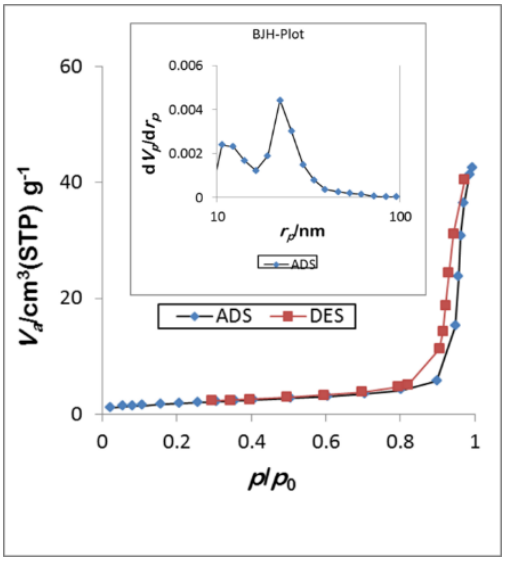

Figure 5. N_2 isotherm of the synthesized YAG: Cr nanophosphor sample (inset: PSD curve of YAG: Cr sample)

4. CONCLUSION

The cathodic electrodeposition method was successfully used to synthesis YAG: Cr nanophosphor and the prepared compound were characterized by various analytical methods. The XRD pattern confirms the incorporation of the Cr^{3+} ions into the YAG framework. The SEM and EDAX analyses show that the prepared material contains spherically shaped nanophosphor particles which are mainly composed of Y, Al, O and Cr elements. Some particles are also observed to be agglomerated as clusters. The PL spectrum confirmed the presence of Cr^{3+} ions in YAG nanomaterial and the N_2 adsorption-desorption analysis revealed the porous structure of YAG: Cr^{3+} with relatively narrow pore size distribution.

5. ACKNOWLEDGEMENTS

The authors are extremely appreciative to the Materials and Energy Research Center (MERC), Karaj, Iran through Grant No. 9911940.

REFERENCES

1. Blasse, G., Bril, A., "A new phosphor for flying-spot cathode-ray tubes for color television: yellow emitting $Y_3Al_5O_{12}$-Ce^{3+}", ***Applied Physics Letters***, Vol. 11, No. 2, (1967), 53–55. DOI:10.1063/1.1755025
2. Piao, X. Q., Horikawa, T., Hanzawa, H., Machida, K. I., "Characterization and luminescence properties of $Sr_2Si_5N_8$: Eu^{2+} phosphor for white light-emitting-diode illumination", ***Applied Physics Letters***, Vol. 88, No. 16, (2006), 161908. DOI:10.1063/1.2196064
3. Wang, D. Y., Huang, C. H., Wu, Y. C., Chen, T. M., "$BaZrSi_3O_9$: Eu^{2+}: a cyan-emitting phosphor with high quantum efficiency for white light-emitting diodes", ***Journal of Materials Chemistry***, Vol. 21, No. 29, (2011), 10818–10822. DOI:10.1039/C1JM00080B
4. Geng, D., Li, G., Shang, M., Yang, D. M., Zhang, Y., Cheng, Z., Lin, J., "Color tuning via energy transfer in Sr^{3+} In $(PO_4)_3$:Ce^{3+}/Tb $^{3+}$/Mn^{2+} phosphors", ***Journal of Materials Chemistry***, Vol. 22, No. 28, (2012), 14262–14271. DOI:10.1039/C2JM32392C
5. Bardsley, N., Bland, S., Chwastyk, D., Monasterio, C. D., Pattison, L., Pattison, M., Welsh, F., Yamada, M., ***Solid state Lighting Research and Development, Manufacturing Roadmap***, U.S. Department of Energy, Office of Energy Efficiency and Renewable Energy, (2013). Available at: http://apps1.eere.energy.gov/buildings/publications/pdfs/ssl/ssl_manuf-roadmap_sept2013.pdf (Accessed: September 2013)
6. Lin, Y. C., You, J. P., Tran, N. T., He Y., Shi, F. G., "Packaging of phosphor based high power white LEDs: effects of phosphor concentration and packaging configuration", ***Journal of Electronic Packaging***, Vol. 133, No. 1, (2011), 011009-0011014. DOI:10.1115/1.4003216
7. Gluchowski, P., Pązik, R. , Hreniak, D., Stręk, W., "Luminescence properties of Cr^{3+}: $Y_3Al_5O_{12}$ nanocrystals", ***Journal of Luminescence***, Vol. 129, No. 5, (2009), 548–553. DOI:10.1016/j.jlumin.2008.12.012
8. Smith, B. A., Dabestani, R. T., Lewis, L. A., T., Thompson, C. V., Collins, C. T., Aytug, C., "Synthesis and Luminescence Characteristics of Cr^{3+} doped $Y_3Al_5O_{12}$ Phosphors", (No. ORNL/TM-2015/627). Oak Ridge National Lab.(ORNL), Oak Ridge, TN (United States) (2015). DOI:10.2172/1223077
9. Dudnikova, V. B., Zharikov, E. V., Urusov , V. S., "Concentration of Cr^{4+} impurity ions and color centers as an indicator of saturation of forsterite crystals Mg_2SiO_4 with oxygen", ***Physics of the Solid state***, Vol. 52, No. 9, (2010), 1865–1873. DOI:10.1134/S1063783410090131
10. Ali, H., Abou Kana, M. T., Khedr, M. A., "Spectroscopy and Optical Properties of Sm^{3+}: YAG Nano crystalline Powder Prepared by Co-Precipitation Method: Effect of Sm^{3+} Ions Concentrations", ***Open Journal of Applied Sciences***, Vol. 4, (2014), 96-102. DOI:10.4236/ojapps.2014.43011
11. Li, X., Li, Q., Wang, J., Yang, S.,, "Synthesis of YAG: Eu phosphors with spherical morphology by solvo-thermal method and their luminescent property", ***Materials Science and Engineering: B***, Vol. 131, No. 1-3, (2006), 32–35. DOI:10.1016/j.mseb.2005.12.022
12. Zhou, S., Fu, Z., Zhang, J., Zhang, S., "Spectral properties of rare-earth ions in nanocrystalline YAG: Re (Re = Ce^{3+}, Pr^{3+}, Tb^{3+})", ***Journal of Luminescence***, Vol. 118, No. 2, (2006), 179–185. DOI:10.1016/j.jlumin.2005.08.011
13. Yang, H., Kim, Y. S., "Energy transfer-based spectral properties of Tb-, Pr-, or Sm co doped YAG: Ce nanocrystalline phosphors", ***Journal of Luminescence***, Vol. 128, No. 10, (2008), 1570–1576. DOI:10.1016/j.jlumin.2008.03.003
14. Ma, X., Lv, Z., Tan, H., Nan, J., Wang, C., Wang, X., "Preparation and grain-growth of chromia-yttrium aluminum garnet composites fibers by sol–gel method", ***Journal of Sol-Gel Science and Technology***, Vol. 83, No. 2, (2017), 275-280. DOI:10.1007/s10971-017-4410-3
15. Sheu, H. H., Jian, S. Y., Lin, T. T., Lee, Y. W., "Effect of rotational speed of an electromagnetic stirrer on neodymium-doped yttrium aluminum garnet nanoparticle size during co-precipitation", ***Microelectronic Engineering***, Vol. 176, (2017), 33-39. DOI:10.1016/j.mee.2017.01.020
16. Ramanujam, P., Vaidhyanathan, B., Binner, J., Ghanizadeh, S., Zhou, Z., Spacie, C., "Rapid synthesis of nanocrystalline YAG via microwave assisted solvothermal process", ***Journal of the American Ceramic Society***, Vol. 101, No. 11, (2018), 4864-4869. DOI:10.1111/jace.15815
17. Carreira, J. F. C., Sedrine, N. B., Monteiro, T., Rino, L., "YAG: Dy–Based single white light emitting phosphor produced by solution combustion synthesis", ***Journal of Luminescence***, Vol. 183, (2017), 251-258. DOI:10.1016/j.jlumin.2016.11.017
18. Hosseinifard, M., Badiei, A., Ahmadi, K., "Synthesis and characterization of yttrium aluminum garnet nanostructures by cathodic electrodeposition method", ***Advanced Powder Technology***, Vol. 28, No. 2, (2017), 411-418. DOI:10.1016/j.apt.2016.10.012
19. Hosseinifard, M., Goldooz, H., Badiei, A., Ahmadi, K., "Synthesis, Characterization and Luminescence Properties of YAG:RE (Ce, Sm and Gd) Nanophosphor by Cathodic Electrodeposition Method", ***Russian Journal of Electrochemistry***, Vol. 56, No. 2, (2020), 174–179. DOI:10.1134/S102319352001005X
20. Hosseinifard, M., Ahmadi, K., Badiei, A., "Cathodic Electrodeposition and Characterization of YAG Nanostructure: Effect Current Density on the Morphology", ***Advanced Ceramics Progress***, Vol. 4, No. 2, (2018), 32-36. DOI:10.30501/ACP.2018.91123
21. Patterson, A. L., "The Scherrer Formula for X-Ray Particle Size Determination", ***Physical Review***, Vol. 56, No. 10, (1939), 978. DOI:10.1103/PhysRev.56.978
22. Aghazadeh, M., Dalvand, S., Hosseinifard, M., "Facile electrochemical synthesis of uniform β-Co $(OH)_2$ nanoplates for high performance supercapacitors", ***Ceramics International***, Vol. 40, No. 2, (2014), 3485-3493. DOI:10.1016/j.ceramint.2013.09.081

23. Țălu, Ș., ***Micro and nanoscale characterization of three dimensional surfaces. Basics and applications***, Napoca Star Publishing House, Cluj-Napoca, Romania, (2015).
24. Mwema, F. M., Akinlabi, E. T., Oladijo, O. P., Fatoba, O. S., Akinlabi, S. A., Țălu, Ș., "Chapter two - Advances in manufacturing analysis: fractal theory in modern manufacturing" In Kumar, K., Davim, J. P., (eds.), ***Modern Manufacturing Processes***, Woodhead Publishing Reviews: Mechanical Engineering Series, (2020), 13-39. DOI: 10.1016/B978-0-12-819496-6.00002-6
25. Muresan, L. E., Popovici, E. J., Bica, E., Cadis, A. I., Perhaita, I., Tudoran, L. B., "Investigation of thermal decomposition of yttrium–aluminumbased precursors for YAG phosphors", ***Journal of Thermal Analysis and Calorimetry***, Vol. 110, No. 1, (2012), 341-348. DOI:10.1007/s10973-012-2374-7

ACERP: Vol. 6, No.2, (Spring 2020) 35-42

Advanced Ceramics Progress

Research Article

Journal Homepage: www.acerp.ir

Synthesis of FAp, Forsterite, and FAp/Forsterite Nanocomposites by Sol-gel Method

S. Manafi [a *], F. Mirjalili [b], S. Joughehdoust [c]

[a] *Department of Materials Engineering, Shahrood Branch, Islamic Azad University, Shahrood, Iran*
[b] *Department of Materials Engineering, Maybod Branch, Islamic Azad University, Maybod, Iran*
[c] *Department of Urology, Maastricht University, The Netherlands*

PAPER INFO

Paper history:

Received 2 June 2020
Accepted in revised form 24 June 2020

Keywords:

Fluorapatite
Forsterite
Nanocomposite
Biomaterials

ABSTRACT

The present study aims to investigate the preparation and evaluation of phase and morphological properties of a nano biocomposite ceramic. In this regard, the synthesis of fluorapatite (FAp) as the first phase and forsterite considered as the second phase by the sol-gel method was taken into account. Then, nanocomposites with the base of fluorapatite with 15, 25, and 35 wt% of forsterite were synthesized using the sol-gel method. The synthesized nanoparticles and nanocomposites were characterized by using different techniques, Field Emission Scanning Electron Microscope (FESEM), X-Ray Powder Diffraction (XRD), and Fourier-Transform Infrared (FT-IR) Spectroscopy. X-ray diffraction test results as well as infrared spectroscopy indicated that fluorapatite, forsterite, and fluorapatite/forsterite nanocomposites were produced without impurity. FESEM result showed that the particle sizes of the produced nanocomposites with 15, 25, and 35 wt% of forsterite ranged approximately between 25 and 80 nm. The result of the MTT assay proved the nontoxicity of samples for 7 days.

1. INTRODUCTION

Bone is a live connective tissue that supplies structural funding to the body organs and is an emergency reservoir of calcium in the correction phase in case of a disease or some pathological processes throughout life [1,2]. Bacterial infection is a severe problem that follows implant surgery in orthopedics and dentistry [3,4]. Numerous studies have pointed out the positive results of bioactive bioceramics regarding bone cell growth [5-6]. The perfect biomaterials for orthopedics may support the mechanical properties and biocompatibility during the period of establishment [7,8]. The agents that demoand hydroxyapatite contain a high degree of decomposition in biological organizations and *in vivo* solubility, which leads to a decrease in use of hydroxyapatite in long-term requests [9-11]. Nevertheless, its biological and physicochemical properties can be strengthened by replacing ions that usually exist in natural bone apatite [10,12].
The inherent brittleness of glass is the major limitation of using bioactive glass as tissue-engineering scaffolds [13,14]. It was discovered that replacing fluoride ions in the hydroxyapatite structure would significantly increase biodegradability. Furthermore, the enhanced absorption of protein expresses a tougher cellular construction and supports the movement of phosphates that create stouter osteoconductivity [15,16]. If OH^- sets in HA are entirely substituted with F^-, fluorapatite [$Ca_{10}(PO_4)_6F_2$] will be prepared [12,17], which has more chemical and structural constancy equated with hydroxyapatite [18-20]. The ion exchange has a positive effect on propagation, morphology, and differentiation of osteoblast-like cells and enhances bioactivity [21,22]. Fluorapatite also forms the external layer of the tooth [19]. The mineral phase of the tooth under the enamel comprises about 0.04-0.07 wt% fluorine [17,23]. The enamel contains fluorapatite with substitution of 50% F^- with OH^- [24].
In 2019, Nguyen and his colleagues established the forsterite bioceramics by using the sol-gel method. Their results designate the adhesion, proliferation, and growth of bone marrow cells on the forsterite ceramic surface. As a result, forsterite ceramic as an ideal bioservice can

* Corresponding Author Email: ali_manafi2005@yahoo.com (S. Manafi)
https://doi.org/10.30501/acp.2020.109549

be appropriate for bone tissue repair. Another research defined biocompatibility of forsterite. In addition, the elasticity of forsterite and its adhesion to dense and spongy bones were among the significant parameters in its collection as biomedical material [25-27].

Forsterite is a magnesium silicate mineral with the chemical formula of $2MgO.SiO_2$. It is a magnesium-rich end-member of the olivine solid solution series with a comparatively high melting point of 1890 °C for refractory demand [27].

Bioactive ceramics have been established in medical demands as a bone substitute material for ruptures. Calcium phosphate ceramics such as hydroxyapatite (HAp: $Ca_{10}(PO_4)_6(OH)_2$) and forsterite are broadly applied as implant materials owing to their biocompatibility with and close semblance to the mineralized phase of human bone structures [1], which can facilitate the formation of new bone with the neighboring tissue [28]. Nanomaterials enjoy an enormously wide range of possible applications from nanoscale optics and electronics to nano-biological systems and nano-medicine. The following methods have been used to synthesize nanosized particles: sol-gel, hydrothermal, solvothermal, sonochemical, direct oxidation, electrodeposition, micelle, and inverse micelle usage, emulsion or hydrolysis precipitation, chemical/physical vapor deposition, microemulsion processes, microwave approaches, and ultrasonic [6-9]. Among the numerous preparation techniques, sol-gel is considered one of the simplest methods for synthesizing nanoparticles in ambient conditions. Besides, it does not require complicated setup and the experimental conditions can be easily controlled [9,11,12]. In addition, sol-gel process can be controlled to obtain the required oxide with a high degree of homogeneity and purity [22].

Likewise, HA and forsterite can be made from natural sources with calcium-based structures such as bovine bone, mollusk shell, or corals [29]. Consequently, these materials may be considered as cost-effective biomaterials for bone tissue engineering in bone graft applications. HA is presently used as implant material in orthopedic surgery and dental implant due to its biocompatibility, osteoconductivity, and chemical similarity to the human skeletal system [5]. It has a calcium-to-phosphate ratio of 1.67, which is homologous to natural human bone [26]. Conversely, bulk HA cannot be used as load-bearing implants due to low mechanical properties such as great brittleness [27]. To this end, investigators have previously attempted to combine HA with forsterite to develop composite biomaterials structure with enhanced mechanical and biological properties [28]. This grouping may be attained through sintering; however, sintering above 597 °C would source forsterite crystallization [29]. The $Na_2Ca_2Si_3O_9$ crystalline phase formed recovers the mechanical property [29] and bioactive response [26].

The combination of fluorapatite particles with forsterite affords its special properties such as augmentation of bioactivity and mechanical properties.

The present study aims to synthesize and characterize fluorapatite, forsterite, and fluorapatite/forsterite nanocomposite by the sol-gel method for bone tissues. The novelties of this research are exploring the effect of different percentages of forsterite for preparing the fluorapatite-forsterite nanocomposite, investigationg the morphological and microstructure properties of fluorapatite-forsterite nanocomposites and fluorapatite, and considering forsterite nanoparticles.

The present study aims to develop and evaluate a ceramic nanosized composite with properties close to bone properties and good biocompatibility for dentistry and orthopedics applications as a bone constructor.

2. EXPERIMENTAL PROCEDURES

2.1. Preparation of FAp Powder

First, 5.91 g hydrated calcium nitrate ($Ca(NO_3).4H_2O$, 98%, Merck, CN)) was dissolved in 20 ml absolute (98%, Merck, ET)/water (W) and then, another solution was made by dissolving 1.36 g triethyl phosphate (97%, Merck, EP) in 20 ml ET/W. Then, 0.28 g fluoride ammonium (97%, Merck, FAp) was dissolved in 20 ml (ET)/W. Three solutions were stirred to obtain transparency for 24 h. At the second step, the calcium solution was added dropwise at a rate of 5 ml/min to phosphate solution with vigorous stirring for 72 h. A milky and gelatinous precipitate was obtained. The obtained precipitates were centrifuged and washed by ethanol four times, dried at 80 ºC for 5 h, and subsequently ground with mortar and pestle. Finally, the resulting fine fluorapatite powders were heated to 550 °C for 1 h.

2.2. Preparation of Forsterite

In order to prepare forsterite (FO), aqueous magnesium nitrate (98%, Merck, MN) solution was prepared in 50 cc distilled water. After the dissolution of magnesium nitrate in distilled water on a magnetic stirrer, colloidal silicon oxide with the molar ratio of magnesium to silicon 2:1=Si: Mg was added and the magnetic stirrer was homogenized. The required amount of sucrose was dissolved in 100 cc of distilled water and added to the mentioned solution. After 2 h of homogenization at ambient temperature, polyvinyl alcohol (Merck, 96%, PVA) solution was distilled in 20 cc of water with magnesium to polyvinyl alcohol ratio of 0.8 and added to the mentioned solution. The pH was adjusted to 1. To uniformly distribute the raw materials and accelerate the

hydrolysis process, the above solution was stirred by a magnetic stirrer for 2 h at ambient temperature of 80 °C. Subsequently, to complete the hydrolysis and polymerization processes of the precursors and to ensure sufficient time for the ions to be uniformly distributed in the structure, aging operations were carried out at ambient temperature for 24 h and dried at 100 °C and sintered at 900 °C for 2 h.

2.3. Preparation of Fap/Forsterite Nanocomposite

To synthesize FAp/forsterite nanocomposites with 15, 25, and 35% wt% of forsterite, three sols were prepared. First, 5.91 g of calcium nitrate of tetrahydrate ($Ca(NO_3)_2.4H_2O$, 98%, Merck, CN) in 20 ml absolute ET/W solution (75% -25%) was dissolved. Then, 1.365 g triethyl phosphate (99%, Merck, TP) in 20 ml absolute ET / W (75%-25%) was stirred for 1 h. In the meantime, 0.28 g ammonium fluoride (99%, Merck, AF) was dissolved in 20 ml absolute ET/W (75-25%) and stirred at 45 °C. Finally, forsterite powder with 15, 25, and 35wt% was added to the final solution and stirred for 48 h. Furthermore, the solutions were dried for 24 h at 110 °C and sintered at 600 °C for 2 h. The sample names are shown in Table 1.

TABLE 1. The name of the samples

Code	Sample
FAp	Fluorapatite of 100%
FAp-F-15	Fluorapatite-Forsterite of 15%
FA-F-25	Fluorapatite-Forsterite of 25%
FA-F-35	Fluorapatite-Forsterite of 35%
FO	Forsterite of 100%

2.4.Characterization of FAp/Forsterite Nanocomposite

Phase identification was performed by X-Ray Diffraction (XRD) PW1800, of Philips Company, using nickel-filtered CuK_α radiation in the range of 2θ=10-60° at a scanning speed of 5° per minute. A Perkin Elmer Spectrum 100 series Fourier FT-IR (Transform Infrared Spectrometer) was used in conjunction with the Universal Attenuated Total Reflection (UATR) method. Microstructures of powders were identified by transmission electron microscope (Philips–Zeiss-Germany), Scanning Electron Microscopy (SEM PHENOM), and field Emission Scanning Electron Microscope (FESEM).

2.5. Evaluation of Cell Survival By MTT Test

At the next step, the proliferation and survival of L929 cells on the surface of the samples were evaluated by MTT assay. To prepare the samples, a common protocol for this test was used. In this way, 5 mg of each sample was mixed in the medium and incubated at 37 °C for 7 days. The stored stock of MTT solution was added to the control and the treated cell line samples and again incubated at 37 °C for 3 h. Then, the medium was removed and mixed with solubilizing buffer. During this process, the MTT ring was broken, thus creating crystalline purplish color. The intensity of this color was directly related to the living cells. Next, the supernatant was discarded and the cells were washed. Finally, the absorbance of the solution was calculated by the spectrophotometer. The following formula was then used to determine the survival rate:

Cell Viability% = ODs/ODc

ODs Optical Density Sample, ODc Optical Density Control.

3. RESULTS AND DISSCUSSION

3.1. X-Raydiffraction Analysis of Forsterite, FAp, FAp/Forsterite Nanocomposite

Fig. 1(a) shows the XRD patterns of the forsterite powder. Based on the X-ray diffraction pattern, it represents a broad and longer form expressing the amorphous structure of the synthesized nanopowder. The peaks belonging to the crystalline phases are visible at angles of 22.81, 23.89, 29.53, 44.57, 64.94, and 65.59°, depending on the effects of crystalline phases of forsterite (JCPDS No. 00-004-0769).

X-ray diffraction pattern of nano-powdered synthetic FA is shown in Fig. 1(b). It was discovered that all the peaks identified in the diffraction pattern were related to the structure of fluorapatite with JCPDS No.00-003-0736 with a hexagonal crystal structure. The peaks belonging to the crystalline phases were visible at angles of 21.78, 25.77, 28.99, 48.19, 60.13, and 63.07°. Based on interpretation of the diffraction pattern, it can be concluded that this structure is well crystallined.

Figs. 1(c-e) show the X-ray diffraction pattern of the FAp/forsterite nanocomposites. The synthetic nanosized particles were distinguishable from the synthesized composite dispersion pattern. Based on the examined patterns, it can be conluded that these patterns are very difficult to be distinguished due to the overlapping of the peak of the forsterite with apatite peaks.

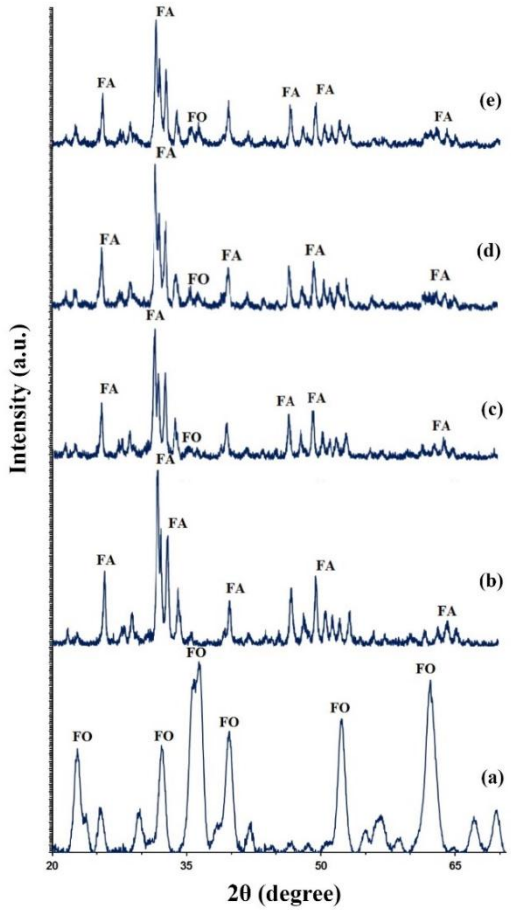

Figure 1. X-ray diffraction pattern of a) nano-powdered synthetic FO; b) nano-powdered synthetic FAp; c) FAp-F-15 nanocomposite; d) FAp-F-25 nanocomposite; e) FAp-F-35 nanocomposite

However, the most significant peak of forsterite, the one at 2θ=36.53°, was detectable in all patterns due to lack of overlap with the fluorapatite peaks; in addition, its intensity increased as the forsterite weight percentage increases. Mazrooei Sebdani et al. discovered that the crystallite size increased by enhancing the Forsterite phase in hydroxyapatite–forsterite–bioactive glass nanocomposite coatings [30]. In another research, Forghani et al. found no grain growth during calcination in Fluorapatite- Forsterite Nanocomposite [31]. However, no significant changes in the crystallinity in XRD peaks were detected in this study.

3.2. Infradspectroscopy Analysis of Forsterite, FAp, FAp/Forsterite Nanocomposite

Forsterite characteristic bands mainly consist of two main categories: one visible peak at 890-1090 cm^{-1}, 841 cm^{-1}, and 614 cm^{-1} corresponding to SiO_4 group vibrational modes, and the other two peaks at 425 cm^{-1} and 2510 cm^{-1} regarded as vibrational modes of octahedral of MgO [27,28].

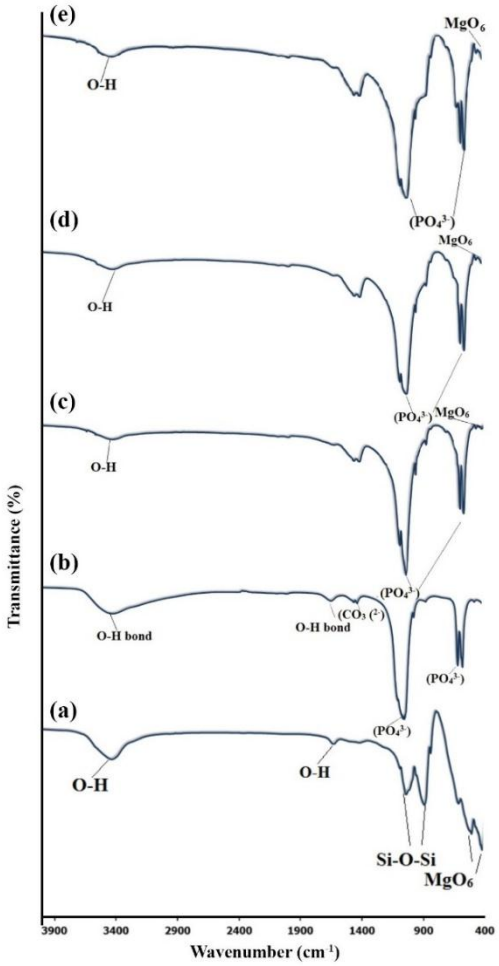

Figure 2. Infrared spectroscopy analysis of a) nano-powdered synthetic FO; b) nano-powdered synthetic FAp; c) FAp-F-15 nanocomposite; d) FAp-F-25 nanocomposite; e) FAp-F-35 nanocomposite

In the FTIR spectrum of pure forsterite, the peaks at 1634 cm^{-1} and 3433 cm^{-1} corresponded to the bending vibrations of water molecules adsorbed on the surface of nanoparticles and tensile vibrations of the O-H group in the water molecule. The peak at 1044 cm^{-1} was due to the tensile vibrations of Si-O-Si bonds in the silicate lattice in the forsterite [29]. Except for the characteristic peaks mentioned, no other peaks related to the structural impurities in the spectrum could be observed, which might confirm the structural purity of the synthesized sample (Fig. 2(a)).

Fig. 2(b) shows the FTIR spectrum of the synthesized fluorapatite nanoparticles. The relevant FTIR spectrum

had all vibrations from v_4 to v_1 related to the phosphate group in the structure of apatite [16]. Finally, there were two courier sharps of 564 cm^{-1} and 603 cm^{-1} belonging to the group of v_4 vibrations [17]. The presented peak at 741 cm^{-1} represented the hydroxyl chain, which was found in this structure that was rich in fluorine [21]. The peaks at 1640 cm^{-1} and 3700 cm^{-1} were related to O-H groups. A central peak of 873 cm^{-1} along with a band with two edges of 1413 cm^{-1} and 1465 cm^{-1} were attributed to structural carbonate (CO_3^{2-}) groups [19]. The presence of this group proved the bioavailability of fluorapatite.

FTIR spectra of fluorapatite-forsterite composites with 15, 25, and 35 wt% of forsterite contained absorption peaks corresponding to each component (Figs. 2(c-e)). As shown, the FTIR curve of nanocomposites did not significantly change by adding different percentages of forsterite. However, the intensities of the forsterite characteristic peaks, especially the peaks at 510 cm^{-1}, 890 cm^{-1}, and 1040 cm^{-1}, gradually increased as the weight percentage of the forsterite in the composite samples increased.

3.3. Morphological Properties of Forsterite, FAp, FAp/Forsterite Nanocomposite

Field Emission Scanning Electron Microscopy (FESEM) images of fluorapatite, forsterite, and fluorapatite/forsterite nanocomposites with different forsterite percentages are presented in Figs. 3 and 5. Fig. 3(a) depicts the FESEM images of synthesized forsterite. It can be noted that the nanoparticle is characterized by spherical morphology with some agglomeration due to the intrinsic nature of nanoparticles, and their particle size ranged from 48 to 25 nm. Fig. 3(b) shows the FESEM microsphere of the synthesized fluorapatite nanoparticles. In addition, the formation of nanometric particles with spherical morphology and a particle size range of 23-30 nm are given.

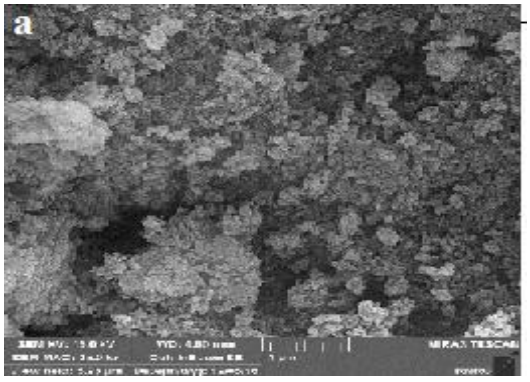

(a)

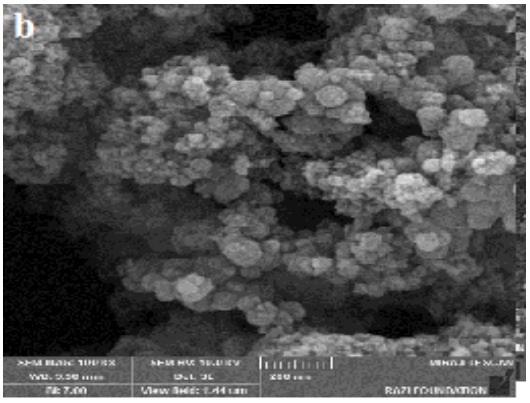

(b)

Figure 3. Field emission scanning images of a) FO, b) FAp

According to Fig. 4(a), the EDS pattern of the synthesized FO particles showed the major constituent elements, namely silicon, magnesium, and oxygen, at the atomic ratio close to the stoichiometric sample of Mg_2SiO_4. The pattern showed no impurity, indicating the high elemental purity of the synthetic forsterite particles. According to Fig. 4(b), the EDS pattern of the fluorapatite nanoparticles indicated that the nanoparticles were composed of four dominant elements: calcium, phosphorus, fluorine, and oxygen, which were essentially the constituent elements of fluorapatite according to the experimental $Ca_5(PO_4)_3F$ formula. The EDS pattern did not show the peaks characteristic of other impurities, which could be considered as a good criterion for the high elemental purity of the synthesized nanoparticles.

FESEM images of FAp/forsterite nanocomposites with different forsterite percentages are presented in Figs. 5(a-c). As shown earlier, the spherical shape of these synthesized particles with different particle sizes ranging from about 20 nm to 80 nm in three samples confirmed the XRD results. The particle sizes of FA-F-15 ranged from 45 to 80 nm. Moreover, as the forsterite particles increased, the particle sizes became finer in FA-F-25 and FA-F-35. The particle sizes in FA-F-25 ranging from 33-45 nm reached 20-40 nm in FA-F-35.

Moreover, as the Forstrite particles increase, the particle sizes become finer. This outcome was predictable due to the different diffusivity rates of between silicon and magnesium and the greater number of fluorapatite-fluorapatite grain boundaries made the growth of forsterite harder [2]. Apatite containing phase-forsterite with emphasis on SiO_2 and MgO showed slow diffusivity and exiguous presence in the assembly. These findings were also the result of research by Hiraga and Johanson who worked on synthesis and grain growth of Periclase as the main phase and forsterite as the second phase. The EDS pattern in Fig. 6 shows the

presence of oxygen, fluorine, magnesium, silicon, phosphorus, and calcium, which were the main constituents of the two structural components of the nanocomposite without the presence of impure elements.

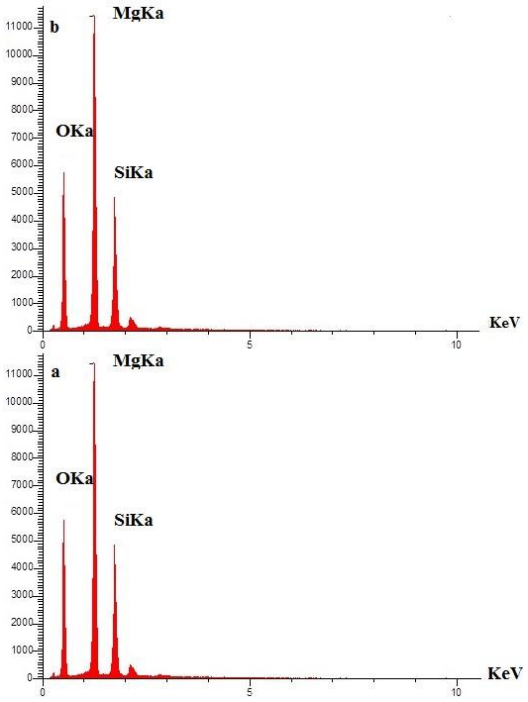

Figure 4. EDX of a) FO nanoparticle, b) EDX of FAp nanoparticle

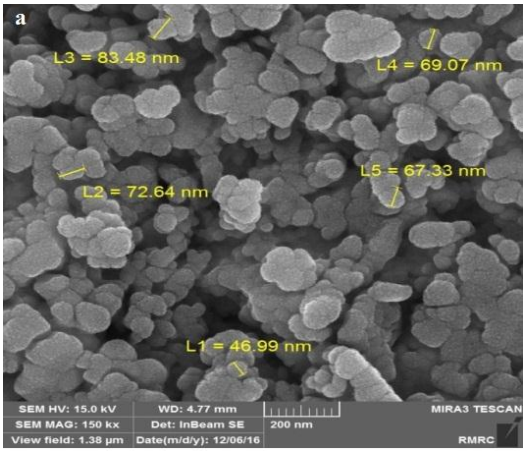

(a)

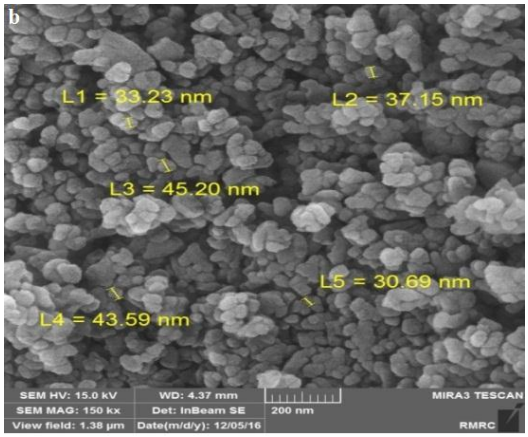

(b)

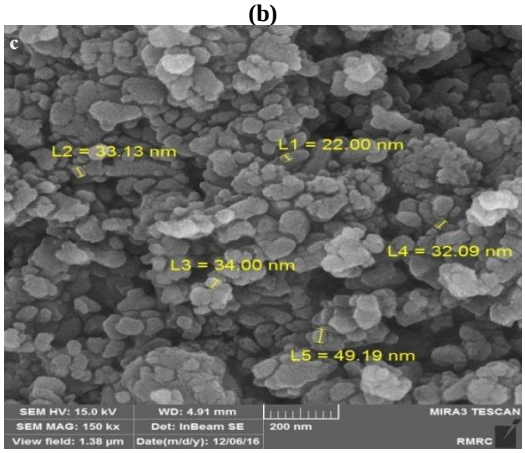

(c)

Figure 5. Field emission scanning images of FAp/forsterite nanocomposites a) FAp-F-15, b) FAp-F-25, and c) FA-F-35

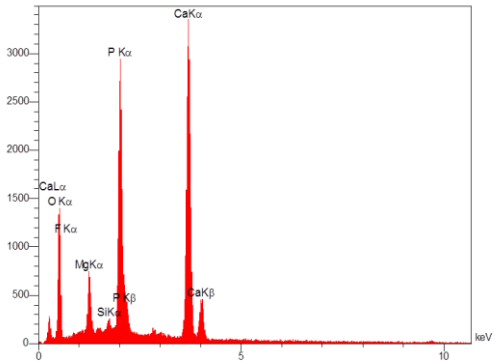

Figure 6. EDX pattern of FAp-F-25 nanocomposite

3.4. MTT TEST

The results of the MTT test (3-(4,5-dimethylthiazol-2-yl)-2,5-diphenyltetrazolium bromide) after 7 days are presented in Fig. 7. Regarding the shape, it can be found that by increasing the time duration of cell replacement

with the extract in all three main samples, negative control and positive control of cellular responses increased by 15 and 25% of forsterite, but the probability of cell survival was reduced with a 35% forsterite increase.

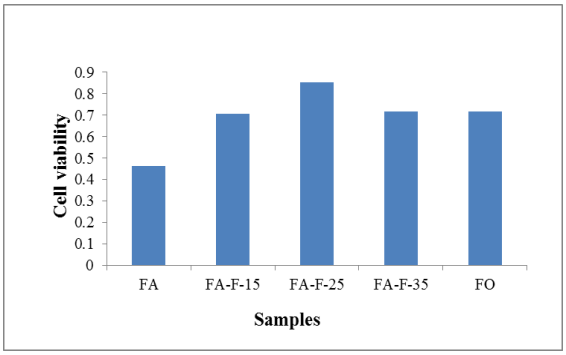

Figure 7. MTT cell survival test for all the samples after 7 days

TABLE 2. The results of the MTT cell survival test for all materials after 7 days

OD 7 days	Mean	SE
FA	0.382	0.031
FO	0.216	0.029
FA-F-35	0.292	0.024
FA-F-25	0.593	0.041
FA-F-15	0.479	0.031
Control	0.59	0.0223

Based on a comparison of the results, the FA-F-25 showed better behavior than FA-F-15 and FA-F-35, which related to the equilibrium recognized in this type of composite in terms of ion release and subsequent relative toxicity.

4. CONCLUSION

Nano forsterite and nano fluorapatite were prepared by the modified sol-gel method, and nano fluorapatite/forsterite nanocomposite with 15%, 25%, and 35% of forsterite was prepared by the modified sol-gel method at 600 °C with particle sizes ranging between 20-80 nm. Based on the X-ray diffraction patterns of forsterite and fluorapatite, the crystalline phases of forsterite with JCPDS No. 00-004-0769 and fluorapatite with JCPDS No. 00-003-0736 with a hexagonal crystal structure were produced, respectively. FTIR analysis indicated that fluorapatite and forsterite without impurities were produced. Also, the FTIR curve of nanocomposites did not change clearly by adding different percentages of forsterite. FESEM images of fluorapatite, forsterite, and fluorapatite/forsterite nanocomposites with different forsterite percentages showed the spherical shape of these synthesized particles with different particle sizes in all samples. The particle sizes of FA-F-15 ranged between 45-80 nm. Moreover, as the forsterite particles increased, the particle sizes became finer in FA-F-25 and FA-F-35. The results of the MTT cell survival test for all materials after 7 days did not show any toxicity.

REFERENCES

1. Manafi, S., Joughehdoust, S., "Synthesis and in vitro investigation of sol-gel derived bioglass-58S nanopowders", ***Materials Science-Poland***, Vol. 30, (2012), 45–52. DOI:10.2478/s13536-012-0007-2
2. Hiraga, T., Miyazaki, T., Tasaka, M., Yoshida, H., "Mantle Superplasticity and Self-made Demise", ***Nature***, Vol. 468, (2010), 1091–1094. DOI:10.1038/nature09685
3. Johnson, C.H., Richter, S.K., Hamilton, C.H., Hoyt, J.J., "Static Grain Growth in a Microduplex Ti-6Al-4V alloy", ***Acta Materialia***, Vol. 47, (1998), 23–29. DOI:10.1016/S1359-6454(98)00341-3
4. Sun, Y., Yang, H., Tao, D., "Microemulsion Process Synthesis of lanthanide-doped Hydroxyapatite Nanoparticles under Hydrothermal Treatment", ***Ceramics International***, Vol. 37, (2011), 2917-2920. DOI:10.1016/j.ceramint.2011.03.030
5. Sumathi, S., Gopal, B., "In Vitro Degradation of Multisubstituted Hydroxyapatite and Fluorapatite in the Physiological Condition", ***Journal of Crystal Growth***, Vol. 422, (2015), 36-43. DOI:10.1016/j.jcrysgro.2015.04.022
6. Choudhary, R., Chatterjee, A., Venkatraman, S., Koppala, S., Abraham, J., "Antibacterial forsterite (Mg_2SiO_4) scaffold: A promising bioceramic for load bearing applications", ***Bioactive Materials***, Vol. 3, (2018), 218-224. DOI:10.1016/j.bioactmat.2018.03.003
7. Basar, B., Tezcaner, A., Keskin, D., Evis, Z., Improvements in Microstructural, Mechanical, and Biocompatibility Properties of nano-sized Hydroxyapatites Doped with Yttrium and Fluoride, ***Ceramics International***, Vol. 36, (2010), 1633-1643. DOI:10.1016/j.ceramint.2010.02.033
8. Kheradmandfard, M., Fathi, M., "Preparation and Characterization of Mg-doped Fluorapatite Nanopowders by Sol-Gel Method", ***Journal of Alloys and Compounds***, Vol. 504, (2010), 141-145. DOI:10.1016/j.jallcom.2010.05.073
9. Mancuso, E., Bretcanu, O., Marshall, M., Dalgarno, K.W., "Sensitivity of Novel Silicate and Borate-Based Glass Structures on In vitro Bioactivity and Degradation Behaviour", ***Ceramics International***, Vol. 43, (2017), 12651-12657. DOI:10.1016/j.ceramint.2017.06.146
10. Chen, W., Wang, Q., Meng, S., Yang, P., Jiang, L., Zou, X., Li, Z., Hu, S., "Temperature-Related Changes of Ca and P Release in Synthesized Hydroxylapatite, Geological Fluorapatite, and Bone Bioapatite", ***Chemical Geology***, Vol. 451, (2017), 183-188. DOI:10.1016/j.chemgeo.2017.01.014
11. Barandehfard, F., Rad, M.K., Hosseinnia, A., Khoshroo, K., Tahriri, M., Jazayeri, H.E., Moharamzadeh, K., Tayebi, L., "The Addition of Synthesized Hydroxyapatite and Fluorapatite Nanoparticles to a Glass-Ionomer Cement for Dental Restoration and its Effects on Mechanical Properties", ***Ceramics***

International, Vol. 42, (2016), 17866-17875. DOI:10.1016/j.ceramint.2016.08.122

12. Santos, S.C., Barreto, L.S., dos Santos, E.A., "Nanocrystalline Apatite Formation on Bioactive Glass in a Sol-Gel Synthesis", ***Journal of Non-Crystalline Solids***, Vol 439, (2016), 30-37. DOI:10.1016/j.jnoncrysol.2016.02.013
13. Shen, J., Jin, B., Jian, Q. Y., Hu, Y. M., Wang, X. Y., "Morphology-Controlled Synthesis of Fluorapatite Nano/Microstructures via Surfactant-Assisted Hydrothermal Process", ***Materials & Design***, Vol. 97, (2016), 204-212. DOI:10.1016/j.matdes.2016.02.091
14. Sumathi, S., Gopal, B., "In vitro Degradation of Multisubstituted Hydroxyapatite and Fluorapatite in the Physiological Condition", ***Journal of Crystal Growth***, Vol. 422, (2015), 36-43. DOI:10.1016/j.jcrysgro.2015.04.022
15. Roche, K. J., Stanton, K. T., "Measurement of Fluoride Substitution in Precipitated Fluorhydroxyapatite Nanoparticles", ***Journal of Fluorine Chemistry***, Vol. 161, (2014), 102-109. DOI:10.1016/j.jfluchem.2014.02.007
16. Zhao, J., Dong, X., Bian, M., Zhao, J., Zhang, Y., Sun, Y., Chen, J., Wang, X., "Solution Combustion Method for Synthesis of Nanostructured Hydroxyapatite, Fluorapatite and Chlorapatite", ***Applied Surface Science***, Vol. 314, (2014) 1026-1033. DOI:10.1016/j.apsusc.2014.06.075
17. Tredwin, C. J., Georgiou, G., Kim, H. W., Knowles, J. C., "Hydroxyapatite, Fluor-hydroxyapatite, and Fluorapatite Produced via the Sol-Gel Method: Bonding to Titanium and Scanning Electron Microscopy", ***Dental Materials***, (2013), 521-529. DOI:10.1016/j.dental.2013.02.002
18. Nasiri-Tabrizi, B., Fahami, A., "Synthesis and Characterization of Fluorapatite–Zirconia Composite Nanopowders", ***Ceramics International***, Vol. 39, (2013), 4329-4337. DOI:10.1016/j.ceramint.2012.11.016
19. Joughehdoust, S., Behnamghader, A., Jahandideh, R., Manafi, S., "Effect of Aging Temperature on Formation of Sol-Gel Derived Fluor-Hydroxyapatite Nanoparticles", ***Journal of nanoscience and nanotechnology***, Vol. 10, (2010), 2892-2896. DOI:10.1166/jnn.2010.1397
20. Cooper, L.F., Zhou, Y., Takebe, J., Guo, J., Abron, A., Holmén, A., Ellingsen, J.E., "Fluoride Modification Effects on Osteoblast Behavior and Bone Formation at TiO_2 Grit-blasted CP Titanium Endosseous Implants", ***Biomaterials***, Vol. 27, (2006), 926-936. DOI:10.1016/j.biomaterials.2005.07.009
21. Rodrıguez-Lorenzo, L., Hart, J., Gross, K., "Influence of Fluorine in the Synthesis of Apatites. Synthesis of Solid Solutions of Hydroxy-Fluorapatite", ***Biomaterials***, Vol. 24, (2003), 3777-3785. DOI:10.1016/S0142-9612(03)00259-X
22. Loher, S., Stark, W.J., Maciejewski, M., Baiker, A., Pratsinis, S.E., Reichardt, D., Maspero, F., Krumeich, F. and Günther, D., "Fluoroapatite and Calcium Phosphate Nanoparticles by Flame Synthesis", ***Chemistry of Materials***, Vol. 17, (2005), 36-42. DOI:10.1021/cm048776c
23. Rey, C., Combes, C., Drouet, C., Sfihi, H., "Fluoride-based Bioceramics" In ***Fluorine and Health: Molecular Imaging, Biomedical Materials and Pharmaceuticals***, Amsterdam: Elsevier, (2008), 279-331. DOI:10.1016/B978-0-444-53086-8.00006-0
24. Chitsazi, M.T., Shirmohammadi, A., Faramarzie, M., Pourabbas, R., Rostamzadeh, A.N., "A Clinical Comparison of Nano-Crystalline Hydroxyapatite (Ostim) and Autogenous Bone Graft in the Treatment of Periodontal Intrabony Defects", ***Medicina Oral Patologia Oral y Cirugia Bucal***, Vol. 16, (2011), 448-453. DOI:10.4317/medoral.16.e448
25. Nguyen, M., Sokolar, R., "Presence of Magnesium-Alumina Spinel in Forsterite Ceramics and its Influence During Sintering and on Resulting Properties of Fired body", ***IOP Conference Series: Materials Science and Engineering***, Czech Republic, Vol. 549, (June. 1, 2019), 2019. DOI:10.1088/1757-899X/549/1/012025
26. Wassanai, W., Jidapah, R., Pana, S., "Appropriate Forming Conditions for Hydroxyapatite-Bioactive Glass Compact Scaffold", ***Engineering Journal***, Vol. 20, (2016), 123-134. DOI:10.4186/ej.2016.20.3.123
27. Ni, S., Chou, L ., "Preparation and Characterization of Forsterite (Mg, SiO_4) Bioceramics", ***Ceramics International***, Vol. 33, (2007), 83-88. DOI:10.1016/j.ceramint.2005.07.021
28. Chin, K. M., Lee, K. Y., Tan, C. Y., Singh, R., Teng, W. D., "Characterization of Forsterite Synthesized by Solid-State Reaction with Ball Milling Method", ***Applied Mechanics and Materials***, Vol. 372, (2013), 416-419. DOI:10.4028/www.scientific.net/AMM.372.416
29. Petric, N., Martinac, V., Tkalcec, E., Ivankovic, V., Petric, B., "Thermodynamic Analysis of Results Obtained by Examination of the Forsterite and Spinel Formation Reactions in the Process of Magnesium Oxide Sintering", ***Industrial & Engineering Chemistry Research***, Vol. 28, (1989), 298–302. DOI:10.1021/ie00087a008
30. Mazrooei Sebdani, M., Fathi, M. H., "Preparation and characterization of hydroxyapatite–forsterite–bioactive glass nanocomposite coatings for biomedical applications", ***Ceramics International***, Vol. 38, (2012), 1325-1330. DOI:10.1016/j.ceramint.2011.09.008
31. Forghani, A., Mapar, M., Kharaziha, M., Fathi, M. H., Fesharaki, M., "Novel Fluorapatite- Forsterite Nanocomposite Powder for Oral Bone Defects", ***International Journal of Applied Ceramic Technology***, Vol. 10, (2012), E282-E289. DOI:10.1111/j.1744-7402.2012.02824.x

AIMS AND SCOPE

Advanced Ceramics Progress (ACERP) as an ISC international journal is devoted to elucidating the fundamental aspects of chemistry and physics occurring at a wide range of oxide and nonoxide ceramics and composite materials and their processing, microstructure, properties, and applications. The journal provides a unique venue for publishing new exciting research, focusing on dynamic growth areas in this field.

INSTRUCTIONS FOR AUTHORS

Submission of manuscript represents that it has neither been published nor submitted for publication elsewhere and is result of research carried out by author(s).
Authors are required to include a list describing all the symbols and abbreviations in the paper.
Use of the international system of measurement units is mandatory.

- On-line submission of manuscripts results in faster publication process and is recommended. Instructions are given in the ACERP web site: www.acerp.ir
- Hardcopy submissions must include MS Word and jpg files.
- Manuscripts should be typewritten on one side of A4 paper, double-spaced, with adequate margins.
- References should be numbered in brackets and appear in sequence through the text. List of references should be given at the end of the paper.
- Figures' captions are to be indicated under the illustrations. They should sufficiently explain the figures.
- Illustrations should appear in their appropriate places in the text.
- Tables and diagrams should be submitted in a form suitable for reproduction.
- Photographs should be of high quality saved as jpg files.
- Tables, illustrations, figures and diagrams will be normally printed in single column width (8 cm). Exceptionally large ones may be printed across two columns (17 cm).

PAGE CHARGES AND REPRINTS

ACERP subscribers do not need to make any payment for publication and reprints. Five offprint, pdf file and two copies of the issue that contains the published article will be supplied for every article.

AUTHORS CHECKLIST

- Author(s), bio-data including affiliation(s) and mail and e-mail addresses.
- Manuscript including abstract, key words, illustrations, tables, figures with figures' captions and list of references.
- MS Word files of the paper.

Advanced **Cer**amics **P**rogress,
P.O. Box 31787-316, Karaj, Alborz, I. R. Iran
Materials and Energy Research Center, Imam Khomeini Blvd, Meshkin Dasht, Karaj, Alborz, I. R. Iran
P.O. Box 14155-4777, Tehran, I. R. Iran
No. 5, Ahuramazda St., Alvand Ave., Argentine Sq., Tehran, I. R. Iran

www.merc.ac.ir - www.icers.ir

Advanced Ceramics Progress

Volume 6, Number 2, Spring 2020

CONTENTS

Journal Home Page: www.acerp.ir